OPTOELECTRONIC AND THERMAL PROPERTIES OF METALLIC TRANSITION METAL DICHALCOGENIDES

A DISSERTATION SUBMITTED TO

THE GRADUATE SCHOOL OF ENGINEERING AND SCIENCE

OF BILKENT UNIVERSITY

IN PARTIAL FULFILLMENT OF THE REQUIREMENTS FOR

THE DEGREE OF

DOCTOR OF PHILOSOPHY

IN

MATERIALS SCIENCE AND NANOTECHNOLOGY

By

Naveed Mehmood

November 2020

Optoelectronic and Thermal Properties of Metallic Transition Metal Dichalcogenides

By Naveed Mehmood

November 2020

We certify that we have read this dissertation and that in our opinion it is fully adequate, in scope and in quality, as a dissertation for the degree of Doctor of Philosophy.

Talip Serkan Kasırga(Advisor)

Menderes Işkin

Selim Hanay

Hilmi Volkan Demir

Hasan Şahin

Approved for the Graduate School of Engineering and Science:

Ezhan Karaşan
Director of the Graduate School

ABSTRACT

OPTOELECTRONIC AND THERMAL PROPERTIES OF METALLIC TRANSITION METAL DICHALCOGENIDES

Naveed Mehmood
Ph.D. in Materials Science and Nanotechnology
Advisor: Talip Serkan Kasırga
November 2020

After the successful isolation of graphene monolayer from its bulky counterpart, there has been tremendous advancement in the field of 2D material. Transition metal dichalcogenides(TMDCs) is family of 2D materials comprising of a transition metal atom sandwiched between two chalcogen atoms. Photoresponse of semiconducting TMDCs has been studied extensively in literature. However, photoresponse from metallic TMDCs is unprecedented and hence has not been studied to explore which mechanism might prevail. Among our findings, we discovered that photocurrent generation through metallic TMDCs is possible and has a photo-thermal origin. Using scanning photo-current microscopy, we were able to obtain spatial photocurrent maps for both, zero biased and biased samples. At zero applied bias, the photocurrent generation is localized to metal-metal junction and governed by Seebeck effect. At finite applied bias, photocurrent from the whole crystal is observed and is due to photobolometric effect. As Photo-bolometric effect relies on photo-thermally induced resistance change of the material, we extended our study to extract thermal conductivity of metallic TMDCs via bolometric effect. As contact of crystal with substrate act as a heat sink, we used suspended crystals over a hole to thermally isolate it from any heat sink. Resistance change via laser induced heating is experimentally measured at the center of the suspended part of crystal. Measured resistance change is matched with expected resistance change which is calculated using thermal conductivity(κ) as a fitting parameter via commercially available finite element method package(COMSOL). This way, thermal conductivity of the metallic TMDCs is calculated with very high accuracy and precision.

Keywords: Opto-electronics, Photo-current, Seebeck Effect, Photo Bolometric effect, TMDCs, Thermal conductivity .

ÖZET

GEÇİŞ METAL DİKALKOJENİTLERİNİN OPTOELEKTRONİK VE TERMAL ÖZELLİKLERİ

Naveed Mehmood
Malzeme bilimi ve Nanoteknoloji, Doktora
Tez Danışmanı: Talip Serkan Kasırga
Kasım 2020

Tek katmanlı grafenin bulk muadilinden başar ılı bir şekilde izolasyonunda sonra, iki boyutlu malzemeler alanında büyük bir ilerleme oldu. Geçiş metal kalkojenleri (GMK) bir geçiş metal atomun iki kalkojen atomu arasına sıkıltırılmasınıiçeren iki boyutlu malzemelerin ailesidir. Yarı iletken GMK'ların ışığa tepkileri literatürde kapsamlı bir şekilde incelendi. Ancak, metalik GMK'ların ışığa tepkilerine daha önceden görülmedi ve dolayısıyla geçerli olan işleyiş şeklini keşfedecek çalışmalar olmadı. Bulgularımız arasında, metalik GMK'lar aracılığı ile fotoakım üretmenin mümkün olduğunu ve bir foto-termal kökene sahip olduğunu keşfettik. Taramalı foto-akım mikroskobunu numunelerin hem sıfır önakım hem de ön akımsız kullanarak, uzamsal fotoakım haritalarını elde edebildik. Uygulanan sıfır önakımında, foto akım üretimi metal-metal bağlantısında yer alır ve Seebeck etkisi ile yönetilir. Uygulanan ölçülebilir ön akımda, fotobolometrik etkiden dolayı, tüm kristalden gelen foto akım gözlemlendi. Foto-bolometrik etki malzemenin foto-termal indüklenen direnç değişimine dayandığından, metallic GMK'ların termal iletimlerini bolometrik etki aracılığı ile elde etmek için çalışmamızı genişlettik. Kristalin altaş ile teması, bir ısı havuzu gibi davrandığından, herhangi bir ısı havuzudan termal olarak izolasyon sağlamak için bir delik üzerine bırakılan kristalleri kullandık. Lazerin kaynaklandığı ısıma ile oluşan direnç değişimi kristalin merkezinden deneysel olarak ölçülmüştür. Piyasada satılan sonlu eleman metodu paketi (COMSOL) aracılığı ile, Termal iletkenliğin (κ) uyma paramatresi olarak kullanıldığı ölçüm değişimleri ve beklenen direnç değişimi eşleşmektedir. Bu şekilde, metallik GMK'ların termal iletkenliği yüksek kesinlik ve doğruluk ile hesaplandı.

Anahtar sözcükler: Opto-elektronik, Foto-akım, Seebeck Etkisi, Foto Bolometrik etki, GMK, Termal iletkenlik .

Acknowledgement

I am grateful to Almighty Allah, the most beneficent and merciful, All embracing, all knowing who provided me with the opportunity, courage and ability to complete this research work.

I feel proud to express my deepest sense of gratitude and appreciation to my PhD advisor Assist. Prof. Dr. Talip Serkan Kasırga for his kind help, inspiration, encouragement, sympathetic attitude and sincere personal involvement through out the research. He has provided me with the great ideas to conduct quality research. I also extend my warm thanks to my thesis committee members Dr. Menderes Işkin and Dr. Selim Hanay for their motivation, generous assistance and appreciation for my research work. Their timely constructive criticism kept me on the right path all through my PhD research. All the experiment that I performed were not possible without their value-able suggestions, cooperation and helpfulness. To our collaborators Dr. Engin Durgun and Mert Miraç who provided theoretical support for few our experimental work.

I would like to acknowledge SCM Lab members who made my stay here enjoyable. The moments we spent together are full of joy, fun, smiles and rejoicing. I would like to acknowledge value-able contribution of Mr. Onur Çakiroğlu who helped me during the thermal conductivity experiments with theoretical support. I would like to extend my acknowledgement to Mr. Hamid Reza Rasouli who had been great help during my experimental work. To Ali Sheraz and Merve Üstünçelik who were always there to cheer me up whenever I felt down during some experimental failures. To former SCM lab members, Engin Can Surmeli, Mustafa Fadlelmulla, Mehdi Ramezani, Koray Yavuz, Sena Nur Arselan and Ibrahim, who were there to help me to built up knowledge of basic concepts of the field.

My acknowledgement is incomplete without mentioning all the support from my beloved wife Breera Maqbool during my research work. She provided me with feeling of not being distressed even when things were not going according to plan. She is the soul of all my work which was impossible without her presence. To my daughters Haya Naveed and Neha Hazel Mehmood who kept me motivated everyday I stepped out of my home. To my beloved Munni Phupo(Nasreen Naz) whose

prayers always acted as a deriving force for me to reach excellence. She made sure that she would not miss my PhD thesis Dissertation by flying from Pakistan all the way to Ankara. To my brother Burhan Mahmood, whose unconditional love and support kept me follow my dreams everyday.

To my parents, my father Khalid Mehmood and my mother Naseem Akhter, it goes with out saying that I would not have been here without your prayers and support. I owe my existence to them and with out them I would have been nothing. This thesis brought the dream of my mother to the reality which makes me really a proud son who fulfilled desire of a deceased mother.

Finally to all my friends who had been my support through thick and thin. They all made my days colorful with their presence. Talha Masood Khan, Saeed Ahmad, Waqas Akbar, Murat Serhetioglu, Ali Haider, Umair Laique, Mehvish Shafi, Anjum Qureshi, Muhammed Saqib, Salahuddin Zafar, Naveed ul Mustafa, Abdul Waheed, Farhan Mughal, Mite Mijalkov, Khushbakht Ali, Laila-tul-Qadar, Furqan Ali, Zulfiqar Ali, Ali Kalantarifard, Mohsin Habib, Mhammad Hamza, Anum Anwar, Shoaib Anwar, Mirza Saad, Ramiz Bukhari, Ghulam Abbas, Sajjad-ur-Rehman, Muhammad Adnan, Habib Gultekin, Zia Isiksacan, are a few to mention. To UNAM support team, Duyugu Hanim, Ayşegul Hanim, Semih Bozkart, Ovenç bey, Mustafa Abi and Mustafa Doğan, who made sure we can perform our research uninterepted at fullest of our capability.

Thank you everyone who has always been there during this beautiful journey of mine and for their unconditional support in coming many more years.

To My Better Half, My Love, My Life

Contents

1 Introduction **1**

1.1 Elemental Layered Materials 2

1.2 Compound Layered Materials 3

1.3 Transition Metal Dichalcogenides 3

1.3.1 Structure 3

1.4 Metallic Transition Metal Dichalcogenides 6

1.5 Photocurrent Generation in Semiconducting Transition Metal Dichalcogenides 8

1.6 Thermal Conductivity of TMDCs and Nano-Sheets 9

1.7 Thesis Motivation and Outline 10

2 Photocurrent generation and possible mechanisms in 2D materials **12**

2.1 Mechanisms of photocurrent generation 12

2.1.1 Photo-conductive effect 13

2.1.2 Photo-gating effect 15

2.1.3 Photovoltaic effect 17

2.1.4 Photo-thermoelectric effect 18

2.1.5 Photo-bolometric effect 20

3 Photo-current generation in metallic transition metal dichalcogenides **21**

3.1 Experimental methods 22

3.1.1 Bottom contact devices 22

3.1.2 Top contact devices 26

3.1.3 Current vs voltage measurements 29
3.1.4 Scanning photocurrent microscopy 29
3.2 Results and discussion 31
3.2.1 Material Characterizations 31
3.2.2 Top contact devices 34
3.2.3 Bottom contact devices 41
3.2.4 Photoconductance dependence on Laser Power 44
3.2.5 Low pressure measurements and BC device with low contact resistance 45
3.2.6 Effect of polarization on photoresponse 48

4 Thermal conductivity measurements in 2D Materials, Methods and Limitations 49
4.1 Steady State Techniques 50
4.1.1 Raman Thermometery 51
4.1.2 Micro-Bridge Thermometery 53
4.2 Transient Techniques 54
4.2.1 Time Domain Thermo-Reflectance Method(TDTR) 55
4.2.2 3ω Method 57
4.3 Bolometric effect based Method 57

5 Thermal Conductivity Measurement via Bolometric Effect 58
5.1 Bolometric Effect 59
5.2 Isotropic 2D Materials, Analytical Solution of the heat Equation . 60
5.3 Thermal Conductivity Calculation Strategy via Bolometric Effect 63
5.4 Experimental Methods 64
5.4.1 Substrate Preparation and Bottom Contact Devices 64
5.4.2 Top Contact Devices 69
5.4.3 IV Characteristic and Scanning Photocurrent Microscopy 70
5.4.4 Full Width Half Maximum Value for Focused Laser Spot . 71
5.4.5 Calculating Absorbance of Material 72
5.5 Thermal Conductivity Measurement of Metallic Vanadium Sesquioxide(V_2O_3) 73
5.5.1 Material Characterization 76

5.5.2 Thermal Conductivity of Metallic V_2O_3 79
5.6 Thermal Conductivity measurements of 2H Tantallum DiSulfide(TaS_2) 81
5.6.1 Material Characterization 81
5.6.2 Thermal conductivity of 2H-TaS_2 82
5.7 Thermal Conductivity Measurement of Semiconducting Materials 85

6 Conclusion **88**
6.1 Research Topics Outside Scope of This Thesis 90

List of Figures

1.1 Schematic of graphene layer containing carbon atoms closely packed in honey comb lattice. 2

1.3 Periodic table showing classification of different elements. Each color describe certain type of element. Purple color on this table represents transition metal elements and orange color is representing S, Se and Te along with some other elements. Copyright Encyclopedia Britannica 5

1.4 (a) Laser induced phase transformation of $MoTe_2$ from 2H phase to 1T'. Copyright American Association for the Advancement of Science 2015(b) CVD grown 2H-MoS_2 crystal selectively converted to 1T phase upon treatment with n-butyl lithium. Copyright Springer Nature 2014 6

1.5 (a) In-plan (ρ_{ab}) and out of plane (ρ_c) resistivity plotted as a function of temperature at ambient pressure. The kink shows CDW transition. Inset shows superconducting transition below 0.9K temperature. (b) Resistivity measurements at higher pressure. The CDW transition suppresses at very high pressure while the shift towards higher temperature for superconducting transition is observed(inset). Copyright Springer Nature 2016 8

1.6 (a) Normalized resistance vs temperature plotted for 2H-NbS_2 for various thickness crystals. (b) The data in the rectangular window in (a) to see superconducting transition between 0K to 10K. Copyright IOP Science, The Japan Society of Applied Physics, 2019 . 9

2.1 (a) Schematic of band alignment when two metal contacts are made to semiconducting material under some applied bias without illumination. (b) Bang alignment under applied bias when a device is illuminated with photons of energy E_{ph} greater than band gap E_{bg}. (c) Current plotted against applied gate voltage with and without illumination. (d) IV plots in dark (black line) and under illumination(red solid line). Reproduced from Ref. [62] with permission from The Royal Society of Chemistry. 14

2.2 (a) Schematic of band alignment when two metal contacts are made to semiconducting material under some applied bias without illumination. (b) Bang alignment under applied bias when a device is illuminated with photons of energy E_{ph} greater than band gap E_{bg}. Holes are shown to be trapped at th band edge. Upon illumination and under applied bias, field effect produces electrons in the channel which contribute towards photocurrent generation. (c) Current plotted against applied gate voltage with and without illumination. (d) IV plots in dark (black line) and under illumination(red and blue solid lines). Reproduced from Ref. [62] with permission from The Royal Society of Chemistry. 16

2.3 (a) Schematic of a PN-junction formation. Common fermi energy (E_f) level for both P and N doped semiconductor can be seen in the schematic represented by dashed black line. The incident photon of energy larger than band gap of the material (E_{ph}¿, E_{bg}) generates the electron hole pair as represented by black and white dot respectively. The built in electric field at the PN-junction then separates the electron hole pair and gets accelerated. (b) I_{ds} vs V_{ds} curves plotted in dark and under illumination represented by black and red lines respectively. A short circuit current due to open circuit voltage is generated in the device upon illumination. An electrical power is generated by the device indicated by P_{el}^{max} (maximum power). Reproduced from Ref. [62] with permission from The Royal Society of Chemistry. 18

2.4 (a) Schematic of a FET which is being illuminated locally using a focused laser spot at one of the metal-semiconducting junction. The configuration represent the open circuit case where the thermoelectric potential is generated between the two junctions. (b) represents the circuit diagram of the same device depicted in (a). (c) IV characteristic curve in both dark (black) and under illumination(red) are plotted. Under zero bias, a current is generated in the system driven by the thermoelectric potential difference(V_{PTE}). Reproduced from Ref. [62] with permission from The Royal Society of Chemistry. 19

3.1 Array of two terminal electrodes patterned using optical lithography 23
3.2 Schematic of the deterministic crystal transfer starting from mechanical exfoliation of the NbS_2 till the selected flake aligned and transferred on top of metal electrode. 24
3.3 Optical microscope images of back contact devices. scale bar is 30μm 25
3.4 Electron microscope images of back contact devices showing top view and side view of the devices. 25
3.5 Optical micrographs of the fabricated devices top contact devices using optical lithography. Scale bar is 30μm 27
3.6 Electron microscope images of top contact devices showing top view and side view of the selected device. 27
3.7 Schematic of the side view (a) and top view (b) of the crystal structure of 3R-NbS_2. Reproduced from ref. [91]. Copyright American Physical Society 2018 31
3.8 Schematic of the side view (a) and top view (b) of the crystal structure of 3R-NbS_2. Reproduced from ref. [91]. Copyright American Physical Society 2018 32
3.9 Schematic of the side view (a) and top view (b) of the crystal structure of 3R-NbS_2. Reproduced from ref. [91]. Copyright American Physical Society 2018 33

3.10 (a) Low resolution transmission electron microscopy image of NbS_2 flake. (b) Selected area diffraction pattern from the same crystal. Reproduced from ref. [91]. Copyright American Physical Society 2018 33

3.11 SEM micrograph of two terminal device with measurement configuration depicted on it. A diffraction limited laser spot raster scans the samples in x-y direction. In all our experiments, left electrode is grounded and the bias is applied from the right electrode. Reproduced from ref. [91]. Copyright American Physical Society 2018 34

3.12 (a) Optical micrograph of the TC1 is shown with marked square region in which SPCM is performed. Scale bar is 10μm (b) Reflection map obtained by scanning the laser on top of the device and (c) corresponding photocurrent map under zero applied bias. The photocurrent is confined around the edges which are marked by the dashed black lines. (d) Resistance vs temperature plot of the same device showing characteristic metallic behavior. The inset shows ∂R/∂T as a reference. (e) Upper panel shows V_{PC} plotted as a function of laser power The measurement is taken from NbS_2 metal junction marked by yellow dashed circle on the photocurrent map. Red and blue points from left and right electrodes respectively. By using V_T vs P data, calculated ΔT_C/P is plotted in the lower panel. Reproduced from ref. [91]. Copyright American Physical Society 2018 35

3.13 Atomic force microscopy image along with height profile along the vertical red line. Reproduced from ref. [91]. Copyright American Physical Society 2018 36

3.14 (a) Photocurrent map of TC-1 under 50mV applied and (b) -50mV applied bias. The photocurrent is generated from whole crystal between the metal electrodes. (c) Upper panel shows line trace of the photocurrent intensity map going from one electrode to other through center of the crystal for applied biases -50mV, -20-, 0-, 20- and 50mV. Lower panel shows the corresponding bias independent photo-conductance. Reproduced from ref. [91]. Copyright American Physical Society 2018 38

3.15 Schematic model showing different parameters used to calculate ∂T_l using a python code. Reproduced from ref. [91]. Copyright American Physical Society 2018 39

3.16 (a) Optical micrograph of prepared indium top contact device (IC-1). Dashed white region shows the area where SPCM is performed. Scale bar is 10μm. (b) Reflection map (c)(d) and (e) photocurrent maps at zero, -50mV and 50mV applied bias respectively. Dashed line in the (d) corresponds to line traces plotted in upper panel of (f) at several different biases. As can be seen the Seebeck effect is significantly diminished but the photoconductance remain invariant (lower panel (f)) for all applied biases through the crystal. (g) Photocurrent plotted against increasing laser power showing linear dependence. Reproduced from ref. [91]. Copyright American Physical Society 2018 42

3.17 (a)Optical micrograph of a bottom contact device. scale bar is 10μm. (b) Photocurrent map under zero applied bias. The photoresponse is localized to a small region and is a magnitude smaller than TC device. (c) and (d) photocurrent maps at 50mv and -50mV applied biases respectively. Photoresponse changed only at the NbS_2/metal junction and no response is observed through middle of the crystal. Reproduced from ref. [91]. Copyright American Physical Society 2018 43

3.18 (a) Optical micrograph of TC-2 device. (b) and (c) are photocurrent maps of same device under 50mV and -50mV applied biases respectively. (d) change in photoconductance as a function of applied bias under different laser illumination powers. (e) Corresponding photoconductance per unit laser power at several applied bias. Reproduced from ref. [91]. Copyright American Physical Society 2018 44

3.19 (a) Typical reflection map obtained during SPCM.(b) and (c) photocurrent maps under -50mV applied bias both under ambient and low pressure respectively. No change in photoresponse observed under low pressure.(d) Line trace through the middle of the crystal taken from photocurrent maps. No difference observed except slight shifting which is because of centering of the line trace. . . . 46

3.20 (a) Reflection map of BC-2 obtained during SPCM. Scale bar is 10μm. Photocurrent maps obtained under 50mV applied bias (b) in ambient and (c) in low pressure. (d) IV characteristic curves taken at ambient and 0.3mBar. There is no resistance change in the device for both cases. Reproduced from ref. [91]. Copyright American Physical Society 2018 47

3.21 (a) Reflection map of TC-4 obtained during SPCM. Zero bias photoresponse using (a) unpolarized and (b) linearly polarized laser beam. Photoresponse under 50mV applied bias for (d) unpolarized and (e) linearly polarized laser beam. Both zero and 50mV bias measurement show no effect of laser light polarization. Scale bar is 5μm. Reproduced from ref. [91]. Copyright American Physical Society 2018 48

4.1 (a) and (b) show SEM image of microbridge structure for supported and suspended graphene flake respectively. scale bar 5μm (c) Close up SEM image of the device with graphene suspended over the contact pads. Scale bar 1μm (d) Schematic circuit diagram of the fabricated device. Reproduced from ref. [108]. Copyright American Chemical Society 2011. 54

4.2 (a) Schematic of typical samples used for TDTR technique. Both thin film and bulk sample configuration is shown. (b) Drawing of typical setup used for TDTR setup. Used abbreviation are PBS(Polarizing beam splitter), BS(Beam splitter), EOM(Electro-optic modulator), $\lambda/2$(Half wave plate). Reproduced from ref. [110]. Copyright AIP Publishing 2018. 56

5.1 (a) schematic of the measurement system along with fabricated device is drawn. A thin nanosheet is suspended over the hole with a radius a. (b) Temperature profile of a 2D material suspended over the hole under certain laser illumination. Dashed red circular line mark the boundary of the hole. Temperature rise is maximum at the center of the hole while equiliberate with ambient as we move far away from center. Lower panel show line trace through the center of the hole showing both analytical and FEM solution. Reproduced from ref. [117] .Copyright Springer Nature 2020. . . . 60

5.2 (a) SEM image of a typical device suspended over a hole with a diameter of 4μm. (b) (i)Temperature profile of the crystal between the electrodes with Gaussian laser spot focused at the center of hole. (ii) Corresponding current density and (iii) electric field potential are plotted based on local resistivity $\rho(x, y)$. Reproduced from ref. [115]. Copyright IOP Publishing Ltd. 2020. 64

5.3 Optical micoscope image of patterns developed after optical lithography using negative tone photoresist. 66

5.4 (a)AFM topography of the deposited metal electrodes into the pits created by ICP etching. (b) Corresponding height profile along the dashed white line. As can be seen, both metal and SiO_2 surfaces are on same level. 67

5.5 (a) SEM image of the drilled hole between the electrodes. Scale bas 10μm(b) Tilted angle close up of the drilled hole with high aspect ratio and desired shape and size. Scale bar 1μm. Reproduced from ref. [117] .Copyright Springer Nature 2020. 68

5.6 (a) 280nm thick SiO_2 wafer is chosen for fabrication (b) Gold metal evaporated into pits prepared after optical lithography and ICP etching. (c) Hole drilled using focused ion beam milling between electrodes.(d) 2D material transferred using all dry visco-elastic stamping method. 68
5.7 V_2O_3 crystal transferred on top of hole marked with red dashed circle. Two indium needles are drawn using micro-manipulator which act as electrodes. Scale bar is 5μm. Reproduced from ref. [115]. Copyright IOP Publishing Ltd. 2020. 70
5.8 First position derivative of the intensity from reflection map yields two Gaussian peaks. Full width half maximum value for laser spot is obtained by the Gaussian fitting to the peaks. Inset shows reflection map of a fabricated device with red dashed line indicating the line trace path. Reproduced from ref. [115]. Copyright IOP Publishing Ltd. 2020. 71
5.9 Absorbance measurement schematic is shown in the figure. Spectrometer is used to measure the intensities of both reflected and transmitted light. 73
5.10 Absorbance measurement schematic is shown in the figure. Spectrometer is used to measure the intensities of both reflected and transmitted light. Reproduced from ref. [115]. Copyright IOP Publishing Ltd. 2020. 74
5.11 The phase diagram of V2O3 based on reference. The paramagnetic metal (PM) and insulator (PI) phases have corundum structure, while the antiferromagnetic insulator phase (AFI) has a monoclinic structure. Reproduced from ref. [119]. Copyright American Physical Society 2019. 75
5.12 Phase diagram indicating that both as grown and transferred crystals from growth substrate enter supercritical correlated state upon heating. Reproduced from ref. [119]. Copyright American Physical Society 2019. 76

5.13 Optical microscope images of V_2O_3 crystals with different morphologies, shapes and thickness grown by salt-assisted chemical vapor deposition. Scale bar is 20μm. Reproduced from ref. [119]. Copyright American Physical Society 2019. 77

5.14 (a) Low resolution TEM image of V_2O_3 crystal transferred over holey carbon TEM grid. The insets shows EDS maps of vanadium(yellow) and oxygen(red) elements. (b) High resolution Cross-sectional TEM image of V_2O_3 crystal stackced on top of sapphire substrate. scale bar is 2nm. (c) Selected area diffraction pattern obtain from cross-sectional TEM sample. This pattern matched uniquely with HCP [01$\bar{1}$2] diffraction pattern. Reproduced from ref. [119]. Copyright American Physical Society 2019. 78

5.15 Raman spectrum of as-grown (red) and transferred V_2O_3 crystals from sapphire substrate. The shift in the peak positions can be seen along with appearance of a shoulder to the 248cm^{-1} peak. Reproduced from ref. [119]. Copyright American Physical Society 2019. 79

5.16 (a) Optical microscope image of V_2O_3 device prepared for thermal conductivity measurements. The red dashed line represents the location of hole under the crystal. (b) Reflection map collected during SPCM of the same device. (c) Photocurrent map of the device under applied bias. (d) FEM simulation of thermal profile of the devices mapped onto optical microscope image. Under 9.5 μW laser power, the maximum temperature rise at the center of the hole is 2.5K above room temperature. Reproduced from ref. [115]. Copyright IOP Publishing Ltd. 2020. 80

5.17 schematic of top and side view of the 2H stacked TaS_2 crystal in the upper and lower pannel respectively. Lower layer is rotated by an angle of 60^0 with respect to upper layer. Ta and S atoms are marked on the schematic. 81

5.18 Raman spectrum of 2H-TaS_2 mechanical exfoliated crystal. Two characteristic peak a labeled E_{2g} and A_{1g} which correspond to in-plane and out of plane vibration modes of phonons respectively. . 82

5.19 (a) Schematic of proposed thermal conductivity measurement method. The red cone symbolize focused Gaussian beam chopped at a certain frequency. Current under applied dc bias is measured through pre-amplifier which a fed to lock-in amplifier referenced by the laser chopper.(b) Cross-section schematic of the fabricated device. (c) Typical reflection map obtained by SPCM. scale bar is 5μm(d) Photocurrent map under zero applied bias. Photocurrent generated due to Seebeck at the metal-TaS_2 junctions can be seen. (e) Photocurrent map under 50mV applied bias. Negative photoresponse can be seen coming from whole crystal. The photocurrent at suspended part of crystal is distinctly decreased. (f) Line traces through the dashed lines drawn over zero and 50mV photocurrent maps. (g) Resistance change extracted for each laser position corresponding to photocurrent trace line plotted. Reproduced from ref. [115]. Copyright IOP Publishing Ltd. 2020. 83

5.20 (a) Optical microscope image of fabricated device.(b) Reflection map obtained during SPCM.(c),(d) and (e) shows photocurrent maps under 0mV, 50mV and -50mV respectively.(f) Corresponding resistance change plotted as a function of laser position. Reproduced from ref. [115]. Copyright IOP Publishing Ltd. 2020. . 84

5.21 (a)Optical image of fabricated top indium contact device.(b) Reflection map of the same device obtained by SPCM.(c)-(d) photocurrent maps collected under 400mV and -400mV applied bias respectively.(e) Characteristic current vs voltage plot in a bias sweep range of 400mV to -400mV.(f) Line traces from the photocurrent maps through the center of the hole for different applied biases.(g) Corresponding resistance change plotted as every laser position. Reproduced from ref. [115]. Copyright IOP Publishing Ltd. 2020. 86

5.22 (a)Optical image of fabricated top indium contact device.(b) Reflection map of the same device obtained by SPCM.(c)-(d) photocurrent maps collected under 400mV and -400mV applied bias respectively.(e) Characteristic current vs voltage plot in a bias sweep range of 400mV to -400mV.(f) Line traces from the photocurrent maps through the center of the hole for different applied biases.(g) Corresponding resistance change plotted as every laser position. Reproduced from ref. [115]. Copyright IOP Publishing Ltd. 2020. 87

6.1 TaS_2 crystal transferred over array of holes prepared by electron beam lithography and ICP etching. Several similar samples were prepared to study mechanical properties of this material. 90

6.2 Optical image of $KMnO_2$ device. Graphite crystals exfoliated and transferred deterministicaly on top of hexagon shaped $KMnO_2$ crystal with extremely fine alignment. Indium needles can be seen in bright silver contrast contacted with graphite electrodes for electrical connection. 91

List of Tables

4.1 Comparison of thermal conductivities of different 2D materials measured using raman thermometery method. Reproduced from ref. [104]. Copyright John Wiley & Sons, Ltd. 2017 52

5.1 Thermal conductivity(κ) values calculated for four different samples. Different laser powers along with wavelengths used to measure thermal conductivity. All yielded similar κ values with in error margin. Reproduced from ref. [115]. Copyright IOP Publishing Ltd. 2020. 85

Chapter 1

Introduction

We are surrounded by the world of 3D objects if we look around. Most materials that we encounter in our daily lives are three dimensional materials. If we look at their structure, we will notice that atoms in those materials are stacked up and arranged in a regular crystalline pattern. This arrangement can be analogous to the pile of oranges stacked up in a market shop. There exist another class material in which atoms are arranged in layers with each layer stacked on top of each other. It can be analogous to sheet of papers lying on top of each other. Materials with stronger in-plane bonds and weaker out of plane bonds can be categorized as layered material[1]. As a consequence of weak out of plane bonds, these layers can be separated from their bulk counterpart down to single layer of material. Based on composition there can be two major classifications of layered materials.

1. Elemental layered materials
2. Compound layered materials

1.1 Elemental Layered Materials

As suggested by the name, layered materials constitute of single element can be termed as elemental layered material. As we thin down from few layer to monolayer, the material can be called 2D material. Isolation of atomically thin single layer of carbon atoms led to the discovery of graphene by Novoselov and Geim back in 2004[2]. This was first detailed study on 2D materials. Their ground breaking experiments on graphene won them 2010 Nobel prize in physics. Graphene is single layer of carbon atoms which are very strongly bonded with each other via covalent bonds but has very weak van der Waals forces between layers which make it easier to exfoliate. It has closely packed carbon atoms arranged in a honey comb lattice. It has sp^2 hybridization between carbon atoms. Fig.1.1 shows the schematic of single layer of graphene.

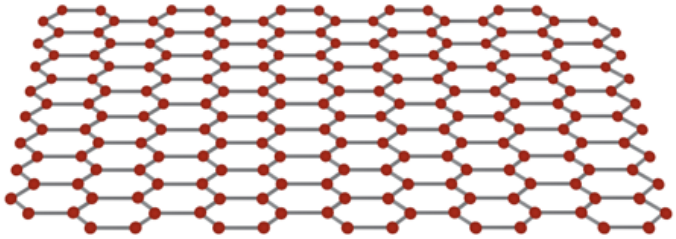

Figure 1.1: Schematic of graphene layer containing carbon atoms closely packed in honey comb lattice.

Other examples of elemental 2D materials include germanene[3][4], phosporene[5][6], borophene[7][8], antimonene[9][10], silicene[11][12] etc. All of these mentioned material exhibits very unique properties in the 2D limit due to strong quantum confinement and higher surface area which yields high surface activity[13][14].

1.2 Compound Layered Materials

Layered materials constitute of more than one elements in their layers are termed as compound layered materials. Some examples of compound layered materials include transition metal dichalcogenides(TMDCs), transition metal oxides, double hydroxides, boron nitride etc. TMDCs have gathered quite significant importance because of their extraordinary properties when exfoliated down to monolayer. One of the major advantage of TMDCs is the presence of tunable band gap which is absent in graphene[15]. TMDCs have been studied extensively in past decade and found potential applications in biosensors[16][17][18], photo detectors[19][20], memristors[21][22], field effect transistors (FET)[23] etc.

1.3 Transition Metal Dichalcogenides

Transition metal dichalcogenides is a family of 2D materials with a general formula MX_2 where M refers to transition metal atom(Mo, W, Nb, V, Ta etc.) and X refers to chalcogen atom(S, Se, Te). Historically, TMDCs were discovered structurally for the first time by Linus Pauling back in 1923[24]. More than 40 layered TMDCs were known by the end of 1960. Obtaining very thin layers of MoS_2 using adhesive tape was realized back in 1963. Monolayer suspension of MoS_2 was obtained in 1986 for the first time. Followed by this, Reshef Tenne successfully synthesized WS_2 nanotubes along with MoS_2 nanotubes later on. After the discovery of graphene in 2004, the research in the field of layered materials including TMDCs accelerated tremendously.

1.3.1 Structure

TMDCs exist in several structural phases depending on the coordination of transition metal atom. The most common phases are named as 2H, 3R and 1T . 2H crystal phase is hexagonal symmetric with trigonal prismatic coordination having

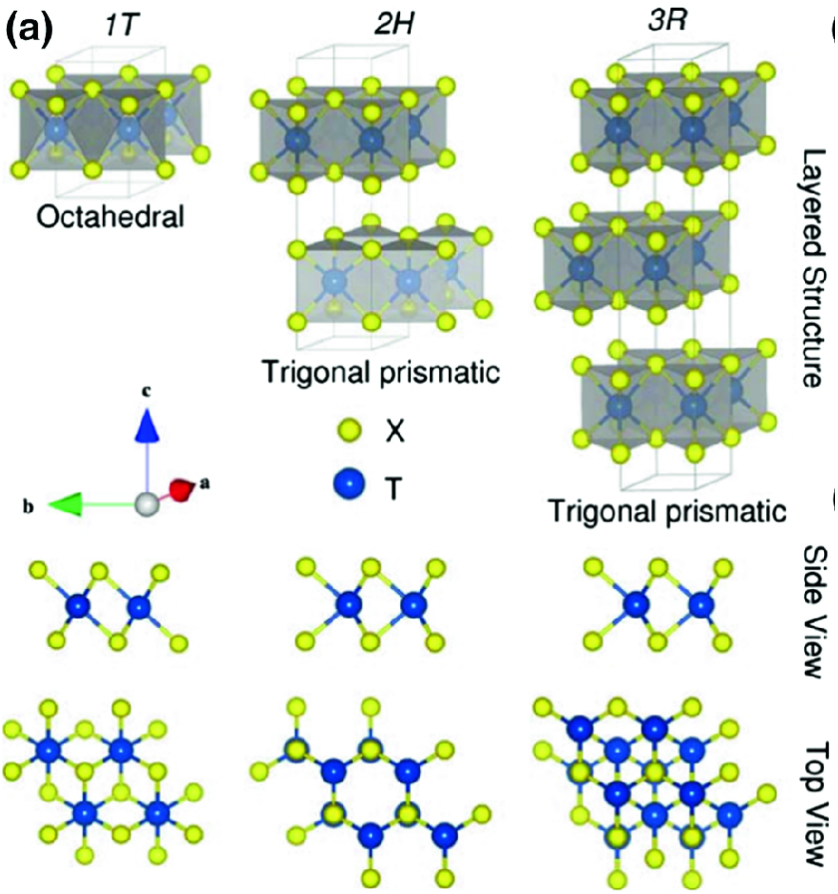

Figure 1.2: Atomic structure schematics of TMDCs showing tetragonal octahedral(1T), hexagonal trigonalprismatic(2H), and rhombohedral trigonal prismatic(3R) crystal phases in monolayer form[25]. Copyright Springer Nature 2019.

two layers per hexagonal unit cell. 1T phase is trigonal symmetric with octahedral coordination having one layer per unit cell[26]. 3R phase has rhombohedral symmetry with trigonal prismatic coordination with three atomic layers per unit cell. These crystal phases can be characterized in terms of different stacking order of the three planes of transition metal and chalcogen atoms which are involved in the formation of single layer of these materials . The 2H phase corresponds to ABA stacking where A refers to chalcogen atomic layer and B corresponds to transition metal atomic layer. Chalcogen atoms occupy the same position in different atomic layers named as A and lie on top of each other in the direction normal to the layer. Contrary to this, in ABC stacking, chalcogen atoms does not occupy the same position and this type of stacking is present in 1T phase. In both

stacking, transition metal atom is sandwiched between chalcogen atoms. If we look at periodic table, groups IV, V, VI, VII, IX and X contain transition metal elements. Chalcogen elements (S, Se and Te) lie in group XVI of the periodic table. Depending on the specific combination of transition metal and chalcogen atom, 2H, 3R and 1T are thermodynamically stable phases. Apart from these, some other meta-stable phases also exist like orthorohmbic $1T_d$ phase. If we look at group VI Mo and W elements, there are six possible combination of TMDCs formation with S, Se and Te. Out of these six, five can exist as stable 2H phase and meta-stable phase 1T[27][28][29][30]. Only WTe_2 is an exception where room temperature stable phase is orthorohmbic $1T_d$[31][32].

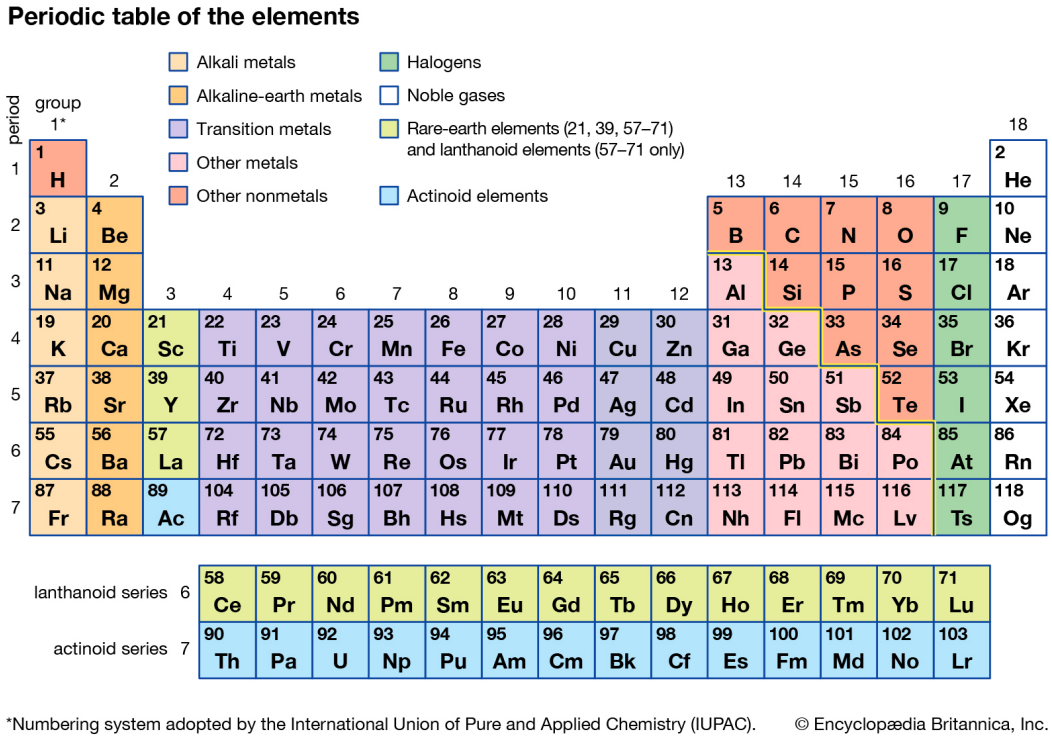

Figure 1.3: Periodic table showing classification of different elements. Each color describe certain type of element. Purple color on this table represents transition metal elements and orange color is representing S, Se and Te along with some other elements. Copyright Encyclopedia Britannica

Apart from these phases mentioned above, TMDCs can also exist in distorted phases like 1T'. In this scenario, metal-metal bond can result in dimerization of 1T phase which ultimately yields formation of 1T' phase. Some of the examples of 1T' phase include $MoTe_2$ and MoS_2[33][34]. Transition from one phase to other is

also possible by different methods. Laser induced transformation from 2H phase to 1T' phase of $MoTe_2$ has been demonstrated by Suyeon Cho et.al[35]. Phase engineering using chemical treatment has already been demonstrated for the case of MoS_2. Treating MoS_2 with n-butyle lithium can assist electron donation in the system which lead to selective phase transformation as can be seen in figure 1.4(b) [36].

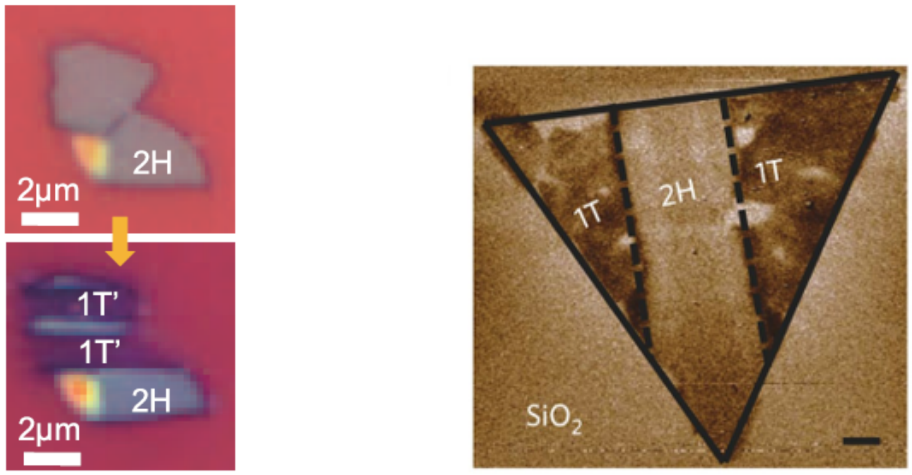

(a) (b)

Figure 1.4: (a) Laser induced phase transformation of $MoTe_2$ from 2H phase to 1T'. Copyright American Association for the Advancement of Science 2015(b) CVD grown 2H-MoS_2 crystal selectively converted to 1T phase upon treatment with n-butyl lithium. Copyright Springer Nature 2014

1.4 Metallic Transition Metal Dichalcogenides

Metallic transition metal dichalcogenides (MTMDC) posses a finite density of state at the Fermi level which is not the case for semiconducting TMDCs. This makes the research field of MTMDCs quite distinguished when compared with STMDCs. MTMDCs can be synthesized with various chemical deposition methods like CVD[37], MOCVD[38], CVT[39], MBE[40] and as simple as mechanical

exfoliation of atomically thin layers of these materials from the bulky counter part[41]. Some of the exotic phenomena that these material exhibit include charge density wave, superconductivity and magnetism. Charge density wave is an ordered quantum fluid of conduction electrons which act as a standing wave and some time may carry electric current. 2H-TaS_2 is one of the exemplary material which exhibits both charge density wave transition and superconductivity at cryogenic temperatures. The external parameters can effect the transitions very significantly. The affect of pressure on these properties has been reported by Hafeiz et.al[42]. As can be seen in 1.5 (a), the kink around 75K represent CDW transition for both in-plane and out of plane resistivity represented by ρ_{ab} and ρ_c respectively. The inset of figure shows superconducting transition beyond temperature 0.9K. Figure 1.5 (b) shows the effect of pressure on the transport properties. The CDW transition becomes insignificant at elevated pressures while the superconducting transition temperature increases from 0.9K(atmospheric pressure) to 4.2K(3.1 GPa) and 9K(8.7GPa) as shown in the inset of same figure.

The onset of superconducting transition can heavily depend on the number of layers of the material. Thickness dependent superconductivity has also been reported in 2H-NbS_2[43]. Figure 1.6 (a) shows resistance vs temperature measurements performed on 2H-NbS_2 crystals with different thicknesses. Superconductivity transition can be observed at a temperature as high as 6K for a crystal of thickness 12nm. Upon decreasing the number of layers, the transition temperature shifts to lower temperature values. For crystals below 6nm thickness, no superconducting transition is observed due to possible inevitable degradation due to oxidation of the material.

Apart from interesting exotic phenomena that exist in MTMDCs, these materials can be used as a promising 2D electrode instead of gold or platinum. Several report have been made to date in which using MTMDCs as electrode material enhanced the performance of 2D material based field effect transistors. Zhang et.al. demonstrated that edge epitaxially grown NbS_2 along the WS_2 flake enhanced the on and off ratio of the fabricated transistor where NbS_2 acted as electrode material[44]. The use of these materials in flexible electronics can also increase the durability of such devices[45].

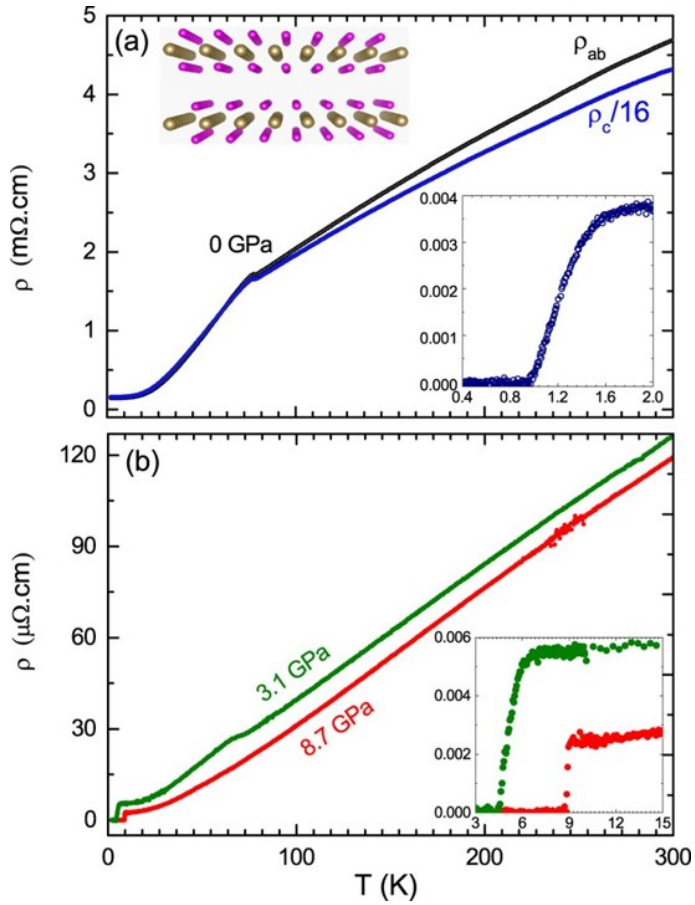

Figure 1.5: (a) In-plan (ρ_{ab}) and out of plane (ρ_c) resistivity plotted as a function of temperature at ambient pressure. The kink shows CDW transition. Inset shows superconducting transition below 0.9K temperature. (b) Resistivity measurements at higher pressure. The CDW transition suppresses at very high pressure while the shift towards higher temperature for superconducting transition is observed(inset). Copyright Springer Nature 2016

1.5 Photocurrent Generation in Semiconducting Transition Metal Dichalcogenides

Upon illumination, almost all semiconducting transition metal dichalcogenides yield photocurrent generation. However, the mechanism that are responsible may vary from material to material. MoS_2 is very well studied member of semiconducting TMDCs. Buscema et.al. showed that the photoresponse in monolayer across metal-semiconductor junction is dominated by photothermal effect which

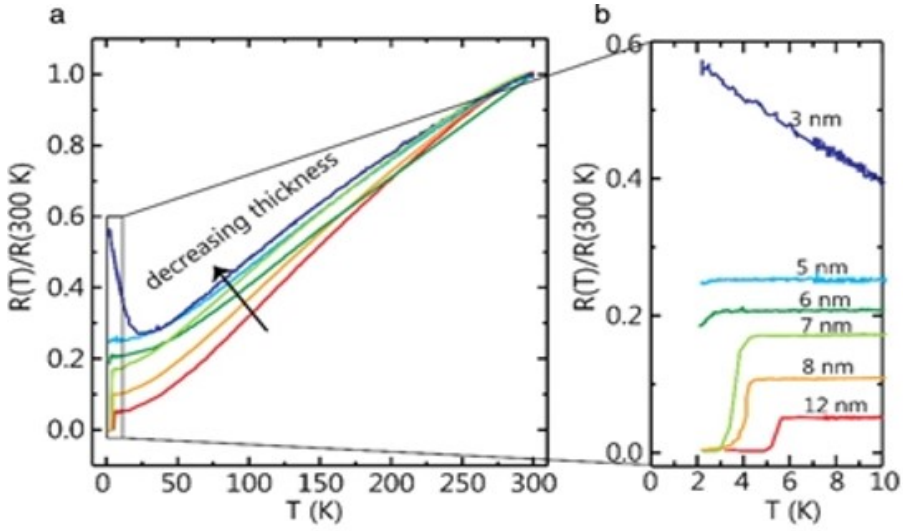

Figure 1.6: (a) Normalized resistance vs temperature plotted for 2H-NbS_2 for various thickness crystals. (b) The data in the rectangular window in (a) to see superconducting transition between 0K to 10K. Copyright IOP Science, The Japan Society of Applied Physics, 2019

results due to the difference in the Seebeck coefficients of MoS_2 and gold[46]. Later on, Chiang Wu et.al demonstrated that at finite applied bias the photocurrent generation in MoS_2 monolayer is due to electric field induced separation of the carriers[47]. Similar studies are reported for several other semiconducting TMDCs as well. The detailed discussion of mechanisms will be provided in the next chapter.

1.6 Thermal Conductivity of TMDCs and Nano-Sheets

Thermal conductivity is characterized by the ability of a material to conduct heat. Several methods in literature have been reported so far to measure thermal conductivity of TMDCs and nano-sheets. Each of the reported methods have its own advantages and disadvantages as compared to each other. 2D materials like

graphene and hexaboron nitride exhibits exceptionally high thermal conductivity as compared to other similar materials[48]. Graphene has a reported value of thermal conductivity in the range of 4800-5300 $Wm^{-1}K^{-1}$ as compared to its bulk counterpart graphite which has thermal conductivity of as high as 470 $Wm^{-1}K^{-1}$[49][50][51]. Reported thermal conductivity of most studied TMDCs like MoS_2 and WS_2 are 34.5$Wm^{-1}K^{-1}$[52] and 32$Wm^{-1}K^{-1}$[53] respectively. Detailed discussion on different methodologies to calculate thermal conductivity of TMDCs and nano sheet is provided in chapter 4.

1.7 Thesis Motivation and Outline

Photocurrent generation has been studied extensively for semiconducting transition metal dichalcogenides with several proposed mechanism in the literature. However, no studies have reported photocurrent generation in metallic TMDCs. As photocurrent generation in metallic TMDCs is unprecedented, the mechanism for such phenomenon required investigation. Few examples in literature exist where photocurrent generation through metallic materials is demonstrated. These include carbon nano-tubes and gold nano-particles. In this thesis, we explore the mechanism which will be responsible for photocurrent generation in metallic TMDCs. We discussed in detail photo-thermal and photo-bolometric origin of photocurrent through metallic TMDCs starting with NbS_2 as an exemplary material. Once we established photo-bolometric origin of photocurrent through metallic TMDCs, we utilized this property to introduce a novel method to calculate thermal conductivity of nano-sheet using photo-bolometric effect. Our proposed method is simple in terms of calculation and device fabrication as compared to other methods that already exist in literature.

First of all, in this thesis, I will discuss several photocurrent generation mechanisms that exist in 2D materials as can be seen in chapter 2. In chapter 3, I will discuss the photocurrent generation metallic TMDCs and governing mechanism. Chapter 4 gives brief introduction to methods of thermal conductivity that has already been reported in literature. In chapter 5, I describe in detail our

proposed method based on bolometric effect to calculate thermal conductivity of nano-sheets along with its pros and cons. Finally, In last chapter I will give concluding remarks regarding our findings during my PhD studies.

Chapter 2

Photocurrent generation and possible mechanisms in 2D materials

When a photo-sensitive device like a photo diode is exposed to a certain threshold radiant power, it results in generation of photocurrent through the device. Based on nature of the material used in the device fabrication, we can have several different mechanism that can explain the origin of current produced upon exposure to radiation. I will be discussing each of these possible mechanism one by one in the below text.

2.1 Mechanisms of photocurrent generation

Generation of photocurrrent in 2D materials can be explained by many mechanisms. Some mechanisms involve electric field driven separation of electron-hole induced by photon absorption. Photoconduction, photovoltaic effect and the photogating mechanisms can fall under this category. Photocurrent can also be generated by a thermal process which may include photothermoelectric and

bolometric effect. Brief discussion on each of the above mentioned mechanisms is discussed below.

2.1.1 Photo-conductive effect

When some non-metallic materials absorb photon energy, they exhibit an increase in the electrical conduction (or reduction in resistance)[54][55][56][57]. Some semiconducting materials which are normally poor electrical conductor can observe increase in their conductivity upon illumination by a certain wavelength light[58]. The incoming photon can interact with the electrons by exciting them and ultimately move them to the conduction band where they can move more freely. This results in enhanced electrical conductivity[59]. This increase in the available free charge carrier makes these materials better conductors upon illumination. The rate of excitation and relaxation of these extra free charge carriers can play a determining role in estimating the change in the conductivity caused by the incident flux of photons[60]. The term describing the excitation and relaxation time is referred as lifetime of the the excited charge carriers. The time these excited charge carriers spend in conduction band before relaxation is termed as lifetime[61].

Fig.2.1 shows schematic of the band alignment of a semiconducting material upon contact with two metal electrodes under applied bias. In Fig.2.1(a), the schematic shows movement of carriers in dark condition under certain applied bias. A small drain source current (I_{dark}) passes through the system. When illuminated by light of energy larger than the band gap ($E_{ph} > E_{bg}$), the electron hole pairs are generated which are separated by the applied voltage bias. The photogenerated free electron hole carriers drift in the opposite direction towards metal electrodes. This in turn results in the enhancement of the conductivity and hence a photocurrent (I_{photo}) of magnitude higher than I_{dark} flows through the system.

When we consider case, where mobilities of both electron and holes possess large difference from each other, it will result huge difference in electron-hole

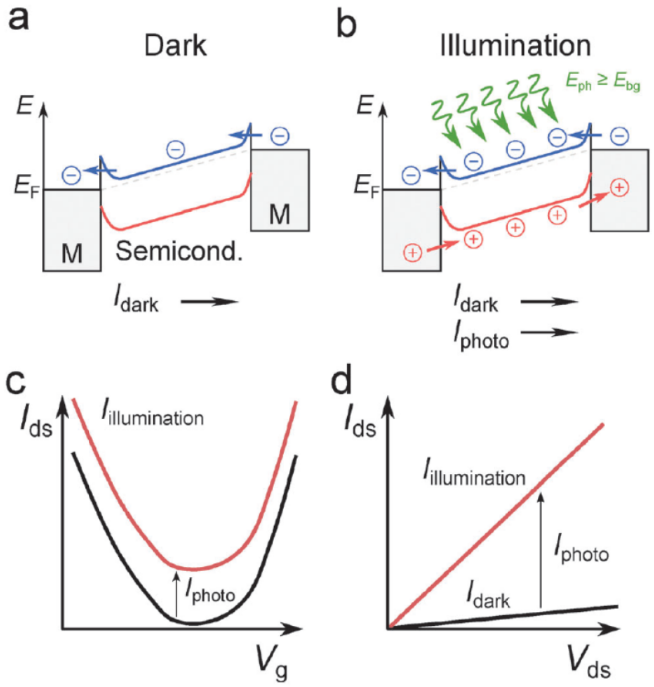

Figure 2.1: (a) Schematic of band alignment when two metal contacts are made to semiconducting material under some applied bias without illumination. (b) Bang alignment under applied bias when a device is illuminated with photons of energy E_{ph} greater than band gap E_{bg}. (c) Current plotted against applied gate voltage with and without illumination. (d) IV plots in dark (black line) and under illumination(red solid line). Reproduced from Ref. [62] with permission from The Royal Society of Chemistry.

transit time which can be referred as $\tau_{transit}$ and is given by equation 2.1[56].

$$\tau_{transit} = \frac{L^2}{\mu . V_{ds}} \tag{2.1}$$

Here, L is the transistor channel lengt, μ is the mobility of charge carriers and V_{ds} is the applied drain-source bias. If the electron mobility is much higher than the hole mobility, the photogenerated electron will pass the channel much quicker as compared to the photogenerated holes. Many electrons can contribute towards photoconductive gain (G) until electron-hole recombination. In simple words, we can say that we can extract more and more electron from a single photon which can result in a quantum efficiency greater than one. The photo-conductive gain

can be defined as the ratio of photo-generated carriers life time and transit time and can be represented by the equation 2.2. It can be clearly seen in the equation that larger value of $\tau_{photocarriers}$ will result in larger value of G[56].

$$G = \frac{\tau_{photocarriers}}{\tau_{transit}} \tag{2.2}$$

2.1.2 Photo-gating effect

Another mechanism which is based on electron-hole separation is photo-gating. It can be considered as special case of photo-conductive effect in which electron or holes can get trapped in local states where they start acting like a local gate which in result modulates the resistance of the material[63][64][65][66]. In this scenario, photo-carrier lifetime is only restricted to recombination life time of the trap states which are localized. Surface of the materials which are semiconducting in nature and defects sites acts as a host for these trap states where these trap states can last for longer period of time. This effect become very significant in materials like colloidal quantum dots, 2D semiconducting materials and nano wires in which electrical properties rely on larger surface and reduced screening[67][68][69].

Fig. 2.2(a) shows band diagram of a semiconducting material in contact with two metal electrodes under applied bias in dark condition. As can be seen, small current (I_{dark}) passes through the system. Upon illumination, generation of electron hole pair occur. As can be seen in fig. 2.2 (b) schematic, hole are trapped at band edge where they act like a local gate. This produces a field effect which in response drives the photocurrent(I_{photo}) through the system. Fig. 2.2 (c) reflects the variation of source drain current(I_{ds}) with respect to applied gate voltage (V_g). There occurs a horizontal shift in the curve upon illumination termed as ΔV_g, also marked on the plot. Solid black line shows response under dark condition while solid blue/red line shows the curve behavior under illumination. Fig. 2.2 (d)shows the IV characteristic curve under dark condition demonstrated by solid black line and under illumination at different applied gate voltage represented by solid red and blue lines. It can be seen that red IV (positive photocurrent) curve

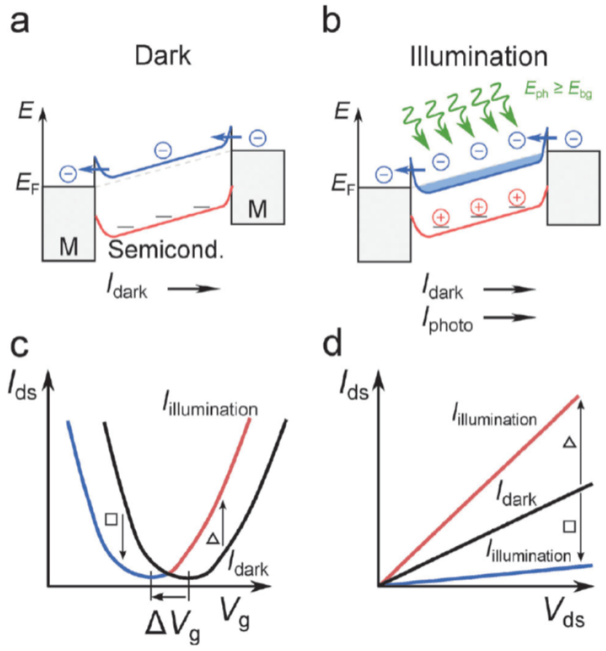

Figure 2.2: (a) Schematic of band alignment when two metal contacts are made to semiconducting material under some applied bias without illumination. (b) Bang alignment under applied bias when a device is illuminated with photons of energy E_{ph} greater than band gap E_{bg}. Holes are shown to be trapped at th band edge. Upon illumination and under applied bias, field effect produces electrons in the channel which contribute towards photocurrent generation. (c) Current plotted against applied gate voltage with and without illumination. (d) IV plots in dark (black line) and under illumination(red and blue solid lines). Reproduced from Ref. [62] with permission from The Royal Society of Chemistry.

is obtained by the gate values used from the triangle marked range in fig. 2.2 (c) while blue IV curve (negative photocurrent) is obtained by square marked range in the panel c.

Practically, both photoconductive and photogating effect are not easily distinguishable. They may co-exist in the same system. However, Furchi et al successfully demonstrated that both effect can be distinguished based on their difference in the time scales[70].

2.1.3 Photovoltaic effect

When an internal electric field separates the photogenerated electron-hole pair, then this effect is called photo voltaic effect[71][72][73]. This internal electric field can originate from the formation of PN-junction or a schottky barrier at the metal and semiconductor interface as can be seen in fig.2.3(a). IV characteristic curve exhibits non-linear behavior in both of these junction formation under dark condition. In PN junction formation, the forward bias current increases exponentially as given by relation in equation 2.3 [74].

$$I_{ds} \propto e^{V_{ds}} - 1 \tag{2.3}$$

In reverse bias configuration, negligibly small current pass through the device until the break down voltage of the junction. When the device is illuminated under zero applied bias, the photo excited electron-hole pairs gets separated by the internal electric field. This in response produces significant amount of photo-current which can be referred as short-circuit current(I_{sc}). If the circuit is kept open, the charge carriers with opposite polarities can be restricted in different parts which in response will lead to generation of a voltage. This net voltage is termed as open circuit voltage(V_{oc}). When we illuminate the device and apply reverse bias, an increase in reverse current is observed as the junction electric filed sweeps the photoexcited charge carriers in the opposite direction. Compared to photoconducting effect, in photovoltaic effect, generated photocurrent can be converted to electrical power[75].

Current vs voltage graph of the PN junction both in dark (solid black line) and under illumination (solid red line) is shown in the fig. 2.3(b). The curve under illumination appear shifted downwards when compared to dark current curve as the generated photocurrent has similar sign as the reverse bias current. It is worth noting that the portion of the curve lying in the lower left quadrant of the plot where the current has negative values under positive applied bias, can be used to calculate maximum electrical power as indicated by P_{el}^{max} on the plot.

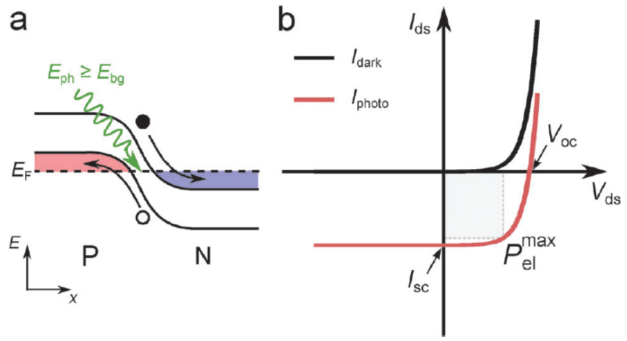

Figure 2.3: (a) Schematic of a PN-junction formation. Common fermi energy (E_f) level for both P and N doped semiconductor can be seen in the schematic represented by dashed black line. The incident photon of energy larger than band gap of the material (E_{ph}¿ E_{bg}) generates the electron hole pair as represented by black and white dot respectively. The built in electric field at the PN-junction then separates the electron hole pair and gets accelerated. (b) I_{ds} vs V_{ds} curves plotted in dark and under illumination represented by black and red lines respectively. A short circuit current due to open circuit voltage is generated in the device upon illumination. An electrical power is generated by the device indicated by P_{el}^{max} (maximum power). Reproduced from Ref. [62] with permission from The Royal Society of Chemistry.

2.1.4 Photo-thermoelectric effect

When a heat gradient is generated through a material by light induced heating, there will appear a temperature gradient between the two ends of the material. This temperature gradient can be termed as ΔT. This ΔT can be converted to a potential difference because of the Seebeck effect or photothermal effect[76]. This potential difference is linearly proportional to the temperature gradient and can be expressed by the equation

$$\Delta V = -S.\Delta T \tag{2.4}$$

Where S is the seebeck coefficient.

The temperature gradient can be created with focused laser spot locally whose dimensions are much smaller than the whole device[77]. Global illumination can

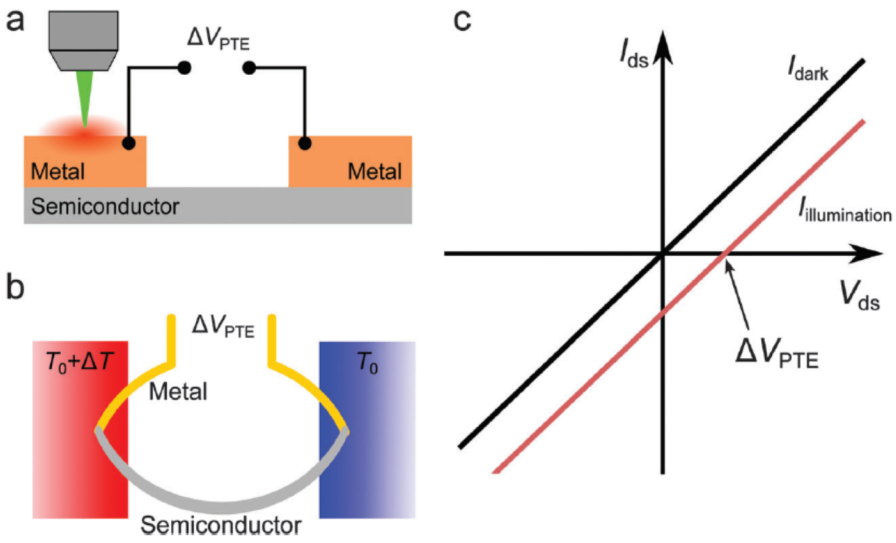

Figure 2.4: (a) Schematic of a FET which is being illuminated locally using a focused laser spot at one of the metal-semiconducting junction. The configuration represent the open circuit case where the thermoelectric potential is generated between the two junctions. (b) represents the circuit diagram of the same device depicted in (a). (c) IV characteristic curve in both dark (black) and under illumination(red) are plotted. Under zero bias, a current is generated in the system driven by the thermoelectric potential difference(V_{PTE}). Reproduced from Ref. [62] with permission from The Royal Society of Chemistry.

also generate such regions of temperature gradients in a material which exhibits different absorption of photon energy in different part of the device[78].

Due to photo-thermoelectric effect, a temperature gradient generates a potential difference through the device which in response can drive current through the system even under zero applied bias. A schematic of such device is shown in fig. 2.4(a) where two junctions are maintained at different temperatures by the aid of focused laser spot. A potential difference (V_{PTE}) is generated due to this constant temperature gradient between the two junctions which can be expressed by the equation 2.5[79].

$$\Delta V_{PTE} = (S_{semiconductor} - S_{metal}).\Delta T \tag{2.5}$$

In this equation, we can neglect the term $S_{metal}.\Delta T$ because of smaller values of seebeck coefficients of metals as compared to semiconducting materials. The estimation of ΔT can be done using finite element analysis methods or incorporating on chip thermometers on the device[80][81]. After knowing the value of ΔT, the corresponding Seebeck coefficient can be estimated. Potential difference values generated by photothermal effect can range from tens of micro-volts to tens of mili-volts. It is important to have ohmic contact formation in order to observe photo-thermoelectric effect. In a scenario, where illumination is on top of uniform semicoducting channel, no current will flow through the device as there is no bias applied to system. Also, the temperature gradient will be negligibly small in this case and the required potential difference will not be created to drive the current.

IV curves of a device in which PTE is dominant is shown in fig. 2.4(c). As the curve under dark condition exhibit linear behavior giving strong indication of formation of ohmic contacts with negligibly small schottky barrier. When the device is illuminated, current at zero applied bias is observed with out changing the resistance of the device due to the photothermoelectric effect. Intersection of red curve with the zero current axis give the value of ΔV_{PTE} as indicated by black arrow in fig. 2.4(c).

2.1.5 Photo-bolometric effect

When the uniform heating induced by photon absorption ultimately change the resistance of the material, such effect is termed as photo-bolometric effect[82][83]. This effect has direct relationship with the change of conductance of a material with temperature (dG/dT) and uniform increment in the temperature by the laser induced heating of the material. Many IR detectors works based on this principle in a four terminal configuration which enhance the detectivity of the operational device[84].

Chapter 3

Photo-current generation in metallic transition metal dichalcogenides

Several mechanisms play their role in generation of photocurrent in 2D semiconducting layered materials[85][86]. These mechanism may involve photothermal effect, photovoltaic effect, photoconduction and photogating. I have discussed briefly all these mechanism in the previous chapter. Apart from few exceptions, the above mentioned mechanisms do not result photocurrent generation in metallic materials. As the thermal conductivity of metallic materials is generally higher and have low absorption of optical excitation, the photothermal effect becomes very insignificant in these materials. Also, Under certain applied bias, electron that are being excited optically in metals will have negligible contribution towards the already existing huge number of intrinsic electron close to the Fermi level. Some of the metallic systems in which photocurrent generation has been reported include gold nano particle network[87], graphene[85][88] and metallic carbon nanotubes[89]. As photocurrent generation in metallic transition metal dichalcogenides(TMDCs) is not expected, the possible mechanism for such phenomenon has not been explored so far. In this chapter, I will be discussing photocurrent generation through mechanically exfoliated Niobium Disulfide(NbS_2)

using scanning photocurrent microscopy. According to our findings, the photocurrent generation in such system is mainly due to photothermal effect and will be discussed in detail later in this chapter.

3.1 Experimental methods

3.1.1 Bottom contact devices

Bottom contact devices are fabricated by transferring selected crystal on top of pre-patterned gold electrodes. In these devices, the gold electrode are lying under crystal making contact to the bottom side of the crystal. This is why these devices are referred as bottom contact devices. The fabrication process is described in detail in the following sections.

3.1.1.1 Mechanical exfoliation

3R-NbS_2 bulk source is purchased from HQ graphene. The bulk source is pasted against a yellow kapton tape and peeled off very carefully using clean tweezers to avoid any contamination. This will leave layers of the pasted material onto the tape. The tape containing NbS_2 crystals is pasted against a cleaned 280nm SiO_2/Si chip and placed on hot plate heated to 90^0C for 1 minute. Then the tape is peeled off from the SiO_2/Si substrate leaving behind exfoliated crystals of NbS_2 onto the substrate. The sample is observed under microscope in order to target a suitable crystal for device fabrication.

3.1.1.2 Optical lithography and metal evaporation

Gold electrodes are pre-patterned onto a clean 280nm SiO_2/Si substrate using optical lithography. First of all the sample is rinsed with acetone, iso-propanol followed by thorough rinsing with DI water. The substrate is placed onto hot

plate set at 120^0C for 10 minutes to get rid of all possible moisture. Positive toned photo-resist AZ-5214 is spin coated onto the cleaned substrate at 4000rpm. The sample is then placed onto hot plate for soft bake to activate the photo-resist. The chip containing photo-resist is exposed to UV light mounted onto a mask aligner under a mask containing desired features. The dose of exposure is set to 40mJ/cm^2. After exposure, the chip is dipped in developer AZ-400K. The developer is a solution of 20mL AZ-400k in 80mL water which make it 1:4 solution. The optimized development time is 45 seconds. After that the required feature are patterned onto the desired substrate. Followed by this, we evaporate gold as metal contact material. 5nm chrome is first deposited as an adhesion layer for gold using thermal evaporator. 100nm gold is then deposited which act as electrodes after the successful lift-off. Fig.3.1 shows final result of electrodes patterned following the above mentioned procedure.

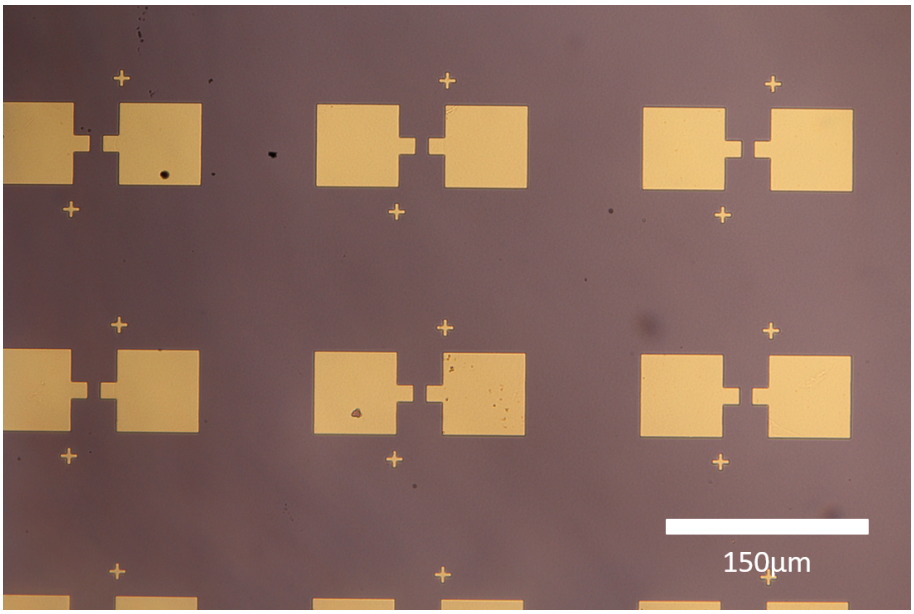

Figure 3.1: Array of two terminal electrodes patterned using optical lithography

3.1.1.3 Deterministic crystal transfer

Selected crystals after mechanical exfoliation are transferred on top of pre-patterned electrodes deterministically using a polymer film. We use poly-carbonate(PC) as a polymer for this purpose. A small piece of thin PC film

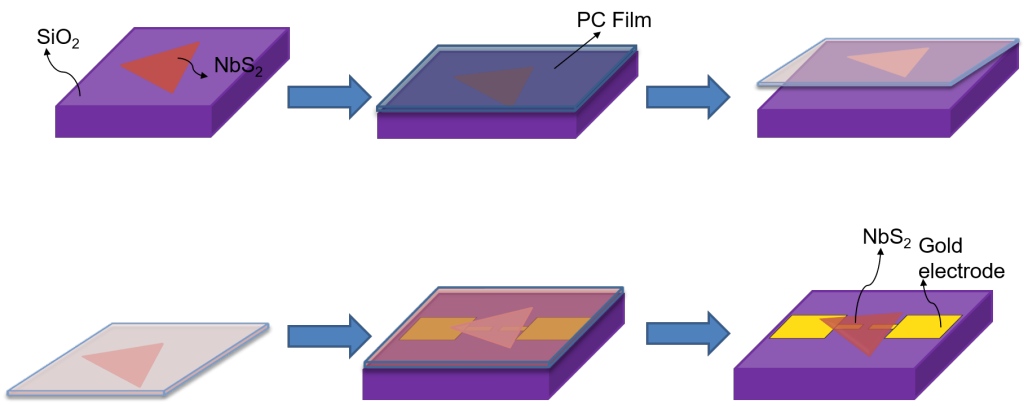

Figure 3.2: Schematic of the deterministic crystal transfer starting from mechanical exfoliation of the NbS_2 till the selected flake aligned and transferred on top of metal electrode.

is cut and placed on top of our desired crystal. The film is allowed to melt by increasing the stage temperature to 165^0C. Once the film is melted, the sample is removed from the stage and the PC film solidifies again. The film is carefully peeled from the substrate which will pick up our desired crystal from the substrate. This film then placed on the pre-patterned substrate containing several gold electrode. The film is then manipulated using a fine needle mounted on a micro-manipulator to align our desired crystal accurately with the electrodes. Once the crystal is aligned, the stage temperature is increased again to melt the PC film again. This step will make sure that our film does not move once we put it into organic solvent for dissolution of the PC film. The sample is then immersed in chloroform to dissolve PC film for 15 minutes. The samples is removed very gently from chloroform solution after 15 minutes and observed under microscope. Schematic of the whole process can be seen in figure 3.2. Optical microscope and scanning electron microscope images of the fabricated devices can be seen in figures 3.3 and 3.4 respectively.

Figure 3.3: Optical microscope images of back contact devices. scale bar is 30μm

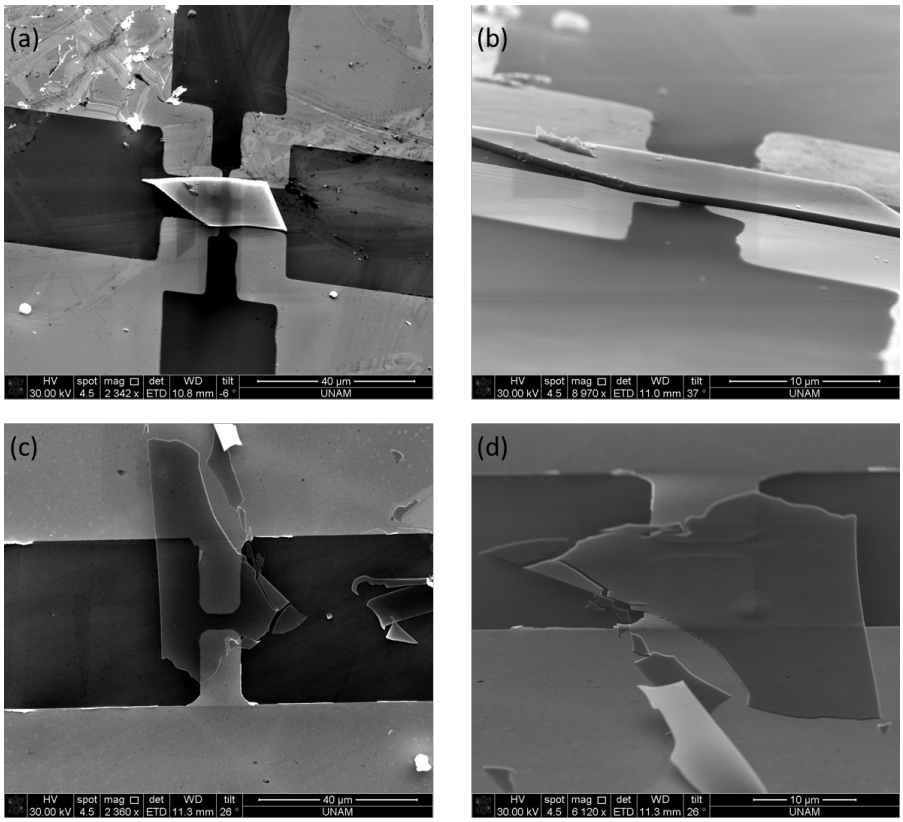

Figure 3.4: Electron microscope images of back contact devices showing top view and side view of the devices.

3.1.2 Top contact devices

In top contact devices, the gold electrodes are deposited on top of selected crystal. In order to obtain such devices, I utilized two different lithography techniques.

1. Optical lithography
2. Electron beam lithography

3.1.2.1 Optical lithography

After doing mechanical exfoliation of the selected material, a suitable crystal is chosen to put metal contact on top of it. The orientation along with the location of the crystal is roughly noted under microscope. If needed a scratch mark is placed near the crystal using a diamond scriber. It helps in locating the crystal under mask aligner in a more efficient and less time consuming way. The patterning parameters are same as described in section **3.1.1.2**. After spotting the crystal under the mask aligner, the crystal is aligned with the electrode terminals followed by UV exposure. After development, the patterned crystal is observed under microscope. If patterning is successful, the sample is placed safely in a container and more similar samples are prepared for metal evaporation. After metal evaporation and successful lift-off process, we observe fabricated devices under microscope.

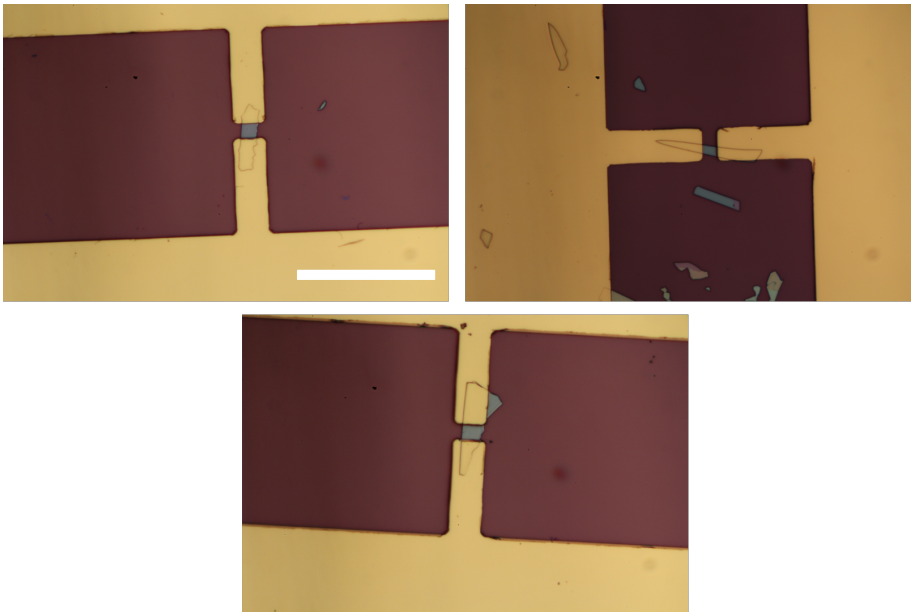

Figure 3.5: Optical micrographs of the fabricated devices top contact devices using optical lithography. Scale bar is 30μm

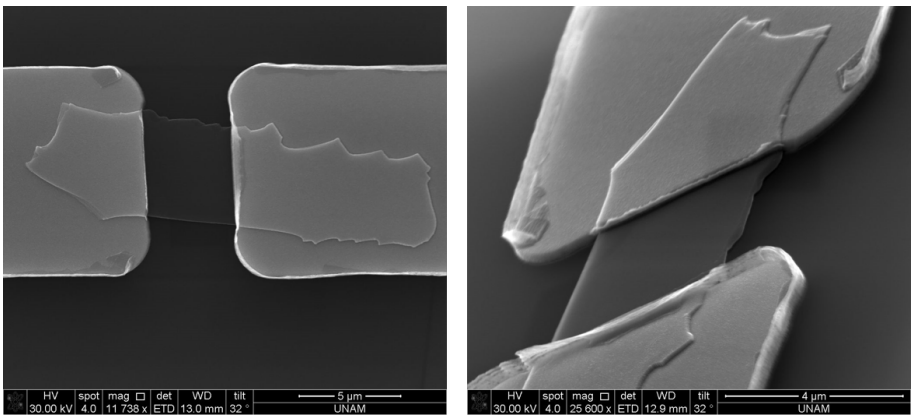

Figure 3.6: Electron microscope images of top contact devices showing top view and side view of the selected device.

3.1.2.2 Electron beam lithography

Some of the devices in this study are fabricated using electron beam lithography. It is a direct writing technique which does not require any physical mask for patterning and we can control the dimensions of each pattern separately that we want to print. This technique can easily have a nano-meter precision in patterning. It is a two step electron beam lithography process. In order to be able to pattern, mechanical exfoliation of desired material is performed on a rectangular chip with flat sides and sharp corner. We can choose one sharp corner of the chip as origin and get the coordinates of the crystal lying on the chip using an on-screen digital ruler named MB-ruler. The precision of the coordinates can be of the order of few tens of micrometer.

In next step, spin coating of electron resist is performed. We use polymethyl methacrylate(PMMA) resist for this purpose. A double layer of two different type of PMMA resist is spin coated. First layer is spin coated PMMA 495(A6) at 4000rpm for 60 seconds followed by a prebaking step for two minutes at a temperature of 180^0C. After this another layer of PMMA 950(A6) is spin coated following similar parameters followed by same duration of baking at 180^0C.

First of all, four alignment cross marks along with three squares are patterned in the vicinity of the target crystal. As sample is coated with electron beam resist, we can not image the crystal in the electron microscope. We use these alignments crosses and squares to match with the actual design prepared as a GDS file in K-Layout software. Once these alignment marks are match perfectly with the actual GDS design, we can draw the desired features and electrodes on the same file. We used EFI Nova 600 NanoSEM for our electron beam lithography process. The used voltage for our process is 30KV to ensure maximum penetration depth. The beam current is chosen according to the feature size. For smaller feature of the order of 2 to 3 μm I used 52pA. For larger features of the order of 100 to 300 μm, I used 80nA. The dose was chosen to be $100\mu C/cm^2$.

The development of exposed resist is done in a developer solution of

MIBK(methyl isobutyl ketone) and IPA(isopropyl alcohol) in ratio of 3:1. Sample is dipped in this solution for 65 second followed by rinsing with IPA for 15 seconds and 20 seconds with DI water. The sample is finally nitrogen dried.

After development, the image of printed alignment marks is captured using optical microscope. This image is used to prepare design in computer software name K-Layout. Spatial orientation is determined using the three squares patterned on the sample and fine adjustments are made using much smaller four crosses. This is all done to have exact match of patterned alignment marks and actual design of the alignment marks prepared on K-Layout software. As these alignment marks act as a coordinate system, any feature designed on the K-layout software in any specified orientation will ultimately be patterned in EBL exactly how we prepared the design. Finally, the exposed regions are developed in developer just like alignment marks development as mentioned earlier.

3.1.3 Current vs voltage measurements

Current vs voltage measurements are performed on a home built probe station. Tungsten needles are used as the probes to make connection with the electrode pads. Probes are connected to a preamplifier which act as a bias source. One probe is connected to the ground of the pre-amplifier and the second probe is connected to bias source of pre-amplifier. The current pre-amplifier is integrated with a DAQ (Data Aquisition card) card and controlled with Labview program. Under a bias sweep the current passing through the device is measured and plotted to get the resistance of the device.

3.1.4 Scanning photocurrent microscopy

Scanning photocurrent microscopy(SPCM) is a technique to obtain the spatial mapping of the photoresponse of a chosen material. A device with metal contacts is raster scanned by a focused laser spot to obtain the photocurrent maps. The

experimental setup is comprised of a modulated laser beam at a certain frequency f. Lock-in amplifier uses this frequency and input of the lock-in amplifier is connected to the output of the current pre-amplifier in order to measure the signal generated by the laser beam scanning. The scanning speed and integration time are adjusted accordingly. In our measurements, we used integration time of 3ms. It physically means that if the generated photoresponse by any mechanism is greater than 3ms, it can be feasibly measured.

A commercially available inverted microscope setup is used for the SPCM measurements with all the optic components compacted in a single column assembly. The whole microscope assembly can move over the sample to achieve the scanning purpose. A 40x objective is used to focus the laser beam on to the sample with a spot size of 400nm (532nm laser wavelength). The step size can be controlled with a Labview program. In our study we used fine scans down to 100nm step size. Both Photocurrent maps and reflection maps are recorded using a labview program. For reflection maps, the reflected light from the sample during the scan is detected by a silicon detector. In order to collect data, the Labview program that we use is capable of performing following tasks

- Scanning in x-y direction
- Controlling scan size and step size
- Collecting and plotting of data in real time
- Exporting the collected data as an ASCII file

After collecting the data from Labview program, the data analysis is performed on Origin software for all of our measurements.

3.2 Results and discussion

3.2.1 Material Characterizations

We performed SPCM experiments on mechanically exfoliated niobium disulfide (NbS_2). NbS_2 belongs to family of metallic transition metal dichalcogenides which we chose as an exemplary material for our study. NbS_2 exists in two layered polymorphs named 2H(hexagonal) and 3R(rhombohedral). For our study, we chose 3R poly-type schematic of which can be seen in Figure3.7. While both polymorphs are metallic[90], only 2H phase exhibits superconducting transition at cryogenic low temperatures[43].

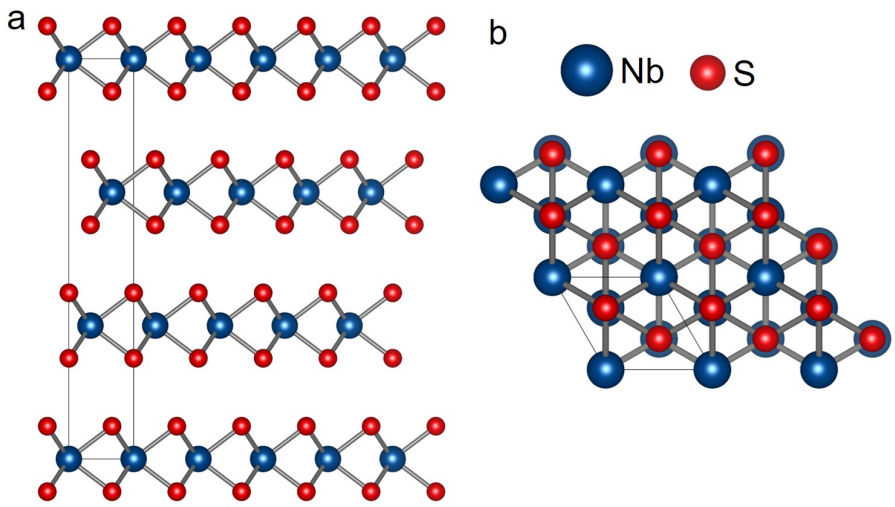

Figure 3.7: Schematic of the side view (a) and top view (b) of the crystal structure of 3R-NbS_2. Reproduced from ref. [91]. Copyright American Physical Society 2018

Raman spectrum of mechanically exfoliated 3R-NbS_2 can be seen in Figure 3.8. Peak positions A_1 ($383cm^{-1}$) and A_2($451cm^{-1}$) corresponds to out of plane vibration modes of the molecules. E_1 ($324.75cm^{-1}$) and E_2($285cm^{-1}$) corresponds to in-plane vibration modes of the molecules. All these marked peak values matches very well with the reported values in literature for 3R-NbS_2[92]. Energy dispersive x-ray spectroscopic (EDS) measurements are performed to confirm chemical composition of the exfoliated crystals. EDS maps of the crystal are

shown in Figure 3.9. Yellow and purple EDS maps correspond to the sulfur and niobium respectively. From the intensity of the maps, we can extract the ratio between niobium and sulfur atoms to be 1:2. The inset at the center shows SEM image of the same NbS_2 flake. Figure 3.10 (a) shows low resolution transmission electron microscope(TEM) image of NbS_2 flake transferred onto a TEM grid. The selected area electron diffraction(SAED) pattern can be seen in Fig. 3.10 (b). Using SAED, we calculated the in-plane lattice constant to be 0.333nm which is in good agreement with the reported value in the literature[93].

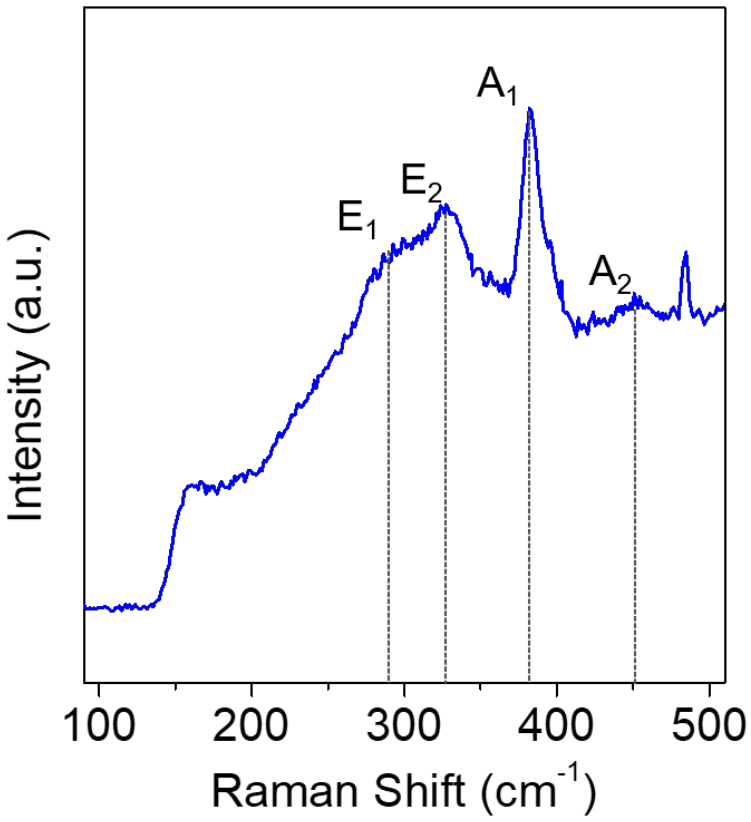

Figure 3.8: Schematic of the side view (a) and top view (b) of the crystal structure of 3R-NbS_2. Reproduced from ref. [91]. Copyright American Physical Society 2018

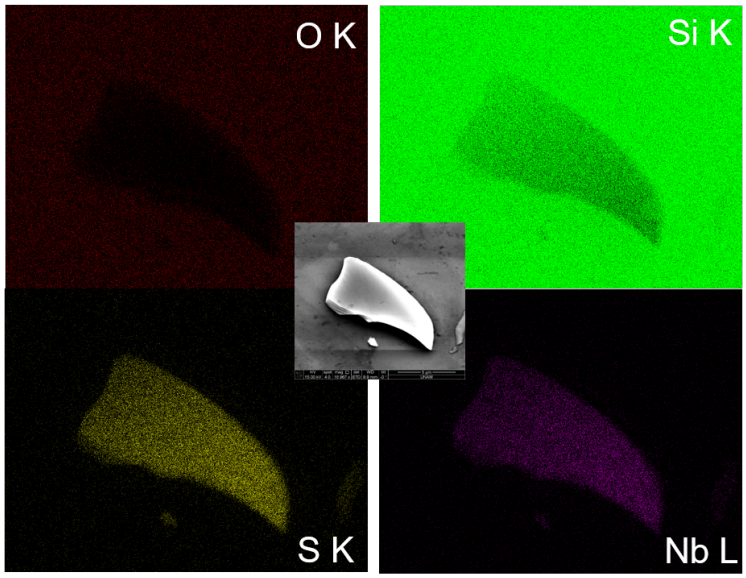

Figure 3.9: Schematic of the side view (a) and top view (b) of the crystal structure of 3R-NbS_2. Reproduced from ref. [91]. Copyright American Physical Society 2018

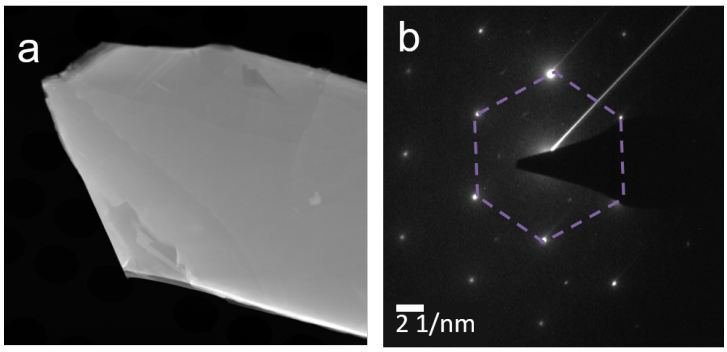

Figure 3.10: (a) Low resolution transmission electron microscopy image of NbS_2 flake. (b) Selected area diffraction pattern from the same crystal. Reproduced from ref. [91]. Copyright American Physical Society 2018

3.2.2 Top contact devices

First of all, I will discuss results of experiments performed on top contact (TC) devices. Fabrication of these devices have been discussed in details in section **3.1.2**. Figure 3.11 shows the scanning electron micrograph of a TC device on which electrical configuration for the measurements has been drawn. Laser beam schematic is also sketched which raster scans the whole sample in x-y direction. The same configuration has been used for all devices in this study. The left terminal is set to ground and right terminal is used to flush bias through it.

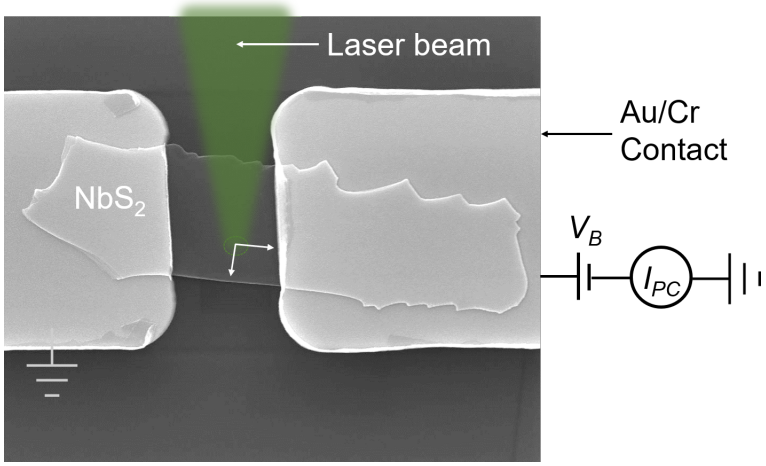

Figure 3.11: SEM micrograph of two terminal device with measurement configuration depicted on it. A diffraction limited laser spot raster scans the samples in x-y direction. In all our experiments, left electrode is grounded and the bias is applied from the right electrode. Reproduced from ref. [91]. Copyright American Physical Society 2018

Figure 3.12(a) shows optical image of the measured device named TC-1. 532nm wavelength laser focused to a diffraction limited spot is used to obtain reflection and photocurrent maps with a laser power P=85μW as can be seen in figure 3.12 (b-c). Resistance vs temperature measurements performed on TC-1 can be seen in figure3.12 (d). It shows room temperature resistance value of around 21.5Ω. As we decrease the temperature, the resistance of the device decreases which confirms the metallic nature of the NbS_2 crystal. Thickness of the crystal is determined my atomic force microscopy. As can be seen in Figure 3.13, there is a slope in the height retrace so we took the average value extracted from the

height profile which is approximately 180nm.

Photocurrent maps obtained under zero applied bias reveals that the maximum intensity of the current is generated at the junction of NbS_2 with the deposited gold metal electrodes. As we are dealing here with metal/metal junction, the generated photocurrent must have photothermal origin and any other mechanism is not likely to be responsible for this photo-induced current generation.

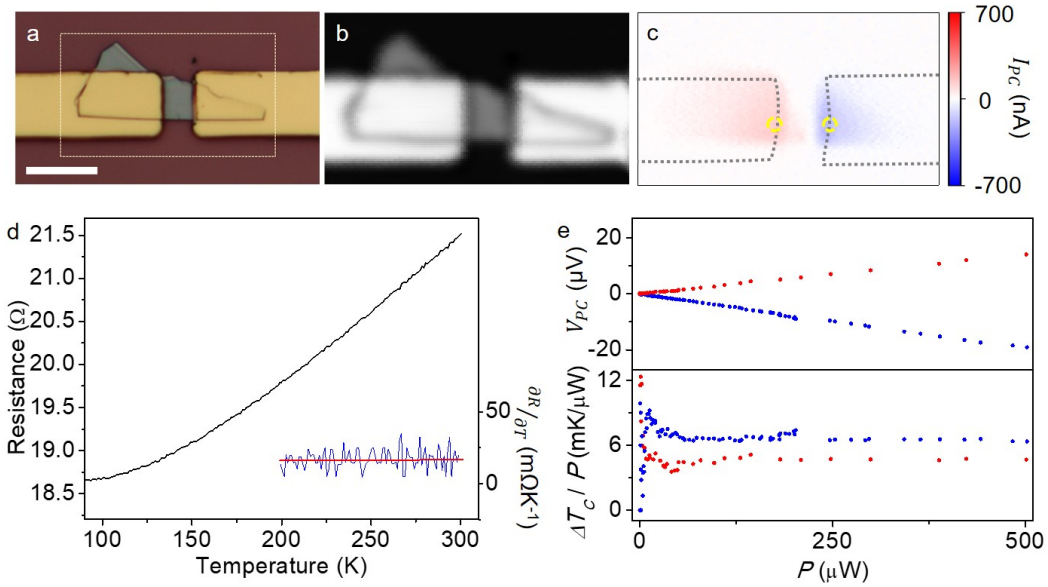

Figure 3.12: (a) Optical micrograph of the TC1 is shown with marked square region in which SPCM is performed. Scale bar is 10μm (b) Reflection map obtained by scanning the laser on top of the device and (c) corresponding photocurrent map under zero applied bias. The photocurrent is confined around the edges which are marked by the dashed black lines. (d) Resistance vs temperature plot of the same device showing characteristic metallic behavior. The inset shows ∂R/∂T as a reference. (e) Upper panel shows V_{PC} plotted as a function of laser power The measurement is taken from NbS_2 metal junction marked by yellow dashed circle on the photocurrent map. Red and blue points from left and right electrodes respectively. By using V_T vs P data, calculated ΔT_C/P is plotted in the lower panel. Reproduced from ref. [91]. Copyright American Physical Society 2018

Let us discuss the photocurrent generation in TC-1 under zero applied bias in more details. The Seebeck effect is responsible for the generation of a thermoelectric electromotive force (V_T) because of the lattice temperature difference ΔT_C produced between the two electrodes due to laser induced heating over one of the

electrodes. Mathematically, this can be written as equation 3.1. Here, $\Delta S_{Au/NbS_2}$ is the difference between the Seebeck coefficient of the gold and NbS_2. Using the values of the Seebeck coefficients of gold and NbS_2 reported in literature, -4μV/K and 2μV/K repectively[94][95], the difference between them can be written as $\Delta S_{Au/NbS_2} = S_{Au} - S_{NbS_2} \approx$ -6μV/K.

$$V_T = -\Delta S_{Au/NbS_2} \Delta T_C \tag{3.1}$$

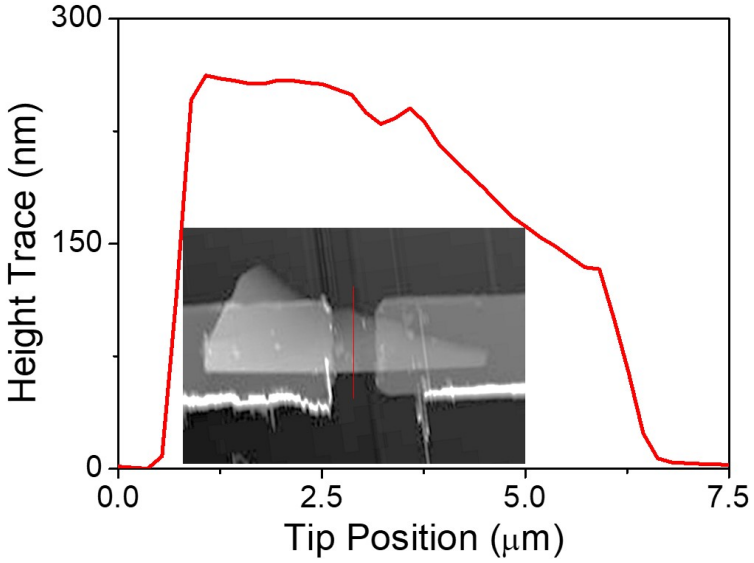

Figure 3.13: Atomic force microscopy image along with height profile along the vertical red line. Reproduced from ref. [91]. Copyright American Physical Society 2018

As we focus laser on left junction, the maximum generated emf can be written by the equation 3.2 where R is the 2-terminal resistance and I_{PC} is the generated photocurrent. The values of maximum emf generated at the junction is calculated as 4.5μV. The corresponding photocurrent generated at both right and left junction is calculated as -130nm and 150nm respectively. By comparing the V_{PC} to V_T, the calculated temperature change (ΔT_C) at both right and left junction is 0.54K and 0.46K respectively. For the laser power 85μW, corresponding ΔT_C/P for right and left junctions are 6.3mK/μW and 5.5mK/μW respectively. These calculated values of ΔT_C/P are of similar order as has been reported in literature[96].

$$V_{PC} = RI_{PC} \tag{3.2}$$

In order to check if we get consistent response from the device at different laser powers, we parked the laser at the NbS_2/metal junction where the photocurrent was minimum and maximum. This can be seen in Figure 3.12 (c) by the dashed circular yellow marks. A variable neutral filter was used to tune the laser power. The laser power was read simultaneously through a 50:50 beam splitter. In figure 3.12(e), V_{PC} is plotted against increasing laser power. As can be seen from the figure, for both junctions we observed that V_{PC} increased linearly with increasing laser power in a similar fashion. Corresponding calculated temperature increase per unit laser power (Δ T_C/P) is plotted in lower panel of figure 3.12(e) against increasing laser power. At both junctions, Δ T_C/P stay invariant with increasing laser power and shows very similar value with a small difference. This small difference can come from difference in gold edge at opposing junctions and also due to positioning of the laser spot.

Now we will discuss the photo-response under applied bias. When we apply bias, the photo-response of NbS_2/metal junction shows significant change. Also, now we observe photocurrent generation throughout the crystal between the metal electrodes. Photocurrent maps of TC-1 under -50mV and 50mV applied bias can be seen in figure 3.14 (a) and (b) respectively. Upper panel of figure 3.14 (c) shows line trace through middle of device at several finite biases. Photoconductance, as can be seen in lower panel of figure 3.14(c), can be calculated by the formula given in equation 3.3

$$G_{PC} = \frac{I_b - I_0}{V_b} \tag{3.3}$$

Where I_b is photocurrent at any applied bias V_b and I_0 is photocurrent under zero applied bias. For all applied biases, photoconductance remains invariant and will be explained in coming paragraph.

The photoresponse coming from all over the flake can be explained by local

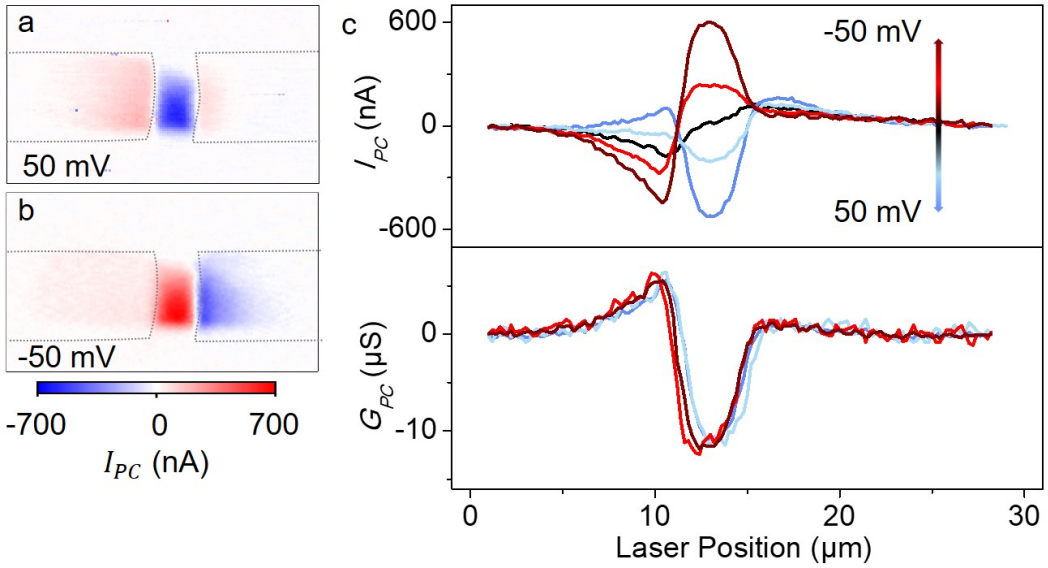

Figure 3.14: (a) Photocurrent map of TC-1 under 50mV applied and (b) -50mV applied bias. The photocurrent is generated from whole crystal between the metal electrodes. (c) Upper panel shows line trace of the photocurrent intensity map going from one electrode to other through center of the crystal for applied biases -50mV, -20-, 0-, 20- and 50mV. Lower panel shows the corresponding bias independent photo-conductance. Reproduced from ref. [91]. Copyright American Physical Society 2018

temperature change caused by laser heating and can be written as ∂T_l. The focused laser beam will increase the temperature of the crystal locally which will cause electrical conductivity to decrease at and in the vicinity of the laser spot. As the dc current due to applied bias will decrease because of laser heating, it will lead to negative photoconductance. As this decrease in conductivity is only being caused by temperature rise due to laser heating, applied bias will have no effect on the conductivity change. For this specific reason, the photoconductance here is bias independent.

We calculated the change in resistance caused by the laser heating. Figure 3.15 shows schematic of device parameter for δT_l calculation. Here we assume that the temperature rise will occur inside a disk of 1μm spot size of laser beam uniformly and outside that temperature rise will be zero. As the laser spot is diffraction limited and has a Gaussian profile, the approximation we made is not bad at all.

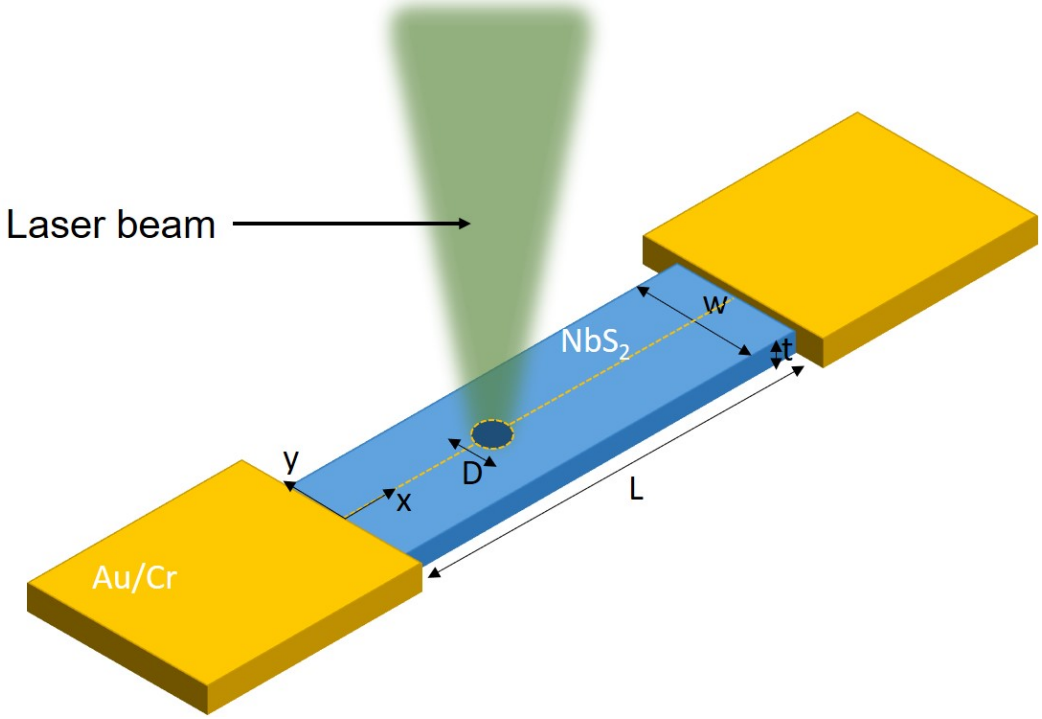

Figure 3.15: Schematic model showing different parameters used to calculate ∂T_l using a python code. Reproduced from ref. [91]. Copyright American Physical Society 2018

To make our calculations less complicated, we choose laser spot at the middle of the crystal which is at a distance of x from the metal electrodes. We choose coordinates of the laser spot as (x,0). D is the diameter of the laser spot. Inside this diameter, the resistance will have different value as compared to rest of the crystal. Considering infinitesimally small piece of crystal which passes through the laser beam, the change in resistance across the contacts can be written as equation

$$dR = \rho_0 \frac{x_i}{A} + \rho_0 \frac{L - x_f}{A} + \rho_T \frac{x_f - x_i}{A} \tag{3.4}$$

ρ_0 is the room temperature resistivity. ρ_T is the resistance of the crystal under the laser spot. L is the length between the metal electrodes. Cross-sectional area of the crystal is given A. $x_f = D + \sqrt{D^2 - y^2}$ and $x_i = D - \sqrt{D^2 - y^2}$ correspond to the edges of laser beam disk in which temperature rise occur along

x axis. Based on our resistance vs temperature measurements, the slope $\partial\rho_T/\partial T$ is determined around room temperature. Here we can write $\rho_T = \partial T_L \frac{\partial\rho_T}{\partial T} + \rho_0$. We can write the total conductance of the crystal as sum of infinitesimally small pieces of resistance connected together under laser illumination as equation

$$\frac{1}{R_T} = \frac{y_1 t}{\rho_0 L} + \frac{(w - y_2)t}{\rho_0 L} + \int_{y_1}^{y_2} \frac{t dy}{\rho_0(L - (x_f - x_i)) + \rho_T(x_f - x_i)} \tag{3.5}$$

w is the total width of the crystal. t represents thickness of the crystal that we measure using atomic force microscopy. Defining the limits as $y_1 = 0$ to $y_2 = D/2$ and evalutaing the integral followed by multiplying the result by 2 is similar to evaluating integral under limits $y_1 = -D/2$ to $y_2 = D/2$.

$$\frac{2}{R_T} = \left[\frac{\sigma\pi/4 - \sqrt{2}b tan^{-1}(\sqrt{2}\frac{b}{\sigma}) + \sqrt{2}b tan^{-1}(\frac{a.D}{\sqrt{2}\sigma})}{a.\sigma} + \frac{1}{2}\frac{w - D}{\rho_0 L} \right] .t \tag{3.6}$$

Based on equation 3.6, we wrote a python code to calculate the estimated temperature rise $\delta \mathrm{T}_l$. We tune the value of $\delta \mathrm{T}_l$ in order to obtain I_{PC}. If the calculated I_{PC} matches with the value obtained through experiments, that specific value of $\delta \mathrm{T}_l$ will be our temperature rise caused by laser heating. For the device TC-1, the calculated value for temperature rise per applied laser power is 40mK/μW. This value is higher than the value calculated for the NbS_2/metal junction. It is expected as the crystal is contact with SiO_2 which has poor thermal conductivity as compared to gold. So the heat dissipation through SiO_2 will be significantly less causing the temperature rise to increase as compared to NbS_2/metal junction.

3.2.2.1 Indium contact device

In order to see if choosing a different metal as a contact material will effect the photoresponse from the device, we prepared indium top contact devices for the measurements. An indium needle is drawn using a micro manipulator from a molten indium source. As indium is a soft metal and has a very low melting point of around 156^{O}C, such kind of device fabrication does not require usage of sophisticated metal evaporator. The drawn indium needle solidifies immediately as it leaves the hot indium source surface. We then place this needle on top of hot NbS_2 surface with very careful alignment. As the sample cools down, the indium solidifies making an electrical contact with the NbS_2. Optical image of the fabricated IC-1 device is shown in figure 3.16 (a).The resistance of this device is 196.46Ω.

As compared to TC devices, in IC devices Seebeck effect at zero applied bias is quite significantly diminished as can be see in figure 3.16(c). As the thickness of the indium needle is huge as compare to gold contacts in TC devices, this effectively block the laser beam. In result, the NbS_2/metal junction can not be heated by laser beam and Seebeck effect is diminished. Figure 3.16(g) shows the photocurrent dependence on the applied laser power. It can be seen that the photocurrent increases linearly, just like TC devices with gold contacts, as we increase the laser power.

3.2.3 Bottom contact devices

In bottom contact(BC) devices, contact resistance plays a major role in generation of photocurrent through the crystal. It diminishes the negative photoconductance which is observed in the middle of the crystal due to decrease in effective bias(V_{eff}) on crystal due to poor electrical contact. It is because of the potential drop in the device due to huge contact resistance R_C.

Our measurements on bottom contact devices prepared by transferring NbS_2

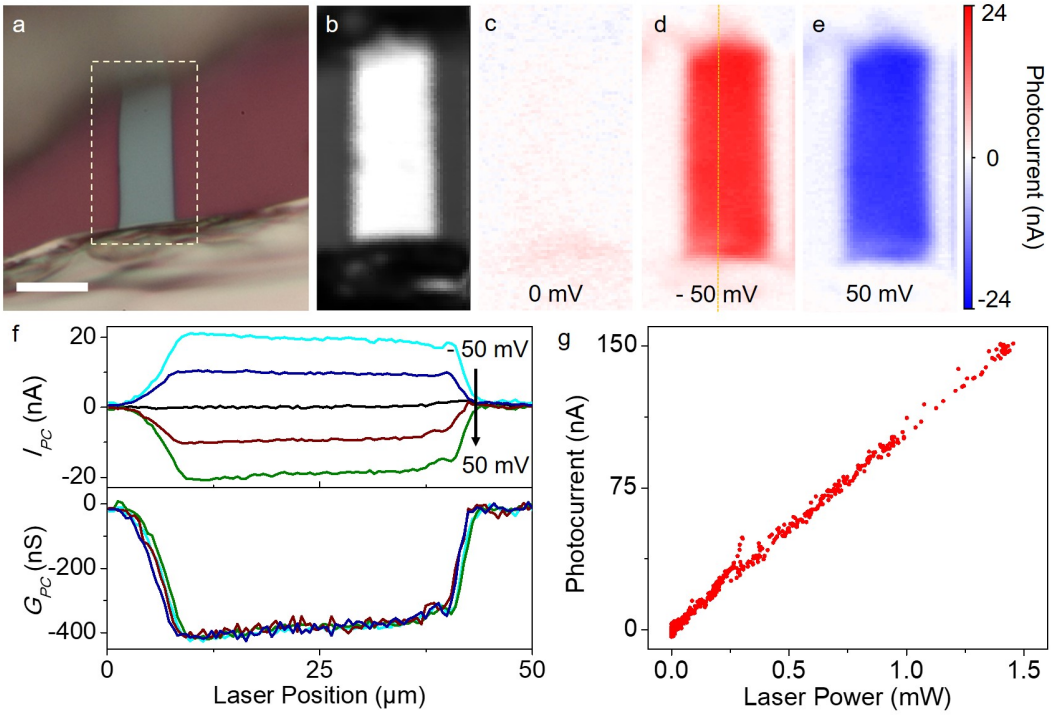

Figure 3.16: (a) Optical micrograph of prepared indium top contact device (IC-1). Dashed white region shows the area where SPCM is performed. Scale bar is 10μm. (b) Reflection map (c)(d) and (e) photocurrent maps at zero, -50mV and 50mV applied bias respectively. Dashed line in the (d) corresponds to line traces plotted in upper panel of (f) at several different biases. As can be seen the Seebeck effect is significantly diminished but the photoconductance remain invariant (lower panel (f)) for all applied biases through the crystal. (g) Photocurrent plotted against increasing laser power showing linear dependence. Reproduced from ref. [91]. Copyright American Physical Society 2018

crystal on top of pre-patterned thin gold electrodes shows photoresponse as described in previous paragraph. Optical image of the BC-1 device can be seen in 3.17(a). The thickness of the crystal is 100nm as measured by atomic force microscopy. The measured resistance of a BC-1 device is R = 600Ω in ambient conditions. First of all, we will discuss zero bias photoresponse. Unlike TC devices, BC-1 exhibit local photoresponse which is a order of a magnitude smaller than that of TC devices. 532nm laser with power P=32μW is used for the experiment. The reduction in photoresponse magnitude can be due to higher resistance of the BC-1 device. The calculated value of $\Delta T_C/P$ is 50mK/μW. Compared to TC devices, this value is higher and is expected because of poor thermal contact

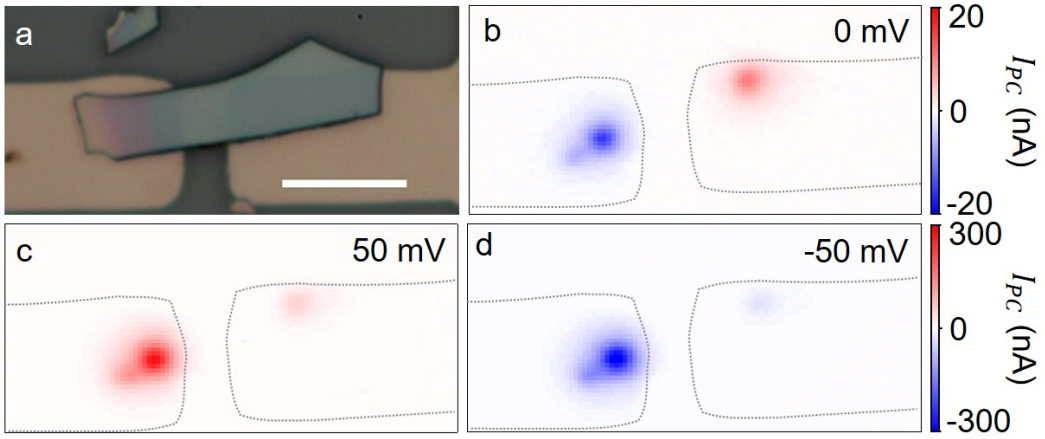

Figure 3.17: (a)Optical micrograph of a bottom contact device. scale bar is 10μm. (b) Photocurrent map under zero applied bias. The photoresponse is localized to a small region and is a magnitude smaller than TC device. (c) and (d) photocurrent maps at 50mv and -50mV applied biases respectively. Photoresponse changed only at the NbS_2/metal junction and no response is observed through middle of the crystal. Reproduced from ref. [91]. Copyright American Physical Society 2018

of the crystal to the gold electrodes which offers poor heat dissipation upon laser heating.

If we compare resistance of BC devices to the TC devices, a crystal used to prepare BC-1 should have resistance around 25Ω in ambient conditions. The difference between the measured resistance value and expected resistance(R_E) value can be attributed to larger contact resistance. The observed photoresponse under zero applied bias is localized to a small region and the magnitude of amplitude is smaller as compared to TC devices. Also the amplitude of photocurrent on bias and ground electrodes are different which is an indication of changing contact quality at both junctions. Under a finite applied bias, we observe change in only the photoresponse coming from the NbS_2/metal junction and no photoresponse is visible through the center of the crystal as can be seen in 3.17 (c) and (d). We can write effective bias on the crystal by the relation shown in equation 3.7.

$$V_{eff} = \left[\frac{V_B}{R_E + R_C}\right] R_E \tag{3.7}$$

For the case of BC-1, the V_{eff} is as low as 4% of applied bias V_B. So the photocurrent that we measure from the centre of the crystal is less than a nanoampere in a device like BC-1.

3.2.4 Photoconductance dependence on Laser Power

We tested effect of laser power on the photoconductance of a top contact device TC-2. Figure 3.18 (b) and (c) shows photocurrent maps at 50mV and -50mV applied bias respectively. At several different laser power, the negative photoconductance shows linear dependence. When we plot negative photoconductance per unit laser power, we find that the spread of values is negligibly small and has a mean value of -0.068 S/W. Also the calculated temperature rise per unit laser power in TC-2 is 35mK/μW which is similar to the value we found for TC-1.

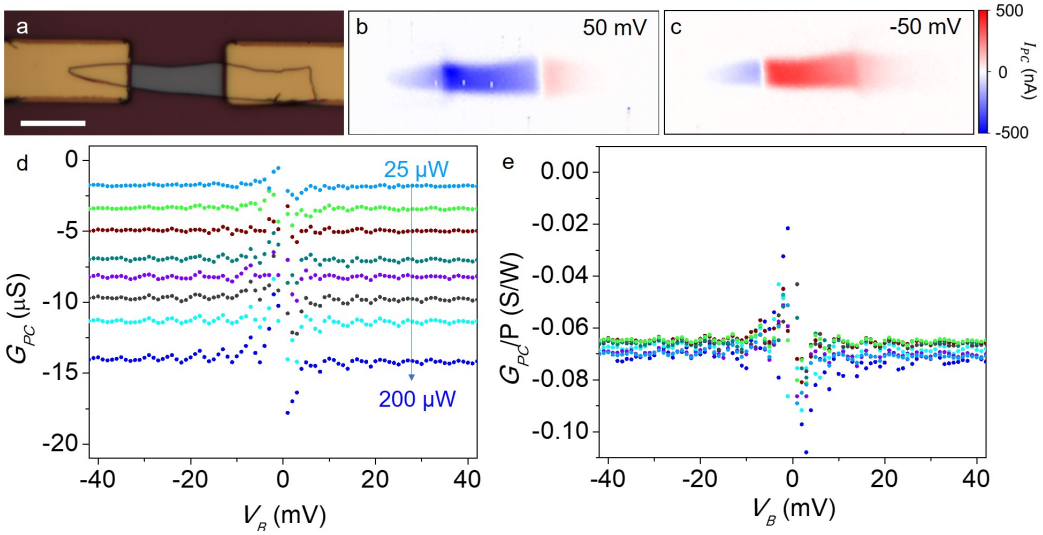

Figure 3.18: (a) Optical micrograph of TC-2 device. (b) and (c) are photocurrent maps of same device under 50mV and -50mV applied biases respectively. (d) change in photoconductance as a function of applied bias under different laser illumination powers. (e) Corresponding photoconductance per unit laser power at several applied bias. Reproduced from ref. [91]. Copyright American Physical Society 2018

3.2.5 Low pressure measurements and BC device with low contact resistance

In order to check if presence of oxygen has any effect on the generated photoresponse, we performed low pressure SPCM on a top contact device named TC-3. Reflection map of the device can be seen in figure 3.19(a). Photocurrent maps obtained under -50mV applied bias in ambient (b) and in vacuum (c) are plotted. We observe no difference in the intensity of generated photocurrent. Line traces through the center of the crystal from the photocurrent maps to obtain photoconductance are plotted in figure 3.19(d). It also show no change in photoconductance as well. There is a slight shift which is due to centering if the line trace through photocurrent map.

We also performed low pressure measurements on a BC device with very low resistance. Photocurrent maps under ambient and vacuum condition show no difference as well, as can been seen in figure 3.20 (b) and (c). We would like to mention that BC-2 has very low resistance with minimal contact resistance. Due to this reason we are able to see photocurrent being generated from all over the crystal which is consistent with our claim mentioned earlier. BC-2 device was prepared with a thinner and larger crystal and have a larger contact area with the electrodes. This lead to significant photocurrent generation at finite applied bias through out the crystal. The resistance of the BC-2 device is 36Ω. IV curves under ambient and low pressure condition show no variation as well and can been in figure 3.20(d).

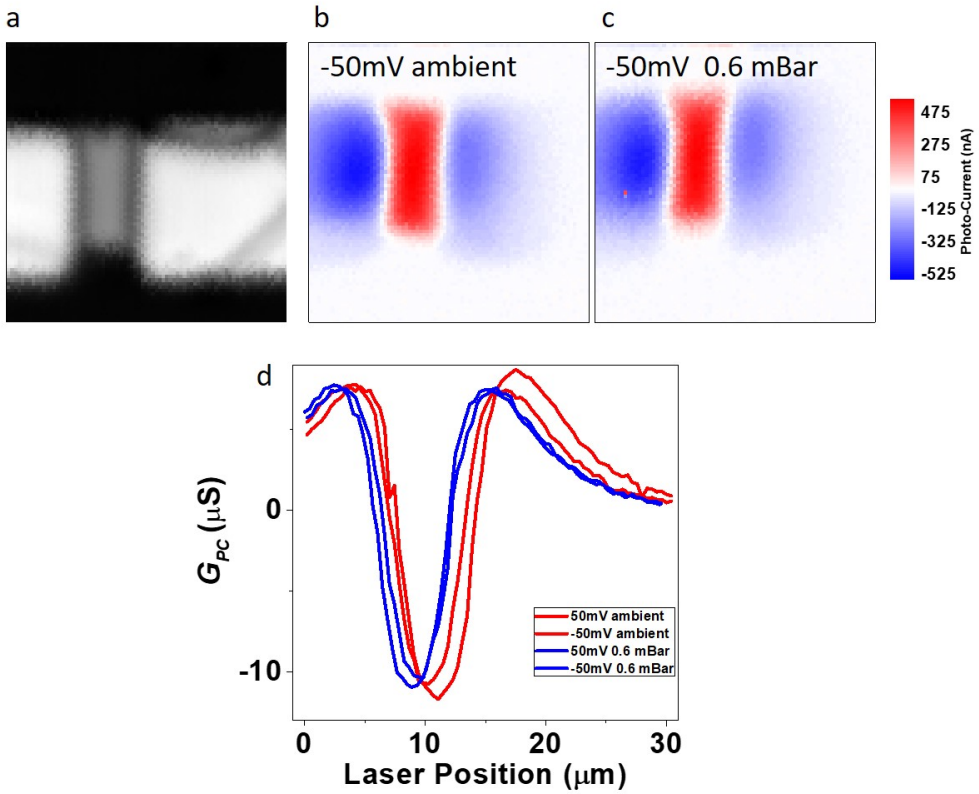

Figure 3.19: (a) Typical reflection map obtained during SPCM.(b) and (c) photocurrent maps under -50mV applied bias both under ambient and low pressure respectively. No change in photoresponse observed under low pressure.(d) Line trace through the middle of the crystal taken from photocurrent maps. No difference observed except slight shifting which is because of centering of the line trace.

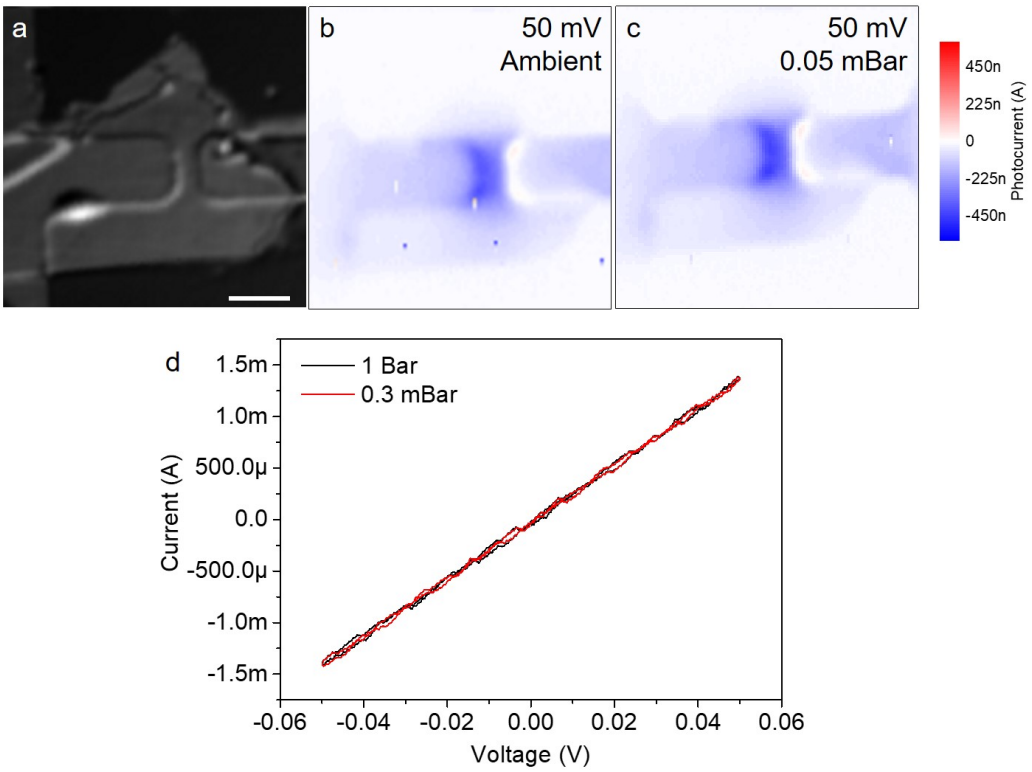

Figure 3.20: (a) Reflection map of BC-2 obtained during SPCM. Scale bar is 10μm. Photocurrent maps obtained under 50mV applied bias (b) in ambient and (c) in low pressure. (d) IV characteristic curves taken at ambient and 0.3mBar. There is no resistance change in the device for both cases. Reproduced from ref. [91]. Copyright American Physical Society 2018

3.2.6 Effect of polarization on photoresponse

All the previous measurements performed in this study involved unpolarized laser light. To check the effect of polarization, we performed SPCM with linearly polarized and non-polarized light. For the same laser power 85μW, we used unpolarized and linearly polarized laser beam to perform SPCM on EBL patterned TC-4 as can be seen in figure3.21. We observed no difference in the photoresponse for linear polarization of light on the sample. Also measurements performed under some finite applied bias show no change in photoresponse under different light polarizations.

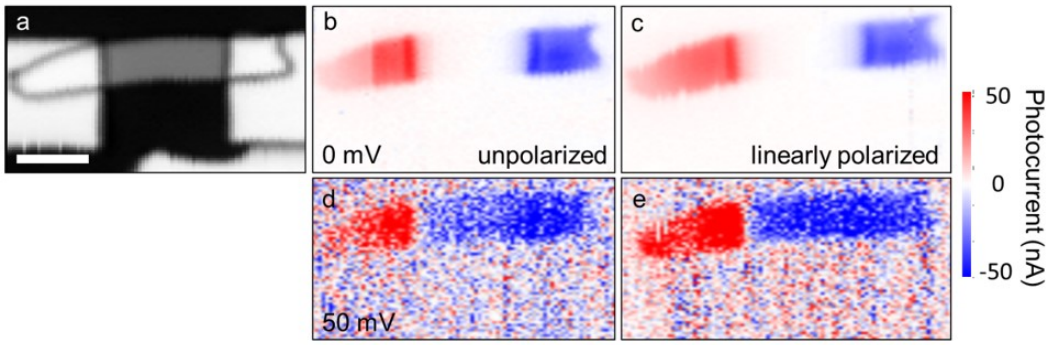

Figure 3.21: (a) Reflection map of TC-4 obtained during SPCM. Zero bias photoresponse using (a) unpolarized and (b) linearly polarized laser beam. Photoresponse under 50mV applied bias for (d) unpolarized and (e) linearly polarized laser beam. Both zero and 50mV bias measurement show no effect of laser light polarization. Scale bar is 5μm. Reproduced from ref. [91]. Copyright American Physical Society 2018

Chapter 4

Thermal conductivity measurements in 2D Materials, Methods and Limitations

The measurement of spatial transfer of heat in a material is termed as thermal conductivity[97]. It is important to study this property of material due to its countless applications in our daily life. Electric irons, cooking stoves, computer CPU, car engines and solar panels are few examples where we utilize thermal properties of materials to construct such sophisticated daily life equipments. Mathematically, we can write thermal conductivity in the form of equation 4.1.

$$Q = \kappa.\Delta T \qquad \text{and} \qquad ZT = \frac{S\sigma^2}{\kappa}T \tag{4.1}$$

Here Q is heat flux through material, κ is thermal conductivity, ΔT is change in temperature, S is Seebeck coefficient, σ is electrical conductivity and T is the temperature change of the material. First equation is termed as Fourier's Law and used to determine heat conduction in materials[98]. Second equation is related to maximum efficiency of a material and termed as thermo-electric figure of merit[99].

2D materials offers unique thermal and thermoelectric properties. Thermal properties of these materials have been extensively studied using several different methodologies[100]. Graphene, which is a wonder material in 2D world, exhibits extraordinary material properties. It also includes exceptionally high thermal conductivity value of the order of 5300W/mK[49]. 2D materials with extremely low thermal conductivity value are also part of literature such as SnSe(Thermal conductivity as low as 0.23W/mK)[99]. This means 2D materials can be used for thermal and thermoelectric applications over a very wide range. For heat dissipation applications, 2D materials with high thermal conductivity value can be used. Similarly, for thermoelectric generation applications, materials with lower thermal conductivity value can be utilized.

Several thermal conductivity measurements methods have been designed to calculate thermal conductivity of 2D materials. The most studied materials in this regard are graphene and molybdenum disulfide (MoS_2) due to their abundance in nature and availability. Let us discuss different types of thermal conductivity measurements methods one by one. These methods can be categorized in two different domains.

- Steady state techniques
- Transient techniques

4.1 Steady State Techniques

When temperature of a system does not change with time, the thermal conductivity measurements performed under such condition will fall in the category of steady state technique[101]. General strategy to perform thermal conductivity measurements involve determining a temperature dependent quantity which we measure by changing the temperature. Following that we need to set a relation between that quantity and thermal conductivity. Based on this strategy, let us discuss some of these methods one by one.

4.1.1 Raman Thermometery

Raman spectroscopy is a very powerful tool for the material characterization as different raman active phonon modes provide very useful information about the material and considered as the finger print of the material under observation[102]. Temperature dependent change in Raman modes can be utilized to calculate thermal conductivity of several 2D materials[102]. A focused laser beam is utilized in this technique with two fold purpose,

1. Heating the sample suspended over the hole or trench
2. To obtain temperature dependent Raman peaks of materials

Suspension of material is very important for Raman thermometery because of two reasons

1. To get rid of any heat sink under the focused laser spot in the form of substrate. Heat can flow easily from material to substrate and thermal conductivity measurement will incorporate thermal conductivity of the substrate as well.
2. The reflected light from the substrate will add extra heating to the desired material which will change the temperature of the material.

A Gaussian laser beam is chosen to obtain radial distribution of temperature rise over the suspended part of the crystal. The generated Raman signal in this case will show some temperature dependent variation which will be ultimately utilized to calculate thermal conductivity of the suspended material using the relation given in equation 4.2[103].

$$\kappa = \chi \left(\frac{L}{2hW}\right) \left(\frac{\delta\omega}{\delta P}\right)^{-1} \tag{4.2}$$

Here χ is the slope obtained from the temperature dependent peak shift($\delta\omega$) vs power(P) graph. If the material is transferred on top of the trench, then L is the half length of suspended material. Thickness and width of the crystal is denoted by h and W respectively. δP is the change in the heating laser power. Among these parameters, L, W and h are known. χ, $\delta\omega$ and δP can be obtained from measurements. Using equation 4.2, we can easily extract the value of thermal conductivity(κ).

Many researchers have reported thermal conductivity values of monolayer graphene and MoS_2 based on Raman thermometery methods. If we look into literature, we will find too much variation among these findings.Table 4.1 shows the comparison of thermal conductivity measurements using raman thermometery method. As said earlier, different studies reported different values of the measured thermal conductivity for the same material with the same number of atomic layers.

Table 4.1: Comparison of thermal conductivities of different 2D materials measured using raman thermometery method. Reproduced from ref. [104]. Copyright John Wiley & Sons, Ltd. 2017

Material	Substrate	Preparation	Absorption coefficient (%)	Laser wavelength (nm)	Hole size (μm)	Laser spot size (μm)	χ_T (cm^{-1} K^{-1})	K (Wm^{-1} K^{-1})
1L-MoS_2	Si_3N_4	Exfoliation	9	488	1.2	0.34	E^1_{2g}: 0.011 A_{1g}: 0.013	34.5
1L-MoS_2	Au	Exfoliation	5.8	532	4.0	0.46 0.62	A_{1g}: 0.020	84
2L-MoS_2	Au	Exfoliation	12.1	532	3.0	0.46 0.62	A_{1g}: 0.014	77
FL-MoS_2	Cu	Vapor phase growth	—	532	—	1–1.5	E^1_{2g}: 0.013 A_{1g}: 0.012	52
1L-WS_2	SiO_2	CVD	4	532	6.0	0.5	E^1_{2g}: 0.012 A_{1g}: 0.014	32
2L-WS_2	SiO_2	CVD	8	532	6.0	0.5	E^1_{2g}: 0.013 A_{1g}: 0.011	53
1L-$MoSe_2$	SiO_2	Exfoliation	5.6	633	2.5	0.46 0.62	A_{1g}: 0.014	59
2L-$MoSe_2$	SiO_2	Exfoliation	9.4	633	3.0	0.46 0.62	A_{1g}: 0.009	42
SLG	Au	CVD	5.7	488	7.5	0.36	G: 0.015	1800
SLG	SiO_2	Exfoliation	13	488	3	0.5–1	G: 0.016	4840–5300
SLG	Au	CVD	3.3	532	3.8	0.38 0.48	—	2500

OTR, optothermal Raman; SLG, single-layer graphene; CVD, chemical vapor deposited.

The main advantage of raman thermometery is the sample preparation. It is non-destructive methods and all measurements are performed in non-contact

mode. Compared to other methods, device fabrication is easier for thermal conductivity measurements.

4.1.2 Micro-Bridge Thermometery

Micro-bridge thermometery is a well established method to calculate thermal conductivity of material in both their bulk form and 2D form[105]. The measurement setup consist of an heating element and a thermal sensing element[106]. This method utilize Fourier's law in two probe measurement configuration in order to measure thermal conductivity of the materials and can be written as the equation

$$Q = \kappa.\Delta T \tag{4.3}$$

In four probe configuration, the provision of heat to each probe is done one by one. This will yield four set of equations with nine unknown parameters. Out of these nine parameters, six are dependent and three are independent which makes this method of calculating thermal conductivity of a system very complicated. Figure 4.1 shows exemplary device fabricated for microbridge thermometery[107]. As can be seen from the figure, the degree of complexity to measure thermal conductivity using this method is very high and not feasible for all materials.

One of the major disadvantage of this technique is the complicated device fabrication. It involves several lithography and etching cycles which will introduce contamination to desired material inevitably. Also not all material can endure such fabrication process except few strong materials like graphene, HBN and MoS_2 in their 2D counter part.

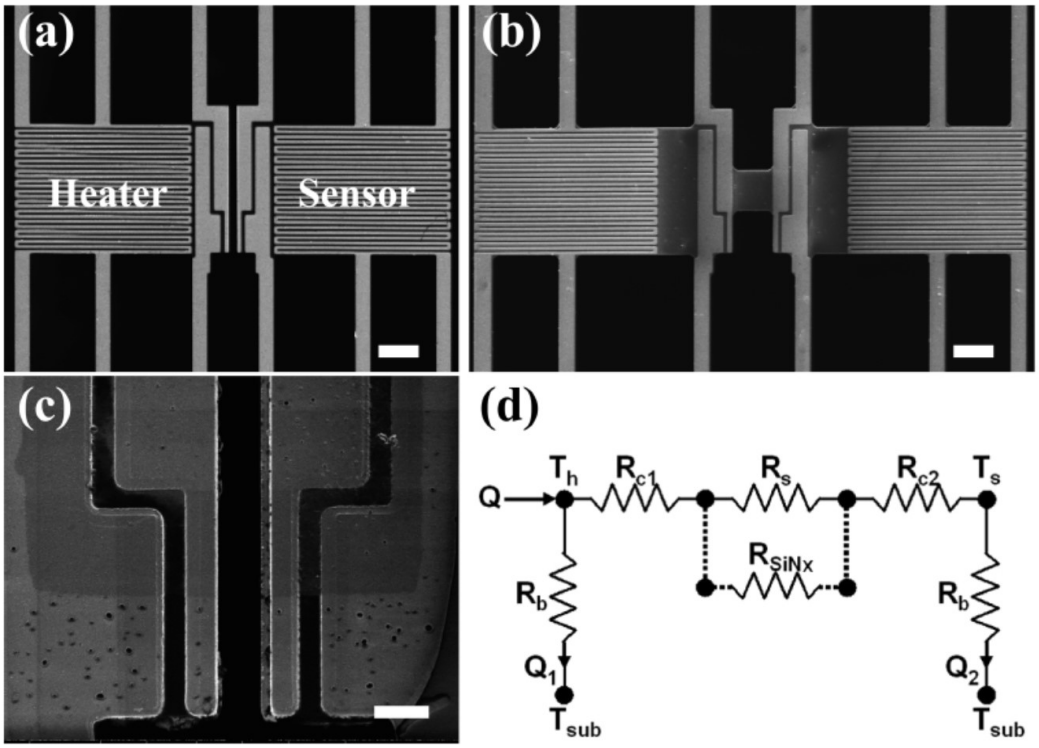

Figure 4.1: (a) and (b) show SEM image of microbridge structure for supported and suspended graphene flake respectively. scale bar 5μm (c) Close up SEM image of the device with graphene suspended over the contact pads. Scale bar 1μm (d) Schematic circuit diagram of the fabricated device. Reproduced from ref. [108]. Copyright American Chemical Society 2011.

4.2 Transient Techniques

When the temperature of sample changes with time, the thermal conductivity measurement performed under such condition will fall in the category of transient techniques. Time domain thermal reflectance and 3ω methods can be considered as transient techniques of thermal conductivity measurements.

4.2.1 Time Domain Thermo-Reflectance Method(TDTR)

Thermal conductivity of materials exhibiting temperature dependent reflectance change can be calculated using TDTR method. When laser light falls on a material, it will reflect and absorb light simultaneously. Temperature can change the transmission and reflection property of a material. So we can utilize one of these properties to calculate thermal conductivity of the material[109]. A thin film acting as transducer is usually coated on the sample. The surface of transducer should exhibit temperature dependent reflectance change under minute temperature rise. In 1970s and 1980s, first TDTR experiments were carried out using continuous wave lasers. Paddcock and Eesley were among the first scientist to demonstrate measurement of thermal diffusivity of metal films by utilizing picosecond transient thermoreflectance method[110]. In the last twenty year, this technique has evolved and improved significantly and is capable of measuring anisotropic thermal conductivity[111]. In TDTR method, pump and probe pulses are sent to the sample surface where pump beam is used to induce heat flux and the probe beam is used to detect any temperature change through the change in reflectance of the sample. Thermoreflectance response is measured as a function of time delay between the pump and probe pulses.

A typical TDTR set-up uses mode-locked Ti:sapphire laser oscillator to act as a light source. Using this laser oscillator, 150fs laser pulses can be generated at a repetition rate of 80-MHz. This is the most commonly used laser in this type of experiment due to its ultra fast nature. Some other type of lasers can also be used which include dye laser, Yb:doped fiber laser. In order to prevent laser beam being reflect back to the oscillator, brodband Faraday optical isolator is used in front of the laser source. To adjust the laser power, a half-wave plate is placed before the isolator. Polarizor beam splitter (PBS) is used to split the laser beam into pump and probe beams. The pump beam and the probe beam are cross polarized with respect to each other. Power ratio between the pump and probe beams is adjusted by placing another half wave plate before the PBS. Electro-opto modulator(EOM) modulate the pump beam at a frequency ranging from 0.2-20MHz before it reaches the sample through an objective. A mechanical

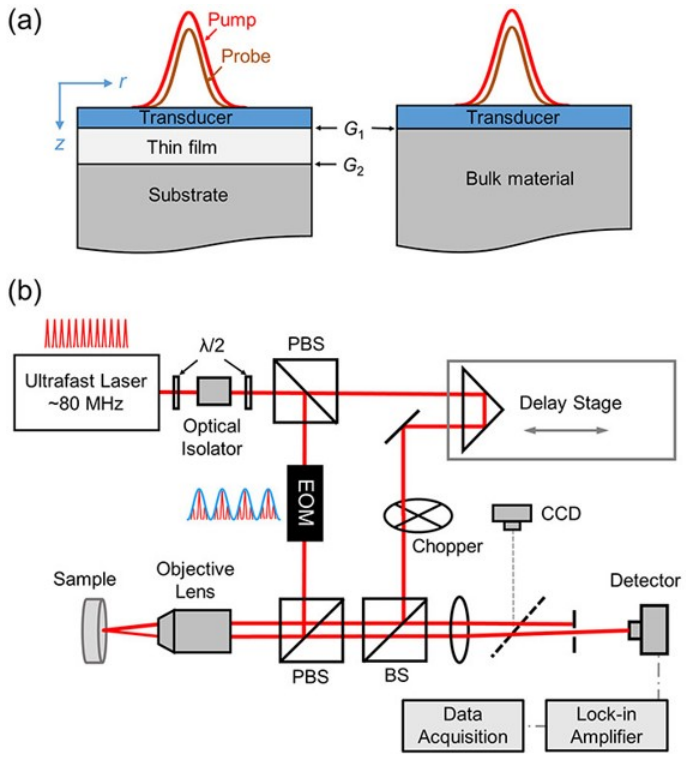

Figure 4.2: (a) Schematic of typical samples used for TDTR technique. Both thin film and bulk sample configuration is shown. (b) Drawing of typical setup used for TDTR setup. Used abbreviation are PBS(Polarizing beam splitter), BS(Beam splitter), EOM(Electro-optic modulator), $\lambda/2$(Half wave plate). Reproduced from ref. [110]. Copyright AIP Publishing 2018.

delay stage is used to delay probe beam with respect to pump beam before it reaches the sample through same objective. A fast response photo diode detector is used to collect the reflected probe beam which later on converts the optical signal to electrical signal. This signal is collected by radio frequency lock in amplifier which filters the strong background noise. Finally the acquired data is analyzed to obtain the thermal conductivity values for the selected material.

Major disadvantage of TDTR technique is its inability to measure samples below 20nm thickness[112]. It makes this method not applicable to 2D materials. Also the data analysis is very complicated due to time dependent heat transfer equation. The addition of transducer adds another degree of complexity to the heat equation and solution is obtained by making many approximations.

4.2.2 3ω Method

This method requires placement of a thin metal line across the material by using lithographic technique followed by metal evaporation[113]. This deposited metal line can be used both as a heating source and a thermometer. Heat is supplied using an AC current via joule heating and hence the temperature rise on the sample will be frequency dependent. A relation between the thermal conductivity and applied frequency is derived in such a way that system does not require to achieve a steady state condition and yet thermal conductivity can be measured. The frequency of applied AC current is set to 2ω resulting in temperature oscillation in metal line at a frequency 2ω. Ultimately, the change in the resistance of the metal line can be detected at third harmonic 3ω. "The applicability of the 3ω technique is very limited on two-dimensional due to the electrically insulated sample requirement of the method. The thermal boundary resistance across various interfaces must be measured for an accurate extraction of the thermal conductivity, which limits the usability of the method on two-dimensional materials[114]."

4.3 Bolometric effect based Method

Recently we demonstrated thermal conductivity measurement of nano sheets via bolometric effect[115]. The laser induced heating can cause change of resistance of the material locally under applied bias. This temperature dependent resistance change of the material can be used to calculate thermal conductivity of the material. The details of this method will be discussed in detail in chapter 5.

Chapter 5

Thermal Conductivity Measurement via Bolometric Effect

Temperature dependent resistance change can be observed in all type of materials (metallic or semiconducting) in a wide range of temperature. Normally, metallic materials exhibit increase in resistance when temperature of the sample is increased. Contrary to that, semiconducting material show resistance depreciation upon heating. In our proposed method, first of all, resistance of the material is determined in absence of local heat source (in our case it is focused laser beam). Under focused laser beam, the temperature of the sample will increase locally causing change in resistance of the material upon reaching a steady state. Using thermal conductivity as a fitting parameter, we can model the thermal distribution under the focused laser spot precisely. Consequently, the resistance change(δR) of the sample is calculated to match the experimentally obtained δR value. And hence the thermal conductivity of the specimen can be calculated precisely.

Just like Raman thermometry, a focused laser beam can be used to locally heat many 2D material. When a 2D material is placed on top of a substrate,

considerable amount of heat dissipates to the substrate via thermal contact. In that scenario, measurement of thermal conductivity becomes very challenging. Thus it is important to isolate the selected material from the substrate in such a way that all applied heat can be used to solely elevate the temperature of 2D material locally. This can be achieved by suspending a 2D material on top of a hole or trench. A similar methodology of sample preparation is adapted in Raman thermometery as well which we discussed briefly in previous chapter.

5.1 Bolometric Effect

As discussed briefly in chapter 2, the calibrated change in electrical resistance of a material caused by the uniform heating induced by photon absorption is called bolometric effect[116]. The measured electrical resistance change can be used as a thermometer. All materials exhibit temperature dependent change in their state. As we pass heat from them, some of their properties will change. Electrical resistivity is one of the material's property that shows temperature dependent variation. For metals, this change is resistivity can be written in the form of equation 5.1[117].

$$\rho(T) = \rho_0(1 + \beta(T - T_0)) \tag{5.1}$$

Here T_0 is room temperature(or reference temperature), β is the temperature coefficient of resistance and ρ_0 is the resistivity of the material at T_0. For semiconductors, we can write a similar relation given by equation 5.2.

$$\rho(T) = \rho_0 e^{E_A/k_B T} \tag{5.2}$$

Here E_A represents activation energy, k_B is the Boltzmann constant. we can use resistance vs temperature (RT) measurements to calculate E_A experimentally.

5.2 Isotropic 2D Materials, Analytical Solution of the heat Equation

Schematic of device geometry can be seen in figure 5.1(a). We need to solve heat equation for the supported part of the crystal as well as suspended part of the crystal over the hole illuminated by a Gaussian laser spot which act as a heat source. For the suspended part, heat equation can be written as the equation 5.3.

$$\kappa \frac{1}{r}\left[r\frac{d}{dr}T_1(r)\right] + q(r) = 0 \qquad r < a \tag{5.3}$$

where

$$q(r) = \frac{I\alpha}{t} exp[\frac{-r^2}{r_0^2}] \tag{5.4}$$

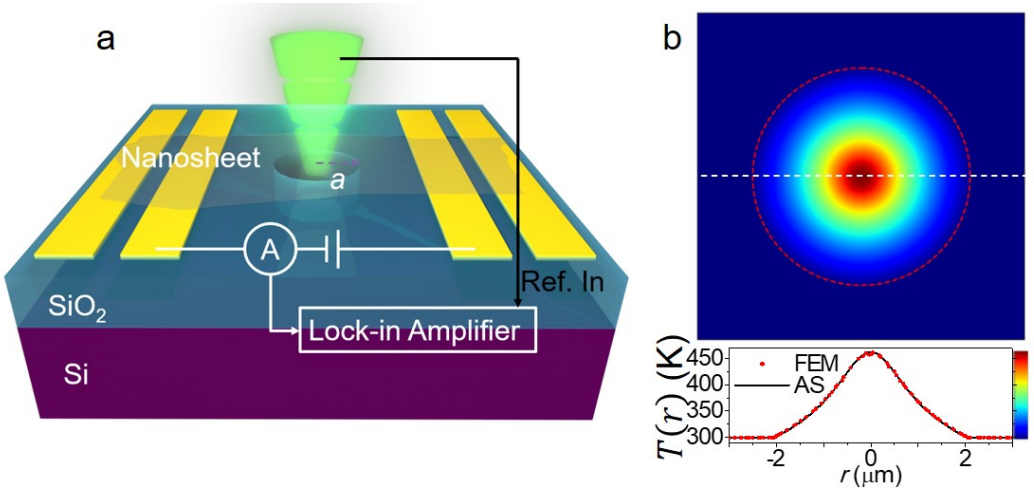

Figure 5.1: (a) schematic of the measurement system along with fabricated device is drawn. A thin nanosheet is suspended over the hole with a radius a. (b) Temperature profile of a 2D material suspended over the hole under certain laser illumination. Dashed red circular line mark the boundary of the hole. Temperature rise is maximum at the center of the hole while equiliberate with ambient as we move far away from center. Lower panel show line trace through the center of the hole showing both analytical and FEM solution. Reproduced from ref. [117] .Copyright Springer Nature 2020.

κ is the thermal conductivity of the suspended material, I is laser power per unit area, α is absorbance of the material , t is the thickness of the crystal, r_0 is radius of the Gaussian beam spot and $T_1(r)$ is temperature distribution function for r<a. For the supported part of the crystal, the heat equation can be written as

$$\kappa' \frac{1}{r}\left[r\frac{d}{dr}T_2(r)\right] - \frac{G}{t}[T_2(r) - T_0] = 0 \qquad r \geqslant a \tag{5.5}$$

κ' is the thermal conductivity of the supported part of the crystal,T_2(r) is temperature distribution function for r$\geqslant$a, T_0 is the room temperature and G is the thermal transmittance. Volumetric Gaussian beam heating source is used in the equations(from paper reference). Newtonian cooling term is ignored in our equation for the sake of simplicity and also heat loss to air will be very negligible which makes it a good assumption to obtain an accurate result. General solutions of above equations can be written by equations 5.6 and 5.7

$$T_1(r) = c_1 + c_2 ln(\frac{r}{r_0}) + \frac{\alpha I r_0^2}{4\kappa t} E_i(\frac{-r^2}{r_0^2}) \tag{5.6}$$

$$T_2(\gamma) = c_3 I_0(\gamma) + c_4 K_0(\gamma) + T_0 \tag{5.7}$$

Here, E_i(x) is the exponential integral, I_0 (first order) and K_0(second order) denote the zero order Bassel functions with $\gamma = r\sqrt{\frac{G}{\kappa' t}}$. In order to calculate c_n we apply appropriate boundry conditions which are given by equation

$$T_2(\gamma \to \infty) = T_0 \tag{5.8}$$

$$\left.\frac{T_1(r)}{dr}\right|_{r\to 0} = 0 \tag{5.9}$$

$$T_1(a) = T_2(\gamma)|_{r=a} \tag{5.10}$$

$$\kappa \frac{T_1(r)}{dr}\bigg|_{r=a} = \kappa' \frac{T_2(\gamma)}{dr}\bigg|_{r=a} \tag{5.11}$$

The first boundary condition given by equations 5.8 suggest that at very far away from the center, $T_2(r)$ must possess a finite value and should equiliberate with ambient. Second boundary condition imply that the temperature rise under the focused laser spot will have a definite value and position derivative will yield a zero value. Boundary conditions 5.10 and 5.11 suggest the continuity of the heat exchange at the boundary of the supported and suspended part of the crystal. Under these boundary condition, the derived values of c_n are as follows

$$c_1 = T_0 + \frac{\alpha P K_0(\gamma_R)}{2\pi d t K_1(\gamma_R)} \sqrt{\frac{t}{G\kappa'}} \left[1 - exp[-\frac{d^2}{r_0^2}]\right] + \frac{\alpha P}{2\pi\kappa t} \left[2ln(d) - E_i\left(-\frac{d^2}{r_0^2}\right)\right]$$

$$c_2 = -\frac{\alpha r_0^2}{2\kappa}$$

$$c_3 = 0$$

$$c_4 = \frac{\alpha r_0^2}{2d K_1(\gamma_R)} \sqrt{\frac{t}{G\kappa'}} \left[1 - exp[-\frac{d^2}{r_0^2}]\right]$$

Using these coefficients in equation 5.6 and 5.7 , temperature distribution under the focused laser beam can be plotted as shown in figure 5.1 (b). Temperature rise is maximum at the center of the hole and decreases gradually as we move away from the center. Red dashed line mark the boundary of the hole. As it can be seen from the temperature distribution plot, the temperature of the crystal will equiliberate with ambient as we move very far away from the center as suggested

by the one of the boundary conditions. Once we obtain the temperature distribution T(r;κ) over suspended part of the crystal which has thermal conductivity dependence, we can calculate the corresponding resistivity change. Ultimately, we can calculate the resistance change caused by laser heating at the center of the hole. If this calculated change in resistance matches the value that we obtained experimentally, thermal conductivity(κ) value that was used as fitting parameter initially will be our real thermal conductivity of the material.

5.3 Thermal Conductivity Calculation Strategy via Bolometric Effect

Expected resistance change, δR_E, caused by photothermal heating can be calculated by using temperature distribution over the suspended part of the crystal. As mentioned earlier, we can write resistivity distribution for a semiconducting material by the relation $\rho(x,y) = \rho_0 exp(E_A/k_B T(x,y))$. For metallic samples, similar relation can be written as $\rho(x,y) = \rho_0 + \varrho[T(x,y) - T_0]$. These two relations can be used to calculate resistance of laser heated samples termed as R_H numerically. ρ_r can be written as a function of current density and internal electric field of the sample by the relation given in equation 5.12

$$\rho(r) = \frac{E(r)}{J(r)} \tag{5.12}$$

Using continuity equation for current density J(r) and Poisson's equation for internal electric field with in the sample, electrical resistance (R_H) of laser heated sample can be calculated. In our case, we are dealing with crystals of irregular geometries and current density is temperature dependent. For such complex geometries, commercially available finite element method (FEM) method (COMSOL Multiphysics) is used to calculate the R_H. Apart from this, analytical solution can still be used for samples with simpler geometries and lower resistances. In figure 5.2 (a), a typical SEM image of fabricated device can be seen. Figure

5.2 (b) shows results of FEM simulation results for thermal distribution, current density distribution, and electric potential distribution over the crystal when a focused Gaussian laser spot heats the crystal at the center of the hole. Expected resistance change(δR_E) under laser illumination can be written as the relation $\delta R_E = R_H - R$, where R is the dark resistance. Using κ as fitting parameter, the calculated expected resistance is matched with measured resistance change(δR_m). The specific κ value for which $\delta R_E = \delta R_m$ is the thermal conductivity of the material under experiment.

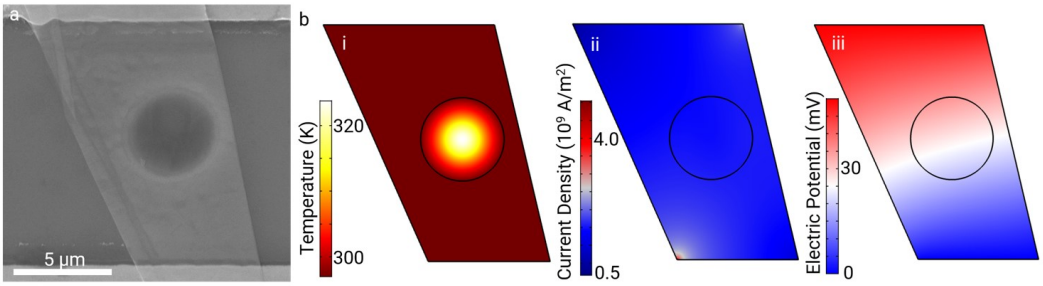

Figure 5.2: (a) SEM image of a typical device suspended over a hole with a diameter of 4μm. (b) (i)Temperature profile of the crystal between the electrodes with Gaussian laser spot focused at the center of hole. (ii) Corresponding current density and (iii) electric field potential are plotted based on local resistivity $\rho(x, y)$. Reproduced from ref. [115]. Copyright IOP Publishing Ltd. 2020.

5.4 Experimental Methods

5.4.1 Substrate Preparation and Bottom Contact Devices

Substrate preparation is very important in bolometry based thermal conductivity measurement method. Step by step substrate preparation is described below along with fabrication of bottom contact devices.

5.4.1.1 Optical Lithography

First of all, optical lithography is performed using negative tone photoresist. The use of negative photoresist ensures that we do not end up with side walls formation after the lift-off process. AZ-5214 is a positive tone photoresist which can also be used as negative tone resist by adding an extra image reversal step. The 280nm Si/SiO_2 substrate is cleaned thoroughly by acetone, IPA and DI water sequentially and blow dried with the nitrogen. The substrate is placed on the hotplate at 120^0C for 10 minutes to get rid of any moisture left on the surface. Photoresist is spin coated on the substrate at 4000rpm for 60 seconds. Spin coated substrate is placed on hotplate at 100^0C for one minute. This will activate the photoresist for the UV exposure. The substrate is placed on optical mask aligner under a mask on which patterns are drawn. The optical lithography is performed in hard contact mode to get rid of any edge beads formed during spin coating. UV exposure dose is set to 25 mJ/cm^2. After this, substrate is placed onto hotplate again for post exposure bake. This is done at 110^0C for 40 seconds. This is the most important step for image reversal. The sample is again put on mask aligner to do a flood exposure without any mask for image reversal finally. The dose in this step is set to 250 mJ/cm^2. After this sample is developed in a AZ-400K developer diluted in ratio of 1:4 in DI water for 45 seconds. Figure 5.3 shows fully developed pattern using optical lithography.

5.4.1.2 ICP Etching and metal deposition

Inductive couple plasma etching is a powerful technique to etch SiO_2 surface isotropically. We use in our process CH_3F and O_2 plasma for the etching purpose. Operating parameters of coil and plate are 13.56MHz and 396KHz at power 250W and 30W respectively. The etching is performed at room temperature for 12 minutes. This will result in etching of SiO_2 surface with 65nm depth. This will generate pits in the patterned area that we will fill with gold using thermal evaporator. We deposited 10nm chromium first which act as adhesion layer followed by 55nm gold deposition. In order to control deposition thickness precisely,

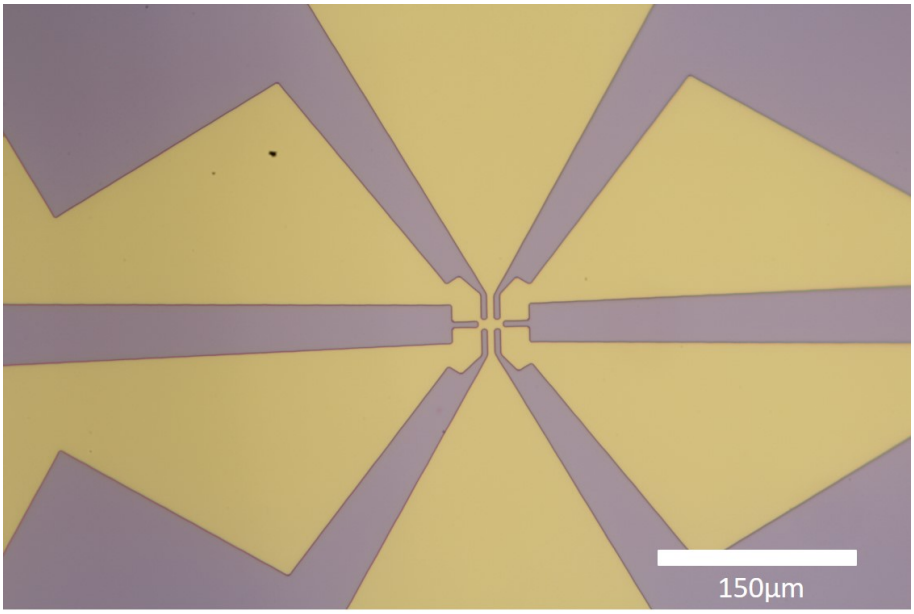

Figure 5.3: Optical micoscope image of patterns developed after optical lithography using negative tone photoresist.

the tooling factor of the machine should be very accurately calibrated. If done otherwise, we might end up having under or overfilling of the pits either of which is not desirable for our device fabrication. If the depth of these patterns does not match the metal filling, the transfer of crystals using visco-elastic PDMS stamping method can fail. The crystal will not get transfer on the desired electrodes due to height difference of metal electrode and substrate. So controlling this deposited thickness will make the device fabrication process more reliable and repeatable.

5.4.1.3 Hole Drilling using Focused Ion Beam Milling

For the sake of suspending crystals, holes need to be drilled between the electrodes. We used focused ion beam milling(FIB) for this purpose. FIB can drill very high aspect ratio holes in the substrate with desired size. Figure 5.5 shows scanning electron microscope images of the drilled hole using focused ion beam. The only disadvantage of using FIB is the slow process of drilling holes and the usage of FIB machine is costly.

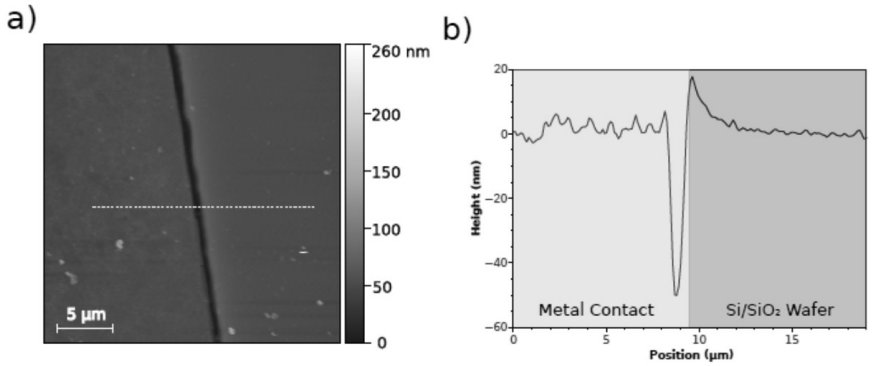

Figure 5.4: (a)AFM topography of the deposited metal electrodes into the pits created by ICP etching. (b) Corresponding height profile along the dashed white line. As can be seen, both metal and SiO_2 surfaces are on same level.

5.4.1.4 Crystal Transfer using Visco-elastic Stamp

Crystals are transferred on top of holes using all dry visco-elastic stamping method as have been mentioned in literature. Poludimethyl siloxane(PDMS) is used as visco-elastic stamp. For our experiments, we prepared our own cured PDMS in the lab. PDMS is prepared by using mixture of curing agent and elastomer base in a ratio 1:10. The mixture is vigorously shaken with a stirrer untill color of the mixture become whitish opaque due to incorporation of lots of bubbles. To get rid of bubbles, a vacuum desiccator is used. Once the bubbles are released, the solution is poured in glass petri dish after thorough cleaning. The glass petri dishes are left on hot plate set at 65C for 5 hours. This much time is enough to completely cure the base elastomer and resulting PDMS is stored in clean environment.

We perform mechanical exfoliation of bulk crystal on to blue NITTO tape(model# SPV224). The bulk crystals that we used are purchased from HQ-Graphene. Once we have desired thickness of crystals on the tape after few exfoliation, the mechanical exfoliation is performed on the prepared PDMS. The PDMS stamp is transferred onto a glass slide and mounted onto a home made crystal transfer setup attached to a micromanipulator. Thin crystals are identified under optical microscope. Target substrate is placed onto a stage with heating element. The crystal is aligned with the electrodes and centered with hole. The

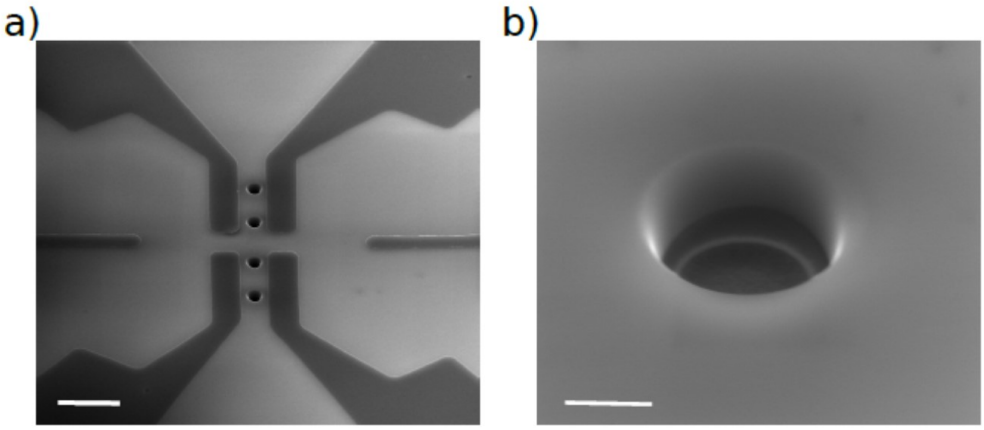

Figure 5.5: (a) SEM image of the drilled hole between the electrodes. Scale bas 10μm(b) Tilted angle close up of the drilled hole with high aspect ratio and desired shape and size. Scale bar 1μm. Reproduced from ref. [117] .Copyright Springer Nature 2020.

PDMS is brought in contact with substrate very slowly. Once the PDMS and desired crystal are in hard contact with the substrate, we wait for 3 minutes. After that we slowly raise the PDMS from the substrate. As adhesion of crystal is much stronger with the substrate and electrodes as compared to PDMS, the crystal will be transferred onto the target substrate as we slowly raise and detach PDMS from the substrate. Short schematic of fabrication process is shown in figure 5.6.

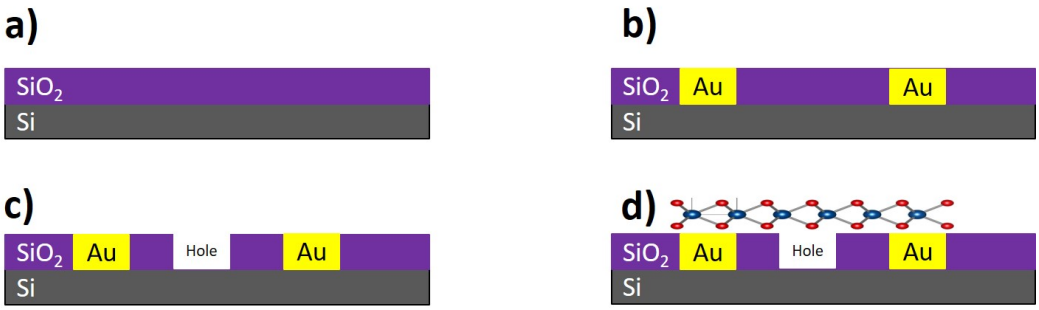

Figure 5.6: (a) 280nm thick SiO_2 wafer is chosen for fabrication (b) Gold metal evaporated into pits prepared after optical lithography and ICP etching. (c) Hole drilled using focused ion beam milling between electrodes.(d) 2D material transferred using all dry visco-elastic stamping method.

5.4.2 Top Contact Devices

In this work, we also prepared top contact devices for thermal conductivity measurements. Vanadium sesquioxide (V_2O_3) devices were specifically fabricated by top contacting indium metal.

5.4.2.1 Polycarbonate Assisted Crystal Transfer

First of all, V_2O_3 crystals are grown on sapphire substrate using salt assisted chemical vapor deposition. As these crystals need to be suspended on top of pre-patterned FIB drilled holes, we use polymer assisted transfer of CVD grown crystal from growth substrate to target substrate. Polycarbonate is chosen as a polymer to pick up the crystals from growth substrate. A solution of 6% by weight polycarbonate granules are mixed with 100ml of chloroform. Once the polycarbonate dissolves completely into chloroform, we spin coat this on growth substrate at 1200rpm. After coating, the substrate is heated at 180^0C for 6 minutes to make PC film adhere better to the CVD grown crystals. Spin coated sample is sonicated in water for one minute. This film is then removed from the growth substrate by wedging it on top of water surface. The floating film is picked up by fishing through Si/SiO_2 substrate. The picked up film is observed under microscope to target desired crystal for transfer. Once a crystal is chosen, a small portion of PC film containing that specific crystal is cut and placed onto the substrate with ICP drilled holes. The alignment of the crystal on top of hole is done by dragging the PC film using a micro-manipulator. Once the crystal is aligned, the PC film is melted by raising the stage temperature to 140^0C. This will make film adhere strongly to the substrate and to avoid any movement when we put substrate in the chloroform to dissolve PC film. Following this, sample is immersed in the chloroform to dissolve PC film leaving behind crystal on the hole.

5.4.2.2 Top Indium Contact

The methodology of putting indium contacts has already been discussed in section **3.2.2.1**. One of the fabricated device is shown in figure 5.7.

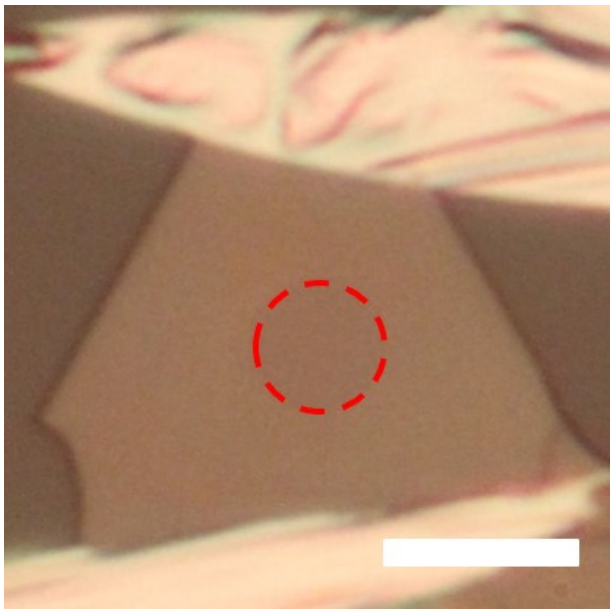

Figure 5.7: V_2O_3 crystal transferred on top of hole marked with red dashed circle. Two indium needles are drawn using micro-manipulator which act as electrodes. Scale bar is 5μm. Reproduced from ref. [115]. Copyright IOP Publishing Ltd. 2020.

5.4.3 IV Characteristic and Scanning Photocurrent Microscopy

Details of IV data acquisition along with scanning photocurrent microscopy has already been described in sections **3.1.3** and **3.1.4** respectively.

5.4.4 Full Width Half Maximum Value for Focused Laser Spot

In order to determine the profile of the laser beam, we utilized very common methods that is being used by many scientists. As we obtain the spatial reflection map of our whole device by raster scanning focused laser beam. In reflection map. gold contacts can be used to obtain laser profile by utilizing very old knife-edge method. Cross-section of the leaser beam spot can be determined through taking the position derivative of the intensity line trace taken along the gold contact edge. The FWHM value is finally obtained by doing Gaussian fit to the $\partial I/\partial x$ vs x plot.

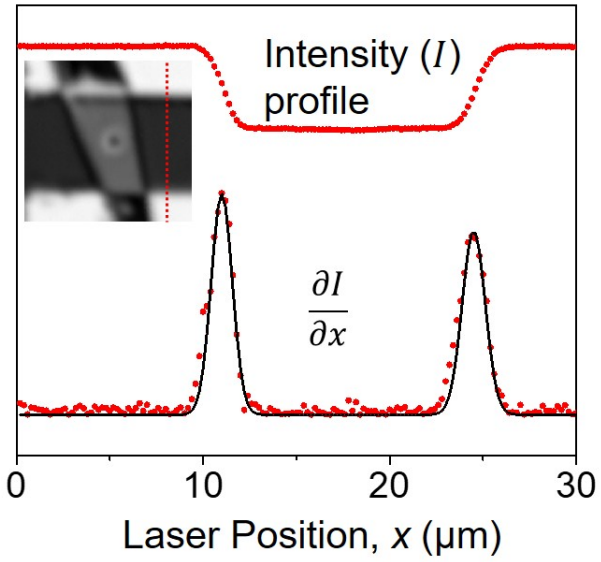

Figure 5.8: First position derivative of the intensity from reflection map yields two Gaussian peaks. Full width half maximum value for laser spot is obtained by the Gaussian fitting to the peaks. Inset shows reflection map of a fabricated device with red dashed line indicating the line trace path. Reproduced from ref. [115]. Copyright IOP Publishing Ltd. 2020.

5.4.5 Calculating Absorbance of Material

Calculating absorbance(α) of the nano-sheet is the most challenging part of our bolometry based thermal conductivity measurement method. Absorbance value of most of the 2D materials is unknown and the value changes with the number of layers and thickness. For the absorbance measurements, first of all, we do mechanical exfoliation of the material onto PDMS. The choice of PDMS is ideal for two reasons. First, it act as a transparent substrate which is very essential for absorbance measurement as we rely on both transmitted and reflected light intensities. Second, thin flakes identified for absorbance measurements can later be transferred onto gold electrode for thermal conductivity and thickness measurements. We measured laser beam intensity(I_0) through a CCD camera attached to a spectrometer. First we measure transmitted intensity of bare PDMS (T_0) in the vicinity of the specific crystal of which we need to measure absorbance. Then the transmitted intensity is recorded over the crystal which is termed as T. Next, corresponding reflected intensities are recorded for bare PDMS and the crystal which are termed as R_0 and R respectively. Once these parameters are recorded, equation 5.13 can be used to calculate absorbance of the crystal.

$$\alpha = \frac{I_0 - (T + R) - (T_{0+R_0})}{I_0} \tag{5.13}$$

Thickness dependent absorbance data obtained for 2H-TaS_2 is plotted in figure 5.10. To our knowledge, this is first report on absorbance of 2H-TaS_2 with thickness dependence.

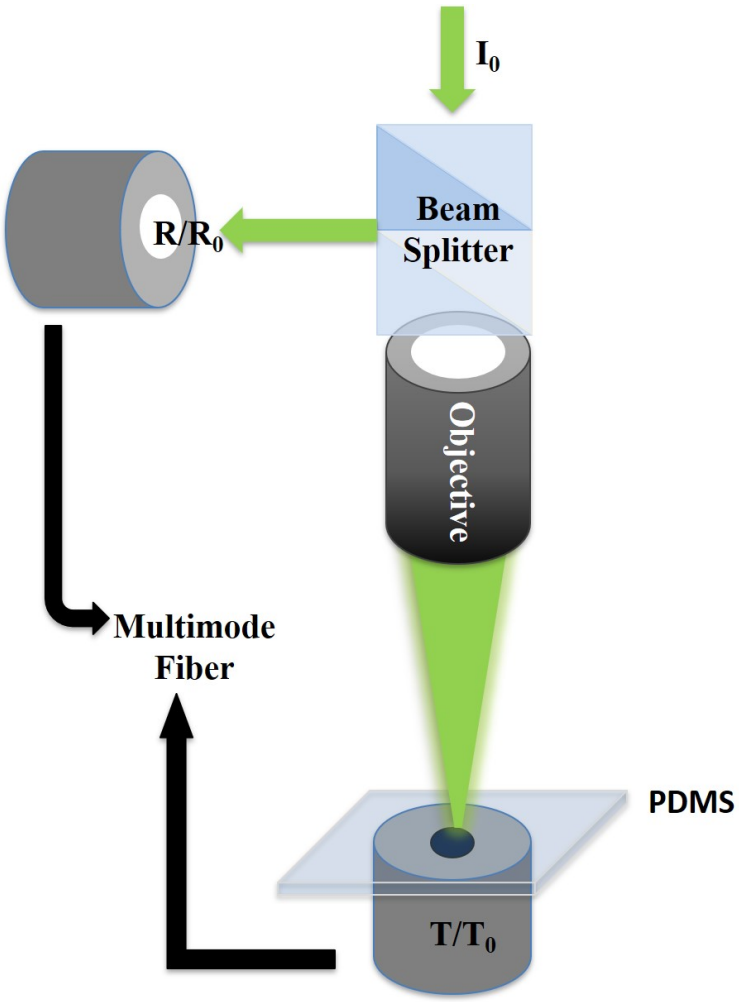

Figure 5.9: Absorbance measurement schematic is shown in the figure. Spectrometer is used to measure the intensities of both reflected and transmitted light.

5.5 Thermal Conductivity Measurement of Metallic Vanadium Sesquioxide(V_2O_3)

Vanadium sesquioxide(V_2O_3) belongs to vanadium oxide family which has a strongly correlated electron system. At room temperature, it can exist in paramagnetic metallic(PM) or paramagnetic insulator(PI) phase which depends on the applied stress on the material[118]. A structural phase transition is observed below 190K from paramagnetic insulator(PI) to antiferromagnetic insulator(AFI) for free standing crystals. This phase transition temperature termed as critical

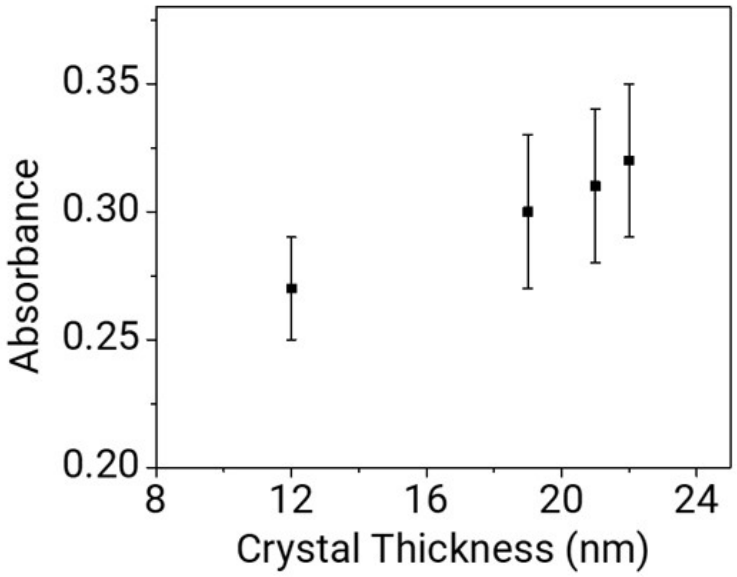

Figure 5.10: Absorbance measurement schematic is shown in the figure. Spectrometer is used to measure the intensities of both reflected and transmitted light. Reproduced from ref. [115]. Copyright IOP Publishing Ltd. 2020.

temperature(T_c) highly depends on the external conditions like stress and doping. A phase diagram indicating all possible structural phases of V_2O_3 under compressive and tensile stress is shown in figure 5.11.

In previous report, researcher has manipulated stress in V_2O_3 by choosing appropriate dopant. If we use titanium as a dopant, it will have similar effect on the crystal as if applying compressive stress. Contrary to this, chromium doping will result a net tensile stress on the crystal. Apart from these, temperature plays a critical role in inducing structural phase transition. As can be seen in the phase diagram, depending on which compressive stress we are in, below 188K V_2O_3 exhibits PI to AFI or PM to AFI or PI to PM to AFI phase transitions.

In recent study, we have demonstrated salt assisted chemical vapor deposition of V_2O_3 single crystalline nanoplates[119]. According to our observations, the as grown V_2O_3 nanoplates are under stress due to lattice mismatch between the growth substrate. We used sapphire as growth substrate in our experiments. As there is epitaxial growth relation between the synthesized V_2O_3 nanoplates

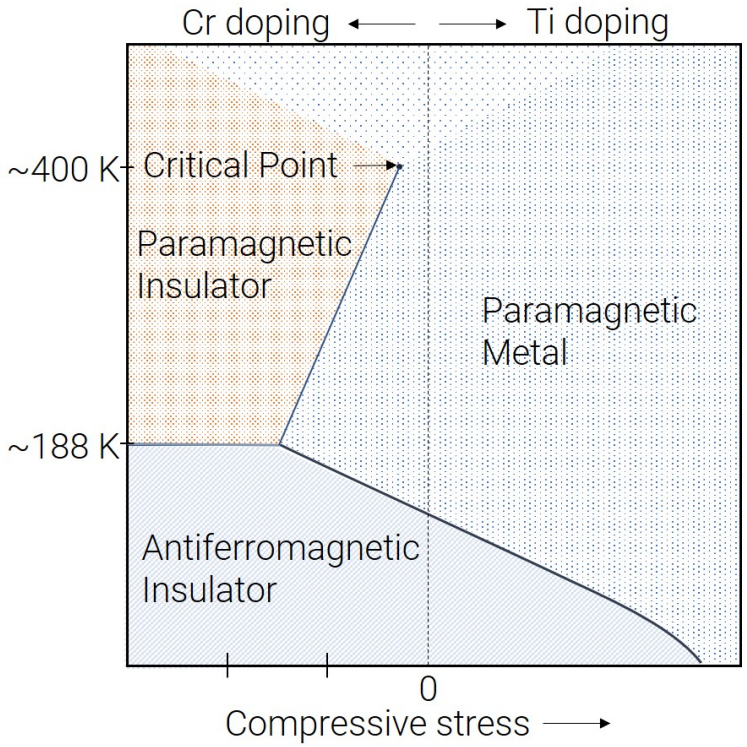

Figure 5.11: The phase diagram of V2O3 based on reference. The paramagnetic metal (PM) and insulator (PI) phases have corundum structure, while the antiferromagnetic insulator phase (AFI) has a monoclinic structure. Reproduced from ref. [119]. Copyright American Physical Society 2019.

and sapphire substrate, it introduce intrinsic stress onto the grown material. The phase of as grown crystals is always PI at room temperature. Once we release these crystal from sapphire substrate by transferring them onto any other arbitrary substrate, the stress on the crystals is released and we observe PI to PM phase transition(see figure 5.12). Upon cooling it enters the AFI phase of the crystals and upon heating it enters a cross over regime beyond a critical point as pointed on the phase diagram by arrow in figure 5.11. This cross over regime is termed as supercritical correlated(SCC) state. Interestingly both as grown and transferred crystal exhibit transition to SCC state upon heating as can be seen from the figure 5.12.

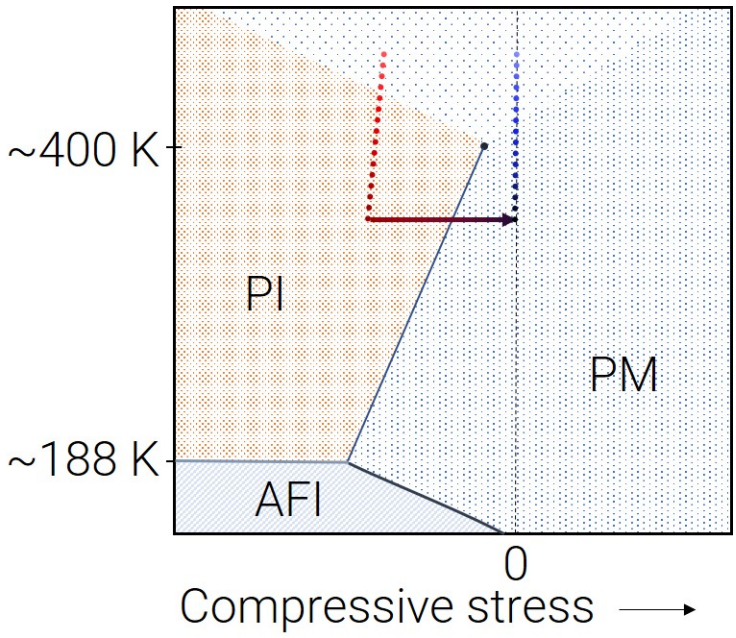

Figure 5.12: Phase diagram indicating that both as grown and transferred crystals from growth substrate enter supercritical correlated state upon heating. Reproduced from ref. [119]. Copyright American Physical Society 2019.

5.5.1 Material Characterization

5.5.1.1 CVD synthesis of V_2O_3

Chemical vapor deposition of V_2O_3 is performed in custom made reactor chamber which is equipped with optical access to the growth substrate. Chemical reactions can be optically observed in-situ as the synthesis process progress. This gives us freedom to control all possible parameters while monitoring the growth in-situ which helps in optimization of any CVD recipe much quicker than in any other conventional tubular furnaces where no optical access is possible[120]. We synthesize V_2O_3 nanoplates using salt assisted chemical vapor deposition process. Potassium Iodide is reacted with V_2O_5 to yield potassium vanadate which is further reduced to V_2O_3 upon reacting with hydrogen(H_2). Potassium vanadate is an intermediate compound in this reaction route which is more volatile and results in formation of very high quality V_2O_3 crystals at much lower growth temperature. Optical microscope images of an exemplary salt assisted CVD growth of

V_2O_3 is shown in figure 5.13.

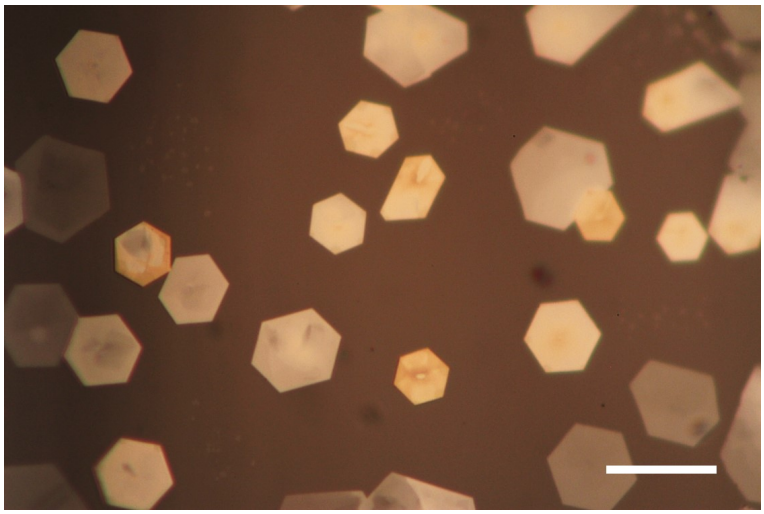

Figure 5.13: Optical microscope images of V_2O_3 crystals with different morphologies, shapes and thickness grown by salt-assisted chemical vapor deposition. Scale bar is 20μm. Reproduced from ref. [119]. Copyright American Physical Society 2019.

5.5.1.2 EDAX and TEM analysis

We performed energy dispersive x-ray spectroscopy to confirm the chemical composition of our grown crystals. Figure 5.14 (a) shows a low resolution transmission electron microscopy (TEM) image of a V_2O_3 flake transferred onto a TEM holey carbon grid.

Insets shows energy dispersive x-ray spectroscopic maps of the same crystal corresponding to vanadium(yellow) and oxygen(red) elements. Figure 5.14 (b) and (c) shows high resolution TEM image and selected area diffraction pattern respectively of the same crystal. SAED pattern clearly indicate single crystalline nature of our V_2O_3 CVD grown crystals.

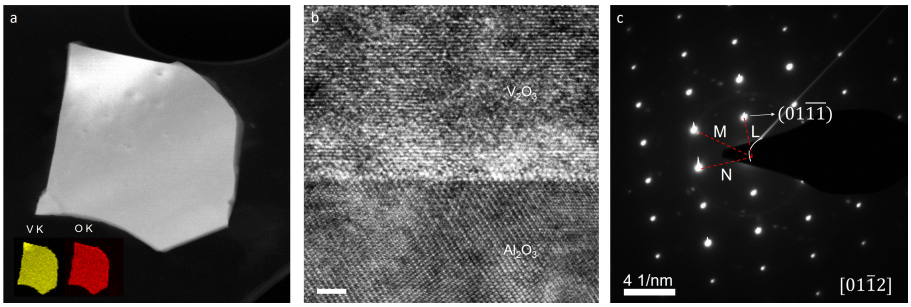

Figure 5.14: (a) Low resolution TEM image of V_2O_3 crystal transferred over holey carbon TEM grid. The insets shows EDS maps of vanadium(yellow) and oxygen(red) elements. (b) High resolution Cross-sectional TEM image of V_2O_3 crystal stackced on top of sapphire substrate. scale bar is 2nm. (c) Selected area diffraction pattern obtain from cross-sectional TEM sample. This pattern matched uniquely with HCP $[01\bar{1}2]$ diffraction pattern. Reproduced from ref. [119]. Copyright American Physical Society 2019.

5.5.1.3 Raman Spectroscopy

As discussed earlier, stress play an important role in structural phase transition of V_2O_3. As the crystal grown on sapphire substrate are under stress due to lattice mismatch, the crystals stay in paramagnetic insulator(PI) phase. Raman spectrum of as grown crystals on sapphire substrate is plotted in Figure 5.15 with red line. Peak positions corresponding to E_g(in plane) vibration modes are 248, 305, and 590cm^{-1}. Out of plane vibration mode A_{1g} peak position can be found at 514cm^{-1}. These value are in excellent agreement with the reported values in literature for the V_2O_3 PI phase[121].

Once the crystals are transferred from the growth substrate or agitated vigorously, the stress on the crystals is released causing a phase change from paramagnetic insulator to paramagnetic metallic. As can be seen in figure 5.15, the Raman spectrum plotted in blue exhibits shift in peak positions as compared to PI phase Raman spectrum. The new peak positions along with shoulder to the 237cm^{-1} can be clearly seen and matches very well with the reported value of V_2O_3 PM phase[122].

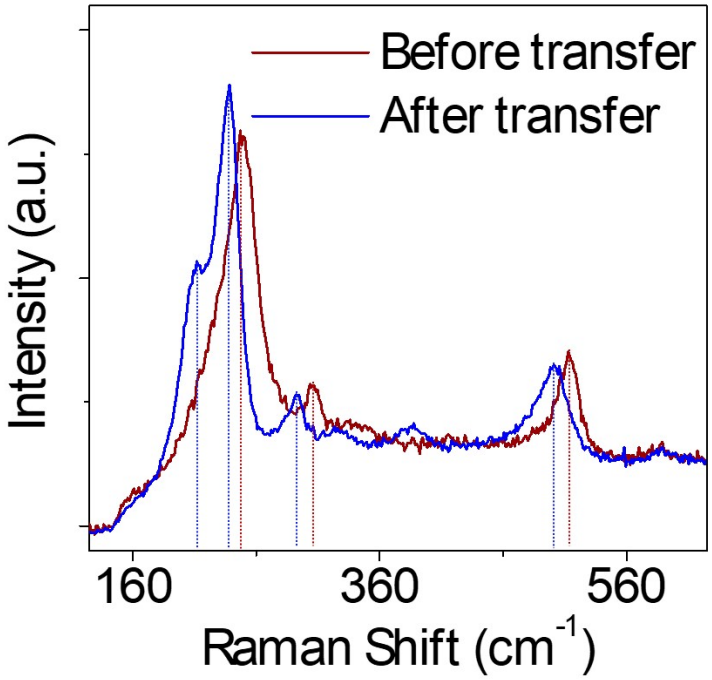

Figure 5.15: Raman spectrum of as-grown (red) and transferred V_2O_3 crystals from sapphire substrate. The shift in the peak positions can be seen along with appearance of a shoulder to the 248cm^{-1} peak. Reproduced from ref. [119]. Copyright American Physical Society 2019.

5.5.2 Thermal Conductivity of Metallic V_2O_3

In order to check validity of our proposed technique, we measured thermal conductivity of metallic V_2O_3 crystals grown by chemical vapor deposition. The thermal conductivity value of metallic V_2O_3 is well reported in literature. We chose this material as a reference material to test our method. From thin layers to bulk form, V_2O_3 does not show significant change in the properties. Thermal conductivity of the metallic V_2O_3 is 4.5 W/m.K at room temperature[123]. The chosen crystal in our experiment has a thickness of 130nm to have a better comparison with the samples used in literature. The absorption coefficient that we used in our calculations is 0.8 that we took from previous report in literature[124]. Figure 5.16 (a) and (b) shows optical micrograph and reflection map obtained by SPCM respectively. Photoresponse is recorded at -200mV to 200mV biases with

50mV step. Typical photocurrent map and FEM simulation for thermal profile is plotted in figure 5.16 (c) and (d) respectively. Under 95μW laser power, the rise in temperature at the center of the hole is 2.5K above room temperature. The slightly elongated bolometric response can be due to trapped air pocket under the crystal near the hole. We measured thermal conductivity of V_2O_3 after using κ as a fitting parameter and matching the expected resistance change value to the measured resistance change value to be 4.5$\pm$1 W/m.K which is in excellent agreement with the reported value in literature as mentioned earlier.

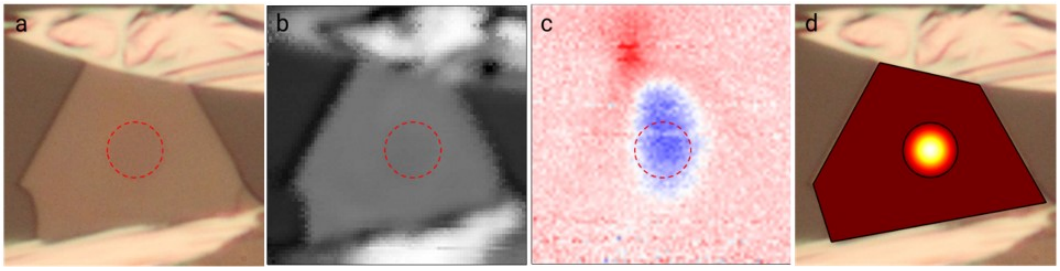

Figure 5.16: (a) Optical microscope image of V_2O_3 device prepared for thermal conductivity measurements. The red dashed line represents the location of hole under the crystal. (b) Reflection map collected during SPCM of the same device. (c) Photocurrent map of the device under applied bias. (d) FEM simulation of thermal profile of the devices mapped onto optical microscope image. Under 9.5 μW laser power, the maximum temperature rise at the center of the hole is 2.5K above room temperature. Reproduced from ref. [115]. Copyright IOP Publishing Ltd. 2020.

5.6 Thermal Conductivity measurements of 2H Tantallum DiSulfide(TaS_2)

5.6.1 Material Characterization

2H Tantallum DiSulfide (TaS_2) is member of metallic transition metal dichalcogenide family with very interesting properties. At around 0.5K, this material undergoes superconducting phase transition[125] while around 75K, charge density wave phase transition happens[126]. As we thin down the material and number of layers decrease, the superconducting transition temperature increases from 0.5K to 2.5K[127].

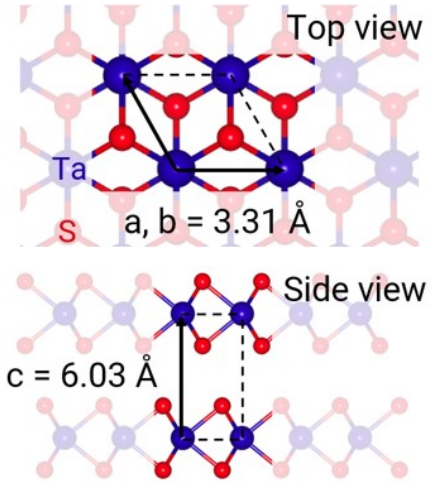

Figure 5.17: schematic of top and side view of the 2H stacked TaS_2 crystal in the upper and lower pannel respectively. Lower layer is rotated by an angle of 60^0 with respect to upper layer. Ta and S atoms are marked on the schematic.

Crystal structure of 2H-TaS_2 is shown in figure 5.17. Upper panel show the top view of 2H stacked layers of the material. The bottom layer is twisted by an angle of 60^0 with respect to upper layer. In the lower panel, side view of the TaS_2 crystal structure is drawn.

Raman spectroscopy is performed on mechanically exfoliated crystals. Raman spectrum of the crystal can be seen in figure 5.18. Two characteristic peaks

can be seen at peak positions 287cm^{-1} (E_{2g}) and 332cm^{-1} (A_{1g}). E_{2g} mode corresponds to inplane vibration mode while A_{1g} is out of plane vibration mode. These peak positions are consistent with the values reported in literature for 2H-TaS_2 polytype[128].

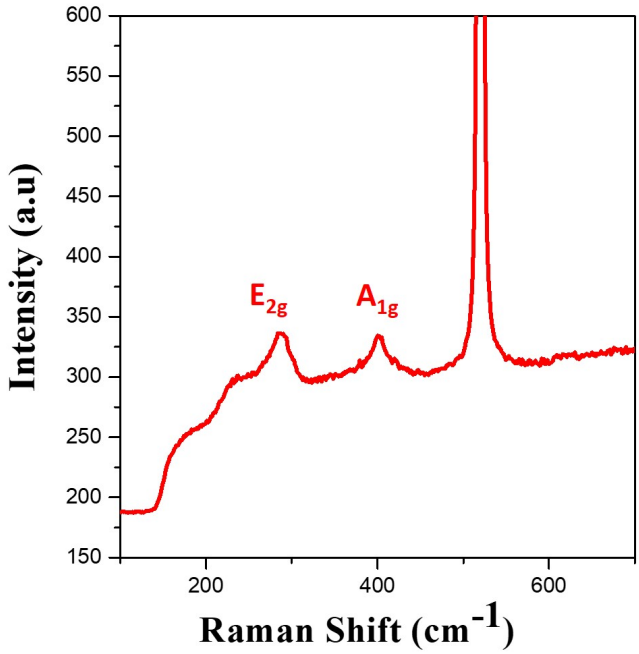

Figure 5.18: Raman spectrum of 2H-TaS_2 mechanical exfoliated crystal. Two characteristic peak a labeled E_{2g} and A_{1g} which correspond to inplane and out of plane vibration modes of phonons respectively.

5.6.2 Thermal conductivity of 2H-TaS_2

In this work, we calculated the thermal conductivity of 2H-TaS_2 for the first time. Devices with similar thickness values were fabricated to have consistent results. Figure 5.19 (a) shows typical measurement setup to obtain the photocurrent map. A crystal of thickness 32nm (determined from atomic force microscopy) is transferred on top of a pre-patterned gold electrodes using all dry visco-elastic stamping method[129]. Details of this fabrication process has already been described in experimental methods part. The hole with a radius of a=2μm drilled

using FIB to a depth of 1μm. A pre-amplifier act as a virtual ground and measures current produced by the dc applied bias and focused Gaussian laser beam. The output current from pre-amplifier is fed to lock-in amplifier which is referenced by a laser chopper operating at a certain frequency. The change in current due to laser beam can be calculated by this measurement.

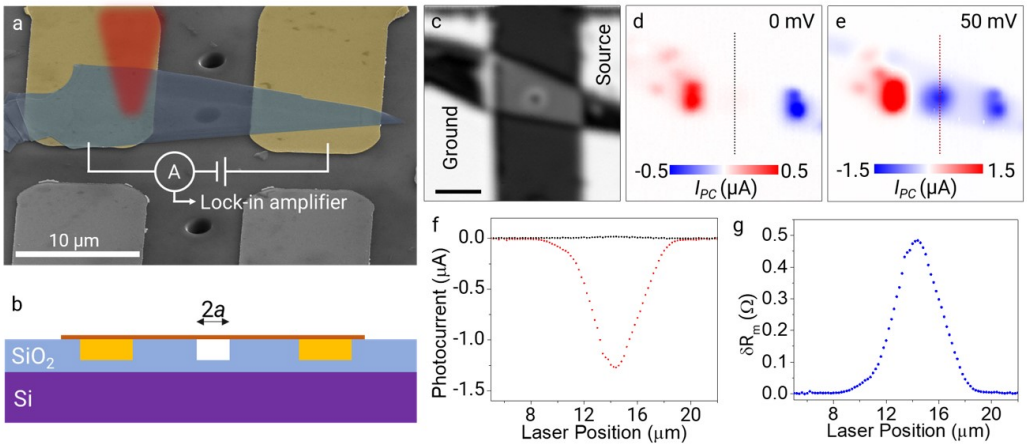

Figure 5.19: (a) Schematic of proposed thermal conductivity measurement method. The red cone symbolize focused Gaussian beam chopped at a certain frequency. Current under applied dc bias is measured through pre-amplifier which a fed to lock-in amplifier referenced by the laser chopper.(b) Cross-section schematic of the fabricated device. (c) Typical reflection map obtained by SPCM. scale bar is 5μm(d) Photocurrent map under zero applied bias. Photocurrent generated due to Seebeck at the metal-TaS_2 junctions can be seen. (e) Photocurrent map under 50mV applied bias. Negative photoresponse can be seen coming from whole crystal. The photocurrent at suspended part of crystal is distinctly decreased. (f) Line traces through the dashed lines drawn over zero and 50mV photocurrent maps. (g) Resistance change extracted for each laser position corresponding to photocurrent trace line plotted. Reproduced from ref. [115]. Copyright IOP Publishing Ltd. 2020.

Figure 5.19 (c) shows a typical reflection map obtained by scanning photocurrent microscopy. Bias is applied from right electrode and left contact act as ground in the measurement setup. Figure 5.19 (d) and (e) shows the photocurrent maps obtained under zero and 50mV applied bias respectively using 642nm wavelength laser. Under no applied bias, we observe a very localized photoresponse from only metal/TaS_2 junction. This is due to electromotive force produced by the Seebeck effect at the metal/metal interface. When we apply bias, the photoresponse is

observed from all over the crystal along with distinct reduction in photocurrent at the suspended part of the crystal over the hole. This reduction in photocurrent is dictated by photo-bolometric effect which is photoresponse generated due to local resistance change under focused laser beam heating. Figure 5.19 (f) shows the line traces taken along the black and red dashed line drawn over the zero and 50mV bias photocurrent maps. Negative photoresponse along with pronounced photocurrent reduction over the suspended part of the crystal can been clearly in the line trace obtained from 50mV bias photocurrent map. Figure 5.19 (g) is the corresponding measured change in the resistance taken at each laser position. Resistance change from the center of the hole is used to calculate thermal conductivity of the material. We calculated the in-plane thermal conductivity of 2H-TaS_2 as 13±1.0 W/m.K. We performed experiments using 532nm wavelength laser as well which yielded similar thermal conductivity values with in the error margin.

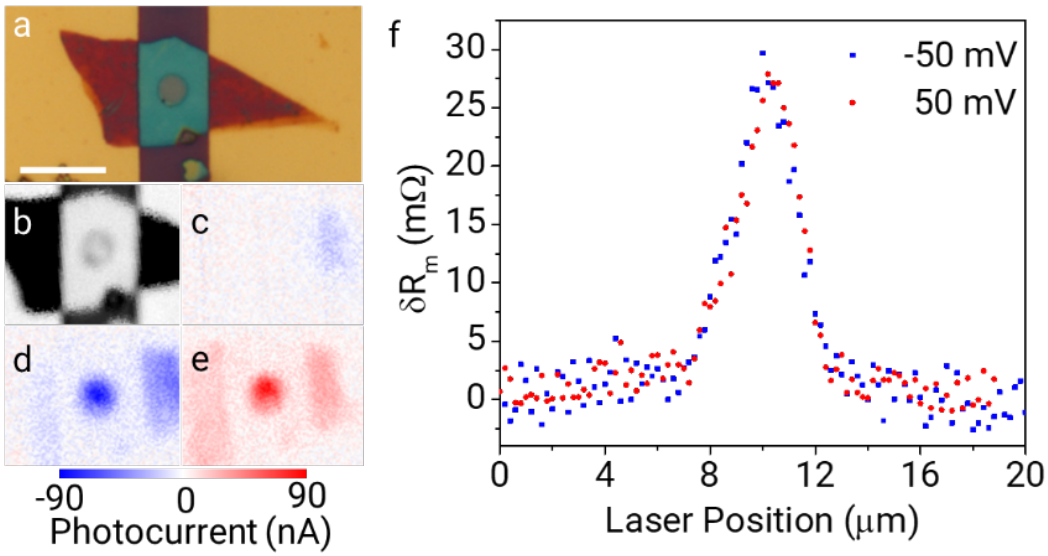

Figure 5.20: (a) Optical microscope image of fabricated device.(b) Reflection map obtained during SPCM.(c),(d) and (e) shows photocurrent maps under 0mV, 50mV and -50mV respectively.(f) Corresponding resistance change plotted as a function of laser position. Reproduced from ref. [115]. Copyright IOP Publishing Ltd. 2020.

Figure 5.20 (a) shows the optical micrograph of the fabricated 2H-TaS_2 devices which is scanned by 532nm laser. Figure 5.20(b) is the reflection map obtained

Sample #	Measurement Wavelength (nm)	Thickness (nm)	Absorption Coefficient (α)	Laser Power (µW)	Dark Resistance (Ω)	$\rho(T)$ (mΩ.cm)	δR (Ω)	κ(W/m.K)
1	642	34.0	0.33	40	124	0.60 (1+0.0025K^{-1} $[T-T_0]$)	0.019±0.001	12.6 ± 0.7
2	532	19.1	0.28	10	131	0.34 (1+0.0025K^{-1} $[T-T_0]$)	0.027±0.001	14.0 ± 1.0
3	642	32.1	0.33	211	138	0.25 (1+0.0025K^{-1} $[T-T_0]$)	0.48±0.01	14.0 ± 1.0
4	642	33.1	0.33	211	267	0.52 (1+0.0025K^{-1} $[T-T_0]$)	0.75±0.01	12.0 ± 1.0
Average								13.2 ± 1.0

Table 5.1: Thermal conductivity(κ) values calculated for four different samples. Different laser powers along with wavelengths used to measure thermal conductivity. All yielded similar κ values with in error margin. Reproduced from ref. [115]. Copyright IOP Publishing Ltd. 2020.

by SPCM. Figure 5.20 (c), (d) and (e) shows photocurrent maps obtained under zero, 50mV and -50mV applied bias. Zero bias scan results in production of localized photocurrent at metal/2H-TaS_2 junction due to Seebeck effect. Under 50mV and -50mV the photocurrent produced is due to resistance change caused by focused laser beam heating (photobolometric effect). The measured resistance change cause by laser beam heating is plotted at each laser position along a line passing through the center of the hole. As can be seen, for both 50mV and -50mV applied bias, the trend of resistance change is similar. From comparing the value of measured resistance change to expected resistance change(obtained through COMSOL simulation), the value of thermal conductivity is calculated. Data calculated for four fabricated devices is shown in table 5.1. Different laser power, different illumination wavelengths and different thickness crystals, all yielded similar thermal conductivity values with in the error margin. Average κ value calculated by our measurement method for 2H-TaS_2 is 13.2±1.

5.7 Thermal Conductivity Measurement of Semiconducting Materials

Bolometric response from intrinsic semiconductors is very well defined and can be described with Arrhenius relation. Under focused laser illumination, the photoresponse from these materials can result from many mechanism altogether. So it becomes extremely challenging to separate contribution of each mechanism in the

generated photocurrent. We performed experiments on very well studied semiconducting TMDCs tungsten disulfide(WS_2) and molybdenum disulfide (MoS_2). Thermal conductivity of these materials are well reported in literature using different methods. As photocurrent in semiconducting materials can be a result of non-equilibrium carrier formation due to absorption of light, built in electric field induced separation of non-equilibrium carriers and photothermal effect. In order to apply bolometry based thermal conductivity measurement methods, each of these effect needs to be distinguished from each other. A WS_2 device fabricated using a 12nm thick crystal is shown in figure 5.21 (a). The photoconductance changes at different applied bias which is a clear indication of existence of more than one photocurrent generation mechanism. This makes the applicability of our proposed method to calculate thermal conductivity of WS_2 very difficult and sole extraction of bolometric response is not a straightforward thing to do.

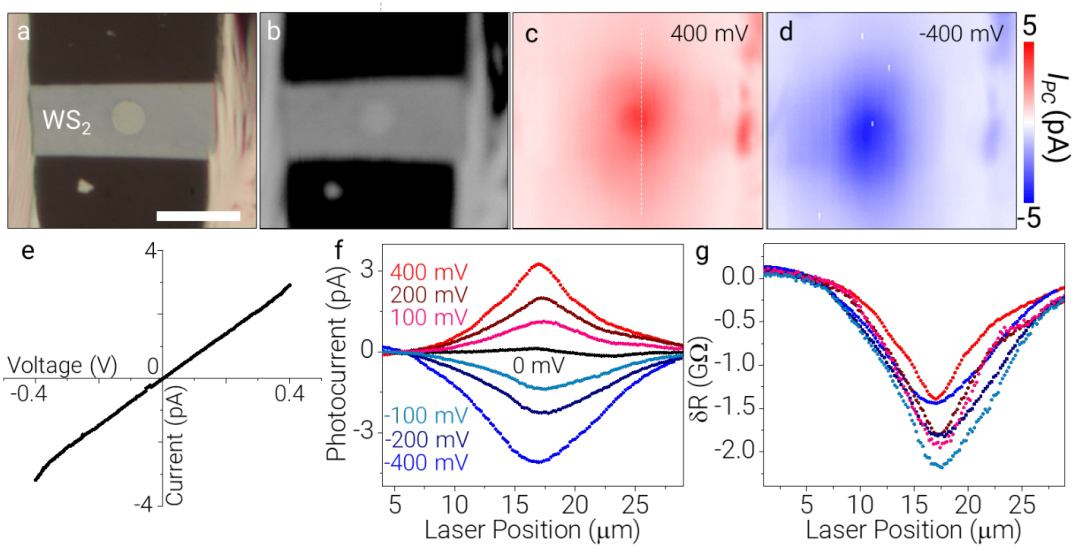

Figure 5.21: (a)Optical image of fabricated top indium contact device.(b) Reflection map of the same device obtained by SPCM.(c)-(d) photocurrent maps collected under 400mV and -400mV applied bias respectively.(e) Characteristic current vs voltage plot in a bias sweep range of 400mV to -400mV.(f) Line traces from the photocurrent maps through the center of the hole for different applied biases.(g) Corresponding resistance change plotted as every laser position. Reproduced from ref. [115]. Copyright IOP Publishing Ltd. 2020.

When we tried to implement our proposed method to MoS_2. Figure5.22(a) and (b) shows optical image and reflection map of the fabricated device respectively.

Figure5.22 (c) and (d) shows plotted photocurrent maps under zero and 1V applied bias respectively. As can be seen from zero bias photocurrent map, a very interesting bipolar photoresponse is generated at the suspended part of crystal which we hypothesize can be due to stress induced local electric field with in the suspended region. At 1V applied bias, the response is still very complicated and can not be considered purely bolometeric. This limits the applicability of our method to MoS_2 crystals as well.

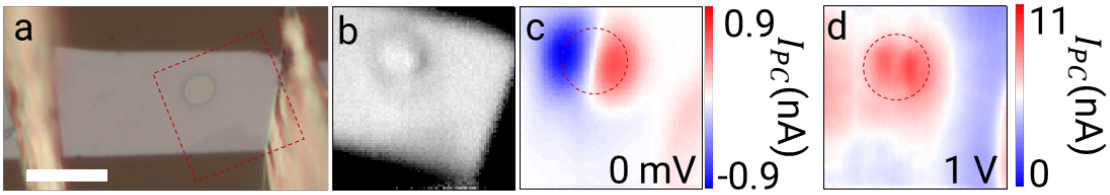

Figure 5.22: (a)Optical image of fabricated top indium contact device.(b) Reflection map of the same device obtained by SPCM.(c)-(d) photocurrent maps collected under 400mV and -400mV applied bias respectively.(e) Characteristic current vs voltage plot in a bias sweep range of 400mV to -400mV.(f) Line traces from the photocurrent maps through the center of the hole for different applied biases.(g) Corresponding resistance change plotted as every laser position. Reproduced from ref. [115]. Copyright IOP Publishing Ltd. 2020.

Chapter 6

Conclusion

In conclusion, we studied the photoresponse of several novel 2D materials and explored the possible mechanism responsible for that. We utilized scanning photocurrent microscopy in order to obtain spatial maps of photocurrent through the material. The metallic TMDCs exhibit localized photocurrent generation at zero applied bias due to Seebeck effect. The photothermally induced electromotive force causes the photocurrent generation at the metal/metal interface under zero applied bias. Under finite applied bias, the generated photocurrent is observed through out the crystal which is dominated by photothermally induced photobolometric effect. The local change in resistance caused by the localized heating by a tightly focused Gaussian laser beam decreases the conductivity of the material locally. As a result, negative photocuductance is observed due to reduction in dc current passing through the crystal because of laser heating. As the change in conductivity is purely due to localized laser heating, the applied bias has no effect on the photoconductivity. Hence the measured photoconductivity is independent of the applied bias.

Once we established that photo-bolometric effect is responsible for the photocurrent generation through atomically thin TMDCs, we extended our study to correlate thermal conductivity of these materials with change in resistance caused by photothermally induced photo-bolometric effect. Using kappa(κ) as

a fitting parameter, we correlated thermal conductivity to the resistance change of nano-sheets caused by focused laser beam heating. Our proposed method has several advantages in terms of simplicity, less complicated analysis, easy sample preparation and non-destructive technique for the material. The accuracy and sensitivity of the measured thermal conductivity is very high. This gives researcher another way to compute thermal conductivity of several 2D materials and nano-sheets with high precision which can help in designing better thermal and thermo-electric devices.

6.1 Research Topics Outside Scope of This Thesis

Some of the techniques that I learned during above mentioned works yielded very useful contributions towards some more publications. The drilling of holes on the SiO_2 substrate was useful for the study of mechanical properties of metallic TMDCs. Atomically thin layers of different TMDCs were suspended over a hole using all dry viscoelestic stamping method (see figure6.1) and then indented at the center by a nano-indenter (in our case AFM tip) to measure Young's modulus of the material. I performed several crystal transfers and data analysis for this project. This work will be submitted soon for the publication.

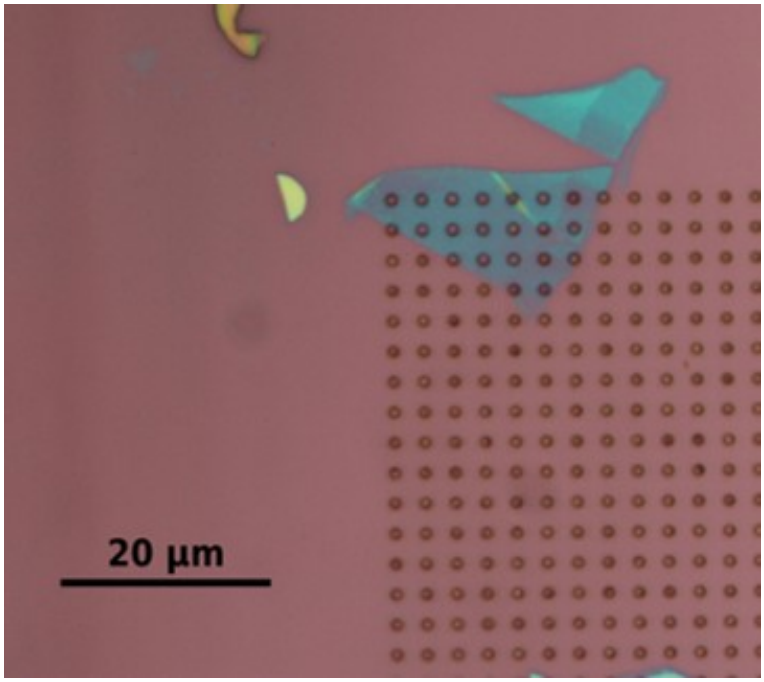

Figure 6.1: TaS_2 crystal transferred over array of holes prepared by electron beam lithography and ICP etching. Several similar samples were prepared to study mechanical properties of this material.

In another work, we studied electrical properties and chemical composition of CVD grown Molybdenum carbide Mo_2C crystals[130]. I performed scanning electron microscopy of the samples and collected electron dispersive spectroscopy data to confirm the chemical composition of the material. Also for electrical characterization, I prepared top contact indium devices and performed IV measurements of the devices, methods of which has been discussed in previous chapters.

Currently we are working on a two dimensional ionic conductor for neuromorphic computing application. For this project I am solely responsible for the device fabrication. We prepare complex Indium contact devices on a graphite contacted K-MnO_2 crystals which can be seen in figure6.2. I performed IV measurements of some devices. For material characterization, I performed Raman and electron dispersive spectroscopy on these crystals. I prepared several TEM samples for HRTEM measurements as well. This work is still in progress and will be submitted soon for publication.

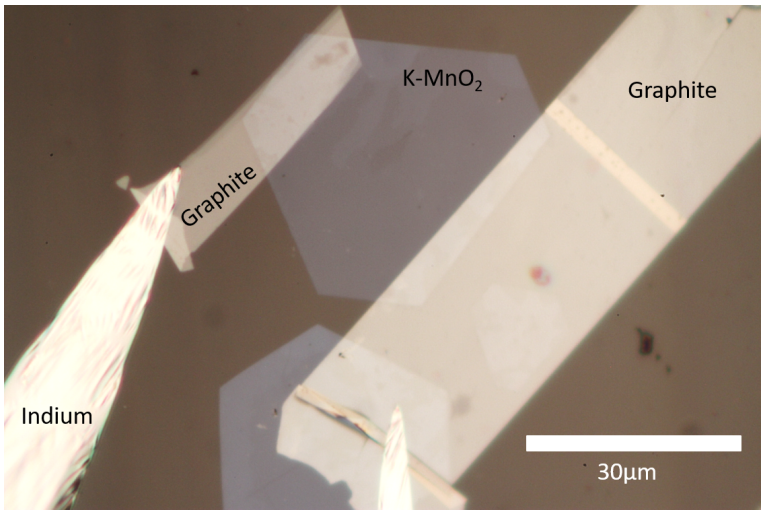

Figure 6.2: Optical image of $KMnO_2$ device. Graphite crystals exfoliated and transferred deterministicaly on top of hexagon shaped $KMnO_2$ crystal with extremely fine alignment. Indium needles can be seen in bright silver contrast contacted with graphite electrodes for electrical connection.

Bibliography

[1] K. S. Novoselov, D. Jiang, F. Schedin, T. Booth, V. Khotkevich, S. Morozov, and A. K. Geim, "Two-dimensional atomic crystals," *Proceedings of the National Academy of Sciences*, vol. 102, no. 30, pp. 10451–10453, 2005.

[2] K. S. Novoselov, A. K. Geim, S. V. Morozov, D. Jiang, Y. Zhang, S. V. Dubonos, I. V. Grigorieva, and A. A. Firsov, "Electric field effect in atomically thin carbon films," *science*, vol. 306, no. 5696, pp. 666–669, 2004.

[3] Z. Ni, Q. Liu, K. Tang, J. Zheng, J. Zhou, R. Qin, Z. Gao, D. Yu, and J. Lu, "Tunable bandgap in silicene and germanene," *Nano letters*, vol. 12, no. 1, pp. 113–118, 2012.

[4] M. Derivaz, D. Dentel, R. Stephan, M.-C. Hanf, A. Mehdaoui, P. Sonnet, and C. Pirri, "Continuous germanene layer on al (111)," *Nano letters*, vol. 15, no. 4, pp. 2510–2516, 2015.

[5] S. Das, W. Zhang, M. Demarteau, A. Hoffmann, M. Dubey, and A. Roelofs, "Tunable transport gap in phosphorene," *Nano letters*, vol. 14, no. 10, pp. 5733–5739, 2014.

[6] A. Carvalho, M. Wang, X. Zhu, A. S. Rodin, H. Su, and A. H. C. Neto, "Phosphorene: from theory to applications," *Nature Reviews Materials*, vol. 1, no. 11, pp. 1–16, 2016.

[7] W. Li, L. Kong, C. Chen, J. Gou, S. Sheng, W. Zhang, H. Li, L. Chen, P. Cheng, and K. Wu, "Experimental realization of honeycomb borophene," *Science Bulletin*, vol. 63, no. 5, pp. 282–286, 2018.

[8] H. Jiang, Z. Lu, M. Wu, F. Ciucci, and T. Zhao, "Borophene: a promising anode material offering high specific capacity and high rate capability for lithium-ion batteries," *Nano Energy*, vol. 23, pp. 97–104, 2016.

[9] J. Ji, X. Song, J. Liu, Z. Yan, C. Huo, S. Zhang, M. Su, L. Liao, W. Wang, Z. Ni, *et al.*, "Two-dimensional antimonene single crystals grown by van der waals epitaxy," *Nature communications*, vol. 7, no. 1, pp. 1–9, 2016.

[10] C. Gibaja, D. Rodriguez-San-Miguel, P. Ares, J. Gómez-Herrero, M. Varela, R. Gillen, J. Maultzsch, F. Hauke, A. Hirsch, G. Abellán, *et al.*, "Few-layer antimonene by liquid-phase exfoliation," *Angewandte Chemie International Edition*, vol. 55, no. 46, pp. 14345–14349, 2016.

[11] B. Aufray, A. Kara, S. Vizzini, H. Oughaddou, C. Léandri, B. Ealet, and G. Le Lay, "Graphene-like silicon nanoribbons on ag (110): A possible formation of silicene," *Applied Physics Letters*, vol. 96, no. 18, p. 183102, 2010.

[12] B. Lalmi, H. Oughaddou, H. Enriquez, A. Kara, S. Vizzini, B. Ealet, and B. Aufray, "Epitaxial growth of a silicene sheet," *Applied Physics Letters*, vol. 97, no. 22, p. 223109, 2010.

[13] T. F. Jaramillo, K. P. Jørgensen, J. Bonde, J. H. Nielsen, S. Horch, and I. Chorkendorff, "Identification of active edge sites for electrochemical h2 evolution from mos2 nanocatalysts," *science*, vol. 317, no. 5834, pp. 100–102, 2007.

[14] H. I. Karunadasa, E. Montalvo, Y. Sun, M. Majda, J. R. Long, and C. J. Chang, "A molecular mos2 edge site mimic for catalytic hydrogen generation," *Science*, vol. 335, no. 6069, pp. 698–702, 2012.

[15] S. Manzeli, D. Ovchinnikov, D. Pasquier, O. V. Yazyev, and A. Kis, "2d transition metal dichalcogenides," *Nature Reviews Materials*, vol. 2, no. 8, p. 17033, 2017.

[16] D. Sarkar, W. Liu, X. Xie, A. C. Anselmo, S. Mitragotri, and K. Banerjee, "Mos2 field-effect transistor for next-generation label-free biosensors," *ACS nano*, vol. 8, no. 4, pp. 3992–4003, 2014.

[17] K. Kalantar-zadeh and J. Z. Ou, "Biosensors based on two-dimensional mos2," *Acs Sensors*, vol. 1, no. 1, pp. 5–16, 2016.

[18] X. Gan, H. Zhao, and X. Quan, "Two-dimensional mos2: a promising building block for biosensors," *Biosensors and Bioelectronics*, vol. 89, pp. 56–71, 2017.

[19] H. Tan, Y. Fan, Y. Zhou, Q. Chen, W. Xu, and J. H. Warner, "Ultrathin 2d photodetectors utilizing chemical vapor deposition grown ws2 with graphene electrodes," *ACS nano*, vol. 10, no. 8, pp. 7866–7873, 2016.

[20] X. Wang, P. Wang, J. Wang, W. Hu, X. Zhou, N. Guo, H. Huang, S. Sun, H. Shen, T. Lin, *et al.*, "Ultrasensitive and broadband mos2 photodetector driven by ferroelectrics," *Advanced materials*, vol. 27, no. 42, pp. 6575–6581, 2015.

[21] P. Cheng, K. Sun, and Y. H. Hu, "Memristive behavior and ideal memristor of 1t phase mos2 nanosheets," *Nano letters*, vol. 16, no. 1, pp. 572–576, 2016.

[22] X. Yan, Q. Zhao, A. P. Chen, J. Zhao, Z. Zhou, J. Wang, H. Wang, L. Zhang, X. Li, Z. Xiao, *et al.*, "Vacancy-induced synaptic behavior in 2d ws2 nanosheet–based memristor for low-power neuromorphic computing," *Small*, vol. 15, no. 24, p. 1901423, 2019.

[23] S. Larentis, B. Fallahazad, and E. Tutuc, "Field-effect transistors and intrinsic mobility in ultra-thin mose2 layers," *Applied Physics Letters*, vol. 101, no. 22, p. 223104, 2012.

[24] R. G. Dickinson and L. Pauling, "The crystal structure of molybdenite," *Journal of the American Chemical Society*, vol. 45, no. 6, pp. 1466–1471, 1923.

[25] T. Liang, Y. Cai, H. Chen, and M. Xu, "Two-dimensional transition metal dichalcogenides: An overview," pp. 1–27, 2019.

[26] S. Manzeli, D. Ovchinnikov, D. Pasquier, O. V. Yazyev, and A. Kis, "2d transition metal dichalcogenides," *Nature Reviews Materials*, vol. 2, no. 8, p. 17033, 2017.

[27] A. Beal and H. Hughes, "Kramers-kronig analysis of the reflectivity spectra of 2h-mos2, 2h-mose2 and 2h-mote2," *Journal of Physics C: Solid State Physics*, vol. 12, no. 5, p. 881, 1979.

[28] B. Mahler, V. Hoepfner, K. Liao, and G. A. Ozin, "Colloidal synthesis of 1t-ws2 and 2h-ws2 nanosheets: applications for photocatalytic hydrogen evolution," *Journal of the American Chemical Society*, vol. 136, no. 40, pp. 14121–14127, 2014.

[29] Q. Tang and D.-e. Jiang, "Mechanism of hydrogen evolution reaction on 1t-mos2 from first principles," *Acs Catalysis*, vol. 6, no. 8, pp. 4953–4961, 2016.

[30] Y. Yin, Y. Zhang, T. Gao, T. Yao, X. Zhang, J. Han, X. Wang, Z. Zhang, P. Xu, P. Zhang, *et al.*, "Synergistic phase and disorder engineering in 1t-mose2 nanosheets for enhanced hydrogen-evolution reaction," *Advanced Materials*, vol. 29, no. 28, p. 1700311, 2017.

[31] E. Revolinsky and D. Beerntsen, "Electrical properties of the mote2- wte2 and mose2- wse2 systems," *Journal of Applied Physics*, vol. 35, no. 7, pp. 2086–2089, 1964.

[32] Y. Kim, Y. I. Jhon, J. Park, J. H. Kim, S. Lee, and Y. M. Jhon, "Anomalous raman scattering and lattice dynamics in mono-and few-layer wte 2," *Nanoscale*, vol. 8, no. 4, pp. 2309–2316, 2016.

[33] C. H. Naylor, W. M. Parkin, J. Ping, Z. Gao, Y. R. Zhou, Y. Kim, F. Streller, R. W. Carpick, A. M. Rappe, M. Drndic, *et al.*, "Monolayer single-crystal 1t-mote2 grown by chemical vapor deposition exhibits weak antilocalization effect," *Nano letters*, vol. 16, no. 7, pp. 4297–4304, 2016.

[34] Y. Yu, G.-H. Nam, Q. He, X.-J. Wu, K. Zhang, Z. Yang, J. Chen, Q. Ma, M. Zhao, Z. Liu, *et al.*, "High phase-purity 1t-mos 2-and 1t-mose 2-layered crystals," *Nature chemistry*, vol. 10, no. 6, pp. 638–643, 2018.

[35] S. Cho, S. Kim, J. H. Kim, J. Zhao, J. Seok, D. H. Keum, J. Baik, D.-H. Choe, K. J. Chang, K. Suenaga, *et al.*, "Phase patterning for ohmic homojunction contact in mote2," *Science*, vol. 349, no. 6248, pp. 625–628, 2015.

[36] R. Kappera, D. Voiry, S. E. Yalcin, B. Branch, G. Gupta, A. D. Mohite, and M. Chhowalla, "Phase-engineered low-resistance contacts for ultrathin mos 2 transistors," *Nature materials*, vol. 13, no. 12, pp. 1128–1134, 2014.

[37] J. Zhou, J. Lin, X. Huang, Y. Zhou, Y. Chen, J. Xia, H. Wang, Y. Xie, H. Yu, J. Lei, *et al.*, "A library of atomically thin metal chalcogenides," *Nature*, vol. 556, no. 7701, pp. 355–359, 2018.

[38] J. Sun, G. Tang, C. Li, X. Ji, W. Liang, and H. Tang, "Synthesis and tribological properties of hexagonal nbse2 nanoplates," *Micro & Nano Letters*, vol. 8, no. 6, pp. 294–297, 2013.

[39] Y. Huang, R. Chen, J. Zhang, and Y. Huang, "Electronic transport in nbse 2 two-dimensional nanostructures: semiconducting characteristics and photoconductivity," *Nanoscale*, vol. 7, no. 45, pp. 18964–18970, 2015.

[40] H. Wang, X. Huang, J. Lin, J. Cui, Y. Chen, C. Zhu, F. Liu, Q. Zeng, J. Zhou, P. Yu, *et al.*, "High-quality monolayer superconductor nbse 2 grown by chemical vapour deposition," *Nature communications*, vol. 8, no. 1, pp. 1–8, 2017.

[41] X. Xi, Z. Wang, W. Zhao, J.-H. Park, K. T. Law, H. Berger, L. Forró, J. Shan, and K. F. Mak, "Ising pairing in superconducting nbse 2 atomic layers," *Nature Physics*, vol. 12, no. 2, pp. 139–143, 2016.

[42] M. Abdel-Hafiez, X.-M. Zhao, A. Kordyuk, Y.-W. Fang, B. Pan, Z. He, C.-G. Duan, J. Zhao, and X.-J. Chen, "Enhancement of superconductivity under pressure and the magnetic phase diagram of tantalum disulfide single crystals," *Scientific reports*, vol. 6, p. 31824, 2016.

[43] R. Yan, G. Khalsa, B. T. Schaefer, A. Jarjour, S. Rouvimov, K. C. Nowack, H. G. Xing, and D. Jena, "Thickness dependence of superconductivity in ultrathin nbs2," *Applied Physics Express*, vol. 12, no. 2, p. 023008, 2019.

[44] Y. Zhang, L. Yin, J. Chu, T. A. Shifa, J. Xia, F. Wang, Y. Wen, X. Zhan, Z. Wang, and J. He, "Edge-epitaxial growth of 2d nbs2-ws2 lateral metal-semiconductor heterostructures," *Advanced Materials*, vol. 30, no. 40, p. 1803665, 2018.

[45] Q. Zhang, X.-F. Wang, S.-H. Shen, Q. Lu, X. Liu, H. Li, J. Zheng, C.-P. Yu, X. Zhong, L. Gu, *et al.*, "Simultaneous synthesis and integration of two-dimensional electronic components," *Nature Electronics*, vol. 2, no. 4, pp. 164–170, 2019.

[46] M. Buscema, M. Barkelid, V. Zwiller, H. S. van der Zant, G. A. Steele, and A. Castellanos-Gomez, "Large and tunable photothermoelectric effect in single-layer mos2," *Nano letters*, vol. 13, no. 2, pp. 358–363, 2013.

[47] C.-C. Wu, D. Jariwala, V. K. Sangwan, T. J. Marks, M. C. Hersam, and L. J. Lauhon, "Elucidating the photoresponse of ultrathin mos2 field-effect transistors by scanning photocurrent microscopy," *The Journal of Physical Chemistry Letters*, vol. 4, no. 15, pp. 2508–2513, 2013.

[48] H. Song, J. Liu, B. Liu, J. Wu, H.-M. Cheng, and F. Kang, "Two-dimensional materials for thermal management applications," *Joule*, vol. 2, no. 3, pp. 442–463, 2018.

[49] A. A. Balandin, S. Ghosh, W. Bao, I. Calizo, D. Teweldebrhan, F. Miao, and C. N. Lau, "Superior thermal conductivity of single-layer graphene," *Nano letters*, vol. 8, no. 3, pp. 902–907, 2008.

[50] D. L. Nika, E. P. Pokatilov, and A. A. Balandin, "Theoretical description of thermal transport in graphene: The issues of phonon cut-off frequencies and polarization branches," *physica status solidi (b)*, vol. 248, no. 11, pp. 2609–2614, 2011.

[51] C.-M. Ye, B.-Q. Shentu, and Z.-X. Weng, "Thermal conductivity of high density polyethylene filled with graphite," *Journal of Applied Polymer Science*, vol. 101, no. 6, pp. 3806–3810, 2006.

[52] R. Yan, J. R. Simpson, S. Bertolazzi, J. Brivio, M. Watson, X. Wu, A. Kis, T. Luo, A. R. Hight Walker, and H. G. Xing, "Thermal conductivity of monolayer molybdenum disulfide obtained from temperature-dependent raman spectroscopy," *ACS nano*, vol. 8, no. 1, pp. 986–993, 2014.

[53] N. Peimyoo, J. Shang, W. Yang, Y. Wang, C. Cong, and T. Yu, "Thermal conductivity determination of suspended mono-and bilayer ws 2 by raman spectroscopy," *Nano Research*, vol. 8, no. 4, pp. 1210–1221, 2015.

[54] A. Rose, *Concepts in photoconductivity and allied problems*. No. 19, Interscience publishers, 1963.

[55] R. H. Bube, *Photoelectronic properties of semiconductors*. Cambridge University Press, 1992.

[56] S. BEA and M. Teich, ""fundamentals of photonics"," *Wiley*, p. 313, 1991.

[57] G. Konstantatos and E. H. Sargent, "Nanostructured materials for photon detection," *Nature nanotechnology*, vol. 5, no. 6, pp. 391–400, 2010.

[58] F. J. Zutavern, G. M. Loubriel, M. O'malley, L. Shanwald, W. Helgeson, D. McLaughlin, and B. McKenzie, "Photoconductive semiconductor switch experiments for pulsed power applications," *IEEE transactions on electron devices*, vol. 37, no. 12, pp. 2472–2477, 1990.

[59] H. Beneking, "On the response behavior of fast photoconductive optical planar and coaxial semiconductor detectors," *IEEE Transactions on Electron Devices*, vol. 29, no. 9, pp. 1431–1441, 1982.

[60] H. Störmer, R. Dingle, A. Gossard, W. Wiegmann, and M. Sturge, "Two-dimensional electron gas at a semiconductor-semiconductor interface," *Solid state communications*, vol. 29, no. 10, pp. 705–709, 1979.

[61] G. QingáLu *et al.*, "Enhanced photocatalytic hydrogen evolution by prolonging the lifetime of carriers in zno/cds heterostructures," *Chemical communications*, no. 23, pp. 3452–3454, 2009.

[62] M. Buscema, J. O. Island, D. J. Groenendijk, S. I. Blanter, G. A. Steele, H. S. van der Zant, and A. Castellanos-Gomez, "Photocurrent generation with two-dimensional van der waals semiconductors," *Chemical Society Reviews*, vol. 44, no. 11, pp. 3691–3718, 2015.

[63] H. Huang, J. Wang, W. Hu, L. Liao, P. Wang, X. Wang, F. Gong, Y. Chen, G. Wu, W. Luo, *et al.*, "Highly sensitive visible to infrared mote2 photodetectors enhanced by the photogating effect," *Nanotechnology*, vol. 27, no. 44, p. 445201, 2016.

[64] H. Fang and W. Hu, "Photogating in low dimensional photodetectors," *Advanced science*, vol. 4, no. 12, p. 1700323, 2017.

[65] B. Miller, E. Parzinger, A. Vernickel, A. W. Holleitner, and U. Wurstbauer, "Photogating of mono-and few-layer mos2," *Applied Physics Letters*, vol. 106, no. 12, p. 122103, 2015.

[66] K. Zhang, M. Peng, A. Yu, Y. Fan, J. Zhai, and Z. L. Wang, "A substrate-enhanced mos 2 photodetector through a dual-photogating effect," *Materials Horizons*, vol. 6, no. 4, pp. 826–833, 2019.

[67] M. Yamamoto, K. Ueno, and K. Tsukagoshi, "Pronounced photogating effect in atomically thin wse2 with a self-limiting surface oxide layer," *Applied Physics Letters*, vol. 112, no. 18, p. 181902, 2018.

[68] C. Hu, D. Dong, X. Yang, K. Qiao, D. Yang, H. Deng, S. Yuan, J. Khan, Y. Lan, H. Song, *et al.*, "Synergistic effect of hybrid pbs quantum dots/2d-wse2 toward high performance and broadband phototransistors," *Advanced Functional Materials*, vol. 27, no. 2, p. 1603605, 2017.

[69] P. Staudinger, M. Sistani, J. Greil, E. Bertagnolli, and A. Lugstein, "Ultrascaled germanium nanowires for highly sensitive photodetection at the quantum ballistic limit," *Nano letters*, vol. 18, no. 8, pp. 5030–5035, 2018.

[70] M. M. Furchi, D. K. Polyushkin, A. Pospischil, and T. Mueller, "Mechanisms of photoconductivity in atomically thin mos2," *Nano letters*, vol. 14, no. 11, pp. 6165–6170, 2014.

[71] Y. Zhang, T. Ideue, M. Onga, F. Qin, R. Suzuki, A. Zak, R. Tenne, J. Smet, and Y. Iwasa, "Enhanced intrinsic photovoltaic effect in tungsten disulfide nanotubes," *Nature*, vol. 570, no. 7761, pp. 349–353, 2019.

[72] L. Wang, L. Huang, W. C. Tan, X. Feng, L. Chen, X. Huang, and K.-W. Ang, "2d photovoltaic devices: progress and prospects," *Small Methods*, vol. 2, no. 3, p. 1700294, 2018.

[73] D. J. Groenendijk, M. Buscema, G. A. Steele, S. Michaelis de Vasconcellos, R. Bratschitsch, H. S. van der Zant, and A. Castellanos-Gomez, "Photovoltaic and photothermoelectric effect in a double-gated wse2 device," *Nano letters*, vol. 14, no. 10, pp. 5846–5852, 2014.

[74] S. M. Sze and K. K. Ng, *Physics of semiconductor devices*. John wiley & sons, 2006.

[75] T. L. Benanti and D. Venkataraman, "Organic solar cells: An overview focusing on active layer morphology," *Photosynthesis research*, vol. 87, no. 1, pp. 73–81, 2006.

[76] N. W. Ashcroft and N. D. Mermin, "Solid state physics (saunders college, philadelphia, 1976)," *Appendix N*, vol. 166, 2010.

[77] J. Park, Y. Ahn, and C. Ruiz-Vargas, "Imaging of photocurrent generation and collection in single-layer graphene," *Nano letters*, vol. 9, no. 5, pp. 1742–1746, 2009.

[78] D.-K. Lim, A. Barhoumi, R. G. Wylie, G. Reznor, R. S. Langer, and D. S. Kohane, "Enhanced photothermal effect of plasmonic nanoparticles coated with reduced graphene oxide," *Nano letters*, vol. 13, no. 9, pp. 4075–4079, 2013.

[79] D. Basko, "A photothermoelectric effect in graphene," *Science*, vol. 334, no. 6056, pp. 610–611, 2011.

[80] A. Slachter, F. L. Bakker, J.-P. Adam, and B. J. van Wees, "Thermally driven spin injection from a ferromagnet into a non-magnetic metal," *Nature Physics*, vol. 6, no. 11, pp. 879–882, 2010.

[81] Z. Li, M.-H. Bae, and E. Pop, "Substrate-supported thermometry platform for nanomaterials like graphene, nanotubes, and nanowires," *Applied Physics Letters*, vol. 105, no. 2, p. 023107, 2014.

[82] Y. Wang, W. Yin, Q. Han, X. Yang, H. Ye, Q. Lv, and D. Yin, "Bolometric effect in a waveguide-integrated graphene photodetector," *Chinese Physics B*, vol. 25, no. 11, p. 118103, 2016.

[83] M. Gauvin, T. Alnasser, E. Terver, I. Abid, A. Mlayah, S. Xie, J. Brugger, B. Viallet, L. Ressier, and J. Grisolia, "Plasmonic photo-current in free-standing monolayered gold nanoparticle membranes," *Nanoscale*, vol. 8, no. 36, pp. 16162–16167, 2016.

[84] P. Richards, "Bolometers for infrared and millimeter waves," *Journal of Applied Physics*, vol. 76, no. 1, pp. 1–24, 1994.

[85] N. M. Gabor, J. C. Song, Q. Ma, N. L. Nair, T. Taychatanapat, K. Watanabe, T. Taniguchi, L. S. Levitov, and P. Jarillo-Herrero, "Hot carrier–assisted intrinsic photoresponse in graphene," *Science*, vol. 334, no. 6056, pp. 648–652, 2011.

[86] L. Britnell, R. Ribeiro, A. Eckmann, R. Jalil, B. Belle, A. Mishchenko, Y.-J. Kim, R. Gorbachev, T. Georgiou, S. Morozov, *et al.*, "Strong light-matter interactions in heterostructures of atomically thin films," *Science*, vol. 340, no. 6138, pp. 1311–1314, 2013.

[87] X. N. Xie, Y. Xie, X. Gao, C. H. Sow, and A. T. S. Wee, "Metallic nanoparticle network for photocurrent generation and photodetection," *Advanced Materials*, vol. 21, no. 29, pp. 3016–3021, 2009.

[88] J. C. Song, M. S. Rudner, C. M. Marcus, and L. S. Levitov, "Hot carrier transport and photocurrent response in graphene," *Nano letters*, vol. 11, no. 11, pp. 4688–4692, 2011.

[89] M. Barkelid and V. Zwiller, "Photocurrent generation in semiconducting and metallic carbon nanotubes," *Nature Photonics*, vol. 8, no. 1, pp. 47–51, 2014.

[90] M. Naito and S. Tanaka, "Electrical transport properties in 2 h-nbs2,-nbse2,-tas2 and-tase2," *Journal of the Physical Society of Japan*, vol. 51, no. 1, pp. 219–227, 1982.

[91] N. Mehmood, H. R. Rasouli, O. Çakıroğlu, and T. S. Kasırga, "Photocurrent generation in a metallic transition-metal dichalcogenide," *Physical Review B*, vol. 97, no. 19, p. 195412, 2018.

[92] X. Wang, J. Lin, Y. Zhu, C. Luo, K. Suenaga, C. Cai, and L. Xie, "Chemical vapor deposition of trigonal prismatic nbs 2 monolayers and 3r-polytype few-layers," *Nanoscale*, vol. 9, no. 43, pp. 16607–16611, 2017.

[93] W. G. Fisher and M. Sienko, "Stoichiometry, structure, and physical properties of niobium disulfide," *Inorganic Chemistry*, vol. 19, no. 1, pp. 39–43, 1980.

[94] S. Zhao, T. Hotta, T. Koretsune, K. Watanabe, T. Taniguchi, K. Sugawara, T. Takahashi, H. Shinohara, and R. Kitaura, "Two-dimensional metallic nbs2: growth, optical identification and transport properties," *2D Materials*, vol. 3, no. 2, p. 025027, 2016.

[95] N. Cusack and P. Kendall, "The absolute scale of thermoelectric power at high temperatwe," 1958.

[96] X. Xu, N. M. Gabor, J. S. Alden, A. M. van der Zande, and P. L. McEuen, "Photo-thermoelectric effect at a graphene interface junction," *Nano letters*, vol. 10, no. 2, pp. 562–566, 2010.

[97] T. L. Bergman, A. Lavine, F. P. Incropera, and D. P. Dewitt, *Fundamentals of heat and mass transfer*. John Wiley & Sons New York, 2017.

[98] C.-W. Chang, D. Okawa, H. Garcia, A. Majumdar, and A. Zettl, "Breakdown of fourier's law in nanotube thermal conductors," *Physical review letters*, vol. 101, no. 7, p. 075903, 2008.

[99] L.-D. Zhao, S.-H. Lo, Y. Zhang, H. Sun, G. Tan, C. Uher, C. Wolverton, V. P. Dravid, and M. G. Kanatzidis, "Ultralow thermal conductivity

and high thermoelectric figure of merit in snse crystals," *Nature*, vol. 508, no. 7496, pp. 373–377, 2014.

[100] G. Zhang and Y.-W. Zhang, "Thermal properties of two-dimensional materials," *Chinese Physics B*, vol. 26, no. 3, p. 034401, 2017.

[101] Y. Xian, P. Zhang, S. Zhai, P. Yuan, and D. Yang, "Experimental characterization methods for thermal contact resistance: A review," *Applied thermal engineering*, vol. 130, pp. 1530–1548, 2018.

[102] M. Paillet, R. Parret, J.-L. Sauvajol, and P. Colomban, "Graphene and related 2d materials: An overview of the raman studies," *Journal of Raman Spectroscopy*, vol. 49, no. 1, pp. 8–12, 2018.

[103] E. Yalon, O. B. Aslan, K. K. Smithe, C. J. McClellan, S. V. Suryavanshi, F. Xiong, A. Sood, C. M. Neumann, X. Xu, K. E. Goodson, *et al.*, "Temperature-dependent thermal boundary conductance of monolayer mos2 by raman thermometry," *ACS applied materials & interfaces*, vol. 9, no. 49, pp. 43013–43020, 2017.

[104] H. Malekpour and A. A. Balandin, "Raman-based technique for measuring thermal conductivity of graphene and related materials," *Journal of Raman Spectroscopy*, vol. 49, no. 1, pp. 106–120, 2018.

[105] I. Jo, M. T. Pettes, L. Lindsay, E. Ou, A. Weathers, A. L. Moore, Z. Yao, and L. Shi, "Reexamination of basal plane thermal conductivity of suspended graphene samples measured by electro-thermal micro-bridge methods," *AIP Advances*, vol. 5, no. 5, p. 053206, 2015.

[106] J. A. Hernandez, J. Carpena-Nunez, L. F. Fonseca, M. T. Pettes, M. J. Yacaman, and A. Benitez, "Thermoelectric properties and thermal tolerance of indium tin oxide nanowires," *Nanotechnology*, vol. 29, no. 36, p. 364001, 2018.

[107] Z. Wang, R. Xie, C. T. Bui, D. Liu, X. Ni, B. Li, and J. T. Thong, "Thermal transport in suspended and supported few-layer graphene," *Nano letters*, vol. 11, no. 1, pp. 113–118, 2011.

[108] Z. Wang, R. Xie, C. T. Bui, D. Liu, X. Ni, B. Li, and J. T. Thong, "Thermal transport in suspended and supported few-layer graphene," *Nano letters*, vol. 11, no. 1, pp. 113–118, 2011.

[109] J.-L. Battaglia, A. Kusiak, C. Rossignol, and N. Chigarev, "Thermal diffusivity of a metallic thin layer using the time-domain thermo reflectance technique," in *Journal of Physics: Conference Series*, vol. 92, p. 92, 2007.

[110] P. Jiang, X. Qian, and R. Yang, "Tutorial: Time-domain thermoreflectance (tdtr) for thermal property characterization of bulk and thin film materials," *Journal of Applied Physics*, vol. 124, no. 16, p. 161103, 2018.

[111] P. Jiang, X. Qian, and R. Yang, "Time-domain thermoreflectance (tdtr) measurements of anisotropic thermal conductivity using a variable spot size approach," *Review of Scientific Instruments*, vol. 88, no. 7, p. 074901, 2017.

[112] A. Rosencwaig, "Thermal-wave imaging," *Science*, vol. 218, no. 4569, pp. 223–228, 1982.

[113] D. G. Cahill, "Thermal conductivity measurement from 30 to 750 k: the 3ω method," *Review of scientific instruments*, vol. 61, no. 2, pp. 802–808, 1990.

[114] T. Tong and A. Majumdar, "Reexamining the 3-omega technique for thin film thermal characterization," *Review of Scientific Instruments*, vol. 77, no. 10, p. 104902, 2006.

[115] O. Çakıroğlu, N. Mehmood, M. M. Çiçek, A. Aikebaier, H. R. Rasouli, E. Durgun, and T. S. Kasırga, "Thermal conductivity measurements in nanosheets via bolometric effect," *2D Materials*, vol. 7, no. 3, p. 035003, 2020.

[116] J.-L. Ouvrier-Buffet and J.-J. Yon, "Thermal detector with bolometric effect amplification," Nov. 13 2001. US Patent 6,316,770.

[117] T. S. Kasirga, "Thermal conductivity measurements via the bolometric effect," in *Thermal Conductivity Measurements in Atomically Thin Materials and Devices*, pp. 29–50, Springer, 2020.

[118] M. Yethiraj, "Pure and doped vanadium sesquioxide: A brief experimental review," *Journal of Solid State Chemistry*, vol. 88, no. 1, pp. 53–69, 1990.

[119] H. R. Rasouli, N. Mehmood, O. Çakıroğlu, E. C. Sürmeli, and T. S. Kasırga, "Synthesis of v 2 o 3 nanoplates for the exploration of the correlated supercritical state," *Physical Review B*, vol. 100, no. 16, p. 161107, 2019.

[120] H. R. Rasouli, N. Mehmood, O. Çakıroğlu, and T. S. Kasırga, "Real time optical observation and control of atomically thin transition metal dichalcogenide synthesis," *Nanoscale*, vol. 11, no. 15, pp. 7317–7323, 2019.

[121] C. Tatsuyama and H. Fan, "Raman scattering and phase transitions in v 2 o 3 and (v 1- x cr x) 2 o 3," *Physical Review B*, vol. 21, no. 7, p. 2977, 1980.

[122] N. Kuroda and H. Fan, "Raman scattering and phase transitions of v 2 o 3," *Physical Review B*, vol. 16, no. 11, p. 5003, 1977.

[123] V. Andreev, F. Chudnovskij, A. Petrov, and E. Terukov, "Thermal conductivity of vo 2, v 3 o 5, and v 2 o 3," *Physica Status Solidi. A, Applied Research*, vol. 48, no. 2, pp. K153–K156, 1978.

[124] C. Lamsal and N. Ravindra, "Optical properties of vanadium oxides-an analysis," *Journal of materials science*, vol. 48, no. 18, pp. 6341–6351, 2013.

[125] S. Nagata, T. Aochi, T. Abe, S. Ebisu, T. Hagino, Y. Seki, and K. Tsutsumi, "Superconductivity in the layered compound 2h-tas2," *Journal of Physics and Chemistry of Solids*, vol. 53, no. 10, pp. 1259–1263, 1992.

[126] I. Guillamón, H. Suderow, J. G. Rodrigo, S. Vieira, P. Rodiere, L. Cario, E. Navarro-Moratalla, C. Martí-Gastaldo, and E. Coronado, "Chiral charge order in the superconductor 2h-tas2," *New Journal of Physics*, vol. 13, no. 10, p. 103020, 2011.

[127] E. Navarro-Moratalla, J. O. Island, S. Manas-Valero, E. Pinilla-Cienfuegos, A. Castellanos-Gomez, J. Quereda, G. Rubio-Bollinger, L. Chirolli, J. A. Silva-Guillén, N. Agraït, *et al.*, "Enhanced superconductivity in atomically thin tas 2," *Nature communications*, vol. 7, no. 1, pp. 1–7, 2016.

[128] S. Sugai, K. Murase, S. Uchida, and S. Tanaka, "Studies of lattice dynamics in 2h tas2 by raman scattering," *Solid State Communications*, vol. 40, no. 4, pp. 399–401, 1981.

[129] A. Castellanos-Gomez, M. Buscema, R. Molenaar, V. Singh, L. Janssen, H. S. Van Der Zant, and G. A. Steele, "Deterministic transfer of two-dimensional materials by all-dry viscoelastic stamping," *2D Materials*, vol. 1, no. 1, p. 011002, 2014.

[130] F. Turker, O. R. Caylan, N. Mehmood, T. S. Kasirga, C. Sevik, and G. Cambaz Buke, "Cvd synthesis and characterization of thin mo2c crystals," *Journal of the American Ceramic Society*, vol. 103, no. 10, pp. 5586–5593, 2020.